STUDYING STRAIN AND DEVICE RELIABILITY IN III-V RIDGE WAVEGUIDE DFB DIODE LASERS USING THE DEGREE OF POLARISATION OF PHOTOLUMINESCENCE (DOP)

STUDYING STRAIN AND DEVICE RELIABILITY IN III-V RIDGE WAVEGUIDE DFB DIODE LASERS USING THE DEGREE OF POLARISATION OF PHOTOLUMINESCENCE (DOP)

By

MICHAEL N. MUCHEMU, BSc.

A Thesis

Submitted to the School of Graduate Studies

In Partial Fulfilment of the Requirements

For the Degree

Master of Applied Science

McMaster University

© Copyright by Michael N. Muchemu, 2007

MASTER OF APPLIED SCIENCE (2007) McMaster University

(Engineering Physics) Hamilton, Ontario

TITLE: Studying Strain and Device Reliability in III-V Ridge Waveguide DFB Diode Lasers Using the Degree of Polarisation of Photoluminescence (DOP)

AUTHOR: Michael N. Muchemu, BSc (University of Guelph)

SUPERVISOR: Professor Daniel T. Cassidy

NUMBER OF PAGES: xi, 153

ABSTRACT

A study of the reliability of semiconductor distributed feedback diode lasers is presented using the degree of polarisation of photoluminescence (DOP). Two figures of merit, v and w, are developed and used to characterise device aging times and performance. v measures the strain gradient between the top and middle of a device by calculating the difference in an area-averaged DOP between the middle and top of a fixed area of the device. w measures the average strain profile across the top of the device by taking the difference in an area-averaged DOP between the region immediately beneath the ridge and the regions to the immediate right and left of it. Further, the influence of aging and the nature of metal contact are explored as they relate to these metrics.

Finite element fits to the DOP and rotated degree of polarisation of photoluminescence (ROP) are presented. The models thus generated are used to explain the nature of the strain observed in different devices.

ACKNOWLEDGEMENTS

I would first like to thank my supervisor, Dr. Daniel T. Cassidy, without whom this thesis would not have been possible. You have been an excellent supervisor and have provided me with very insightful suggestions at crucial moments during my research and the development of this thesis. Your high standards and professionalism do not go unremarked and are very much appreciated.

I would also like to than Dr. Douglas Bruce, whose assistance with several technical matters has been invaluable. I may not have utilised all the tips and trick learnt from him for this thesis, but I believe I am the better for learning them.

I would also like to thank the members of staff of the Engineering Physics Office, particularly Ms. Fran Allen, Ms. Marilyn Marlow and Ms. Lori Cole. They have made my task sorting out administrative and bureaucratic matters considerably less daunting as it might have been and have my sincerest thanks.

Last but not least, I would like to acknowledge my parents and my siblings, whose faith in my ability and me is undiminished and uplifting.

TABLE OF CONTENTS

CHAPTER 1 – INTRODUCTION 1

CHAPTER 2 – THEORETICAL BACKGROUND

2.1. Introduction 7

2.2. Stress and Strain 7

2.3. Measuring Strain Using the Degree of Polarisation of Photoluminescence 14

2.3.1. The Effect of Strain on Band Structure 14

2.3.2. The Degree of Polarisation of Photoluminescence (DOP)......................16

2.4. Conclusion 20

CHAPTER 3 – MEASUREMENT SYSTEM

3.1. Introduction 21

3.2. DOP Apparatus 21

3.3. The Devices 26

3.4. Summary 27

CHAPTER 4 – DOP AND ROP MAPS – QUALITATIVE ANALYSIS

4.1. Introduction..28

4.2. The Experiment 28

4.3. Results..28

4.4. Discussion 34

4.5. Summary 40

CHAPTER 5 – DOP AND ROP MAPS: QUANTITATIVE ANALYSIS

5.1. Introduction..42

5.2. Extracting Quantitative Information 42

5.3. Results 44

5.3.1. The Influence of Number of Life-test Hours on v 44

5.3.2. The Influence of Metal Thickness on v and w..................................49

5.3.3. The Correlation of Degradation Rate to %DOP/ROP-derived Metrics.... 52

5.4. Discussion 56

5.4.1. The Influence of Number of Life-test Hours on v..............................56

5.4.2. The Influence of Metal Thickness on v and w..................................62

5.4.3. The Correlation of Degradation Rate to %DOP/ROP-derived Metrics 63
5.5. Summary 63

CHAPTER 6: FINITE ELEMENT METHOD AND FITTING TO DATA
6.1. Introduction 65
6.2. Overview of the Finite Element Method 65
6.2.1. Discretisation 66
6.2.2. Approximating Equations 66
6.2.3. Assembly 67
6.2.4. Boundary Conditions 67
6.2.5. Solution 68
6.3. Fitting to Data 68
6.3.1. The System 68
6.3.2. Modelling 71
6.4. Results 74
6.4.1. Discussion: Strain Plots Extracted From DOP Fits 78
6.4.2. Summary 115
6.4.3. Discussion: Shear Strain Plots Extracted From ROP Fits 116
6.4.4. Summary 132
6.5. Conclusion 134

CHAPTER 7: CONCLUSION
7.1. Introduction 135
7.2. Review 135
7.3. Suggestions for Future Work 137

REFERENCES 139

LIST OF FIGURES

Figure 2.1. An illustration of the lifting of degeneracy, band deformation and band gap change brought about by strain. The system dispersion curves are evaluated at the Γ point. Figure adapted from C.P. Kuo, S.K. Vong, R.M. Cohen, & G.B. Stringfellow, "Effect of Mismatch Strain on Band Gap in III-V Semiconductors," J. Appl. Phys. **57**(12), 5428-5432, (1985)........16

Figure 2.2. A diagram of a typical DOP and ROP measurement arrangement. Indicated are the transmission axes of the polariser necessary to achieve +1 for the measurement of DOP and ROP as viewed by the detector. The *y*-axis is out of the plane defined by the page........19

Figure 3.1. Apparatus used to measure DOP and ROP of the given samples........23

Figure 4.1. DOP (left column) and ROP (right column) of the laser facets for two devices. Note the extensive damage to the top of the device (a). This is typical of samples from this hour group, being present in 7 of the 19 scanned devices from this group. At the top of (a) is indicated where the ridge structure would be in an undamaged sample........30

Figure 4.2. DOP (left column) and ROP (right column) of the laser facets for two devices. The prominent black regions at the centre of the device in the DOP scans are a common feature of the shorter-lived devices........31

Figure 4.3. DOP (left column) and ROP (right column) of the laser facets for two devices........32

Figure 4.4. DOP (left column) and ROP (right column) of the laser facets for two devices. The bottom device shows an extensive dark region........32

Figure 4.5. DOP (left column) and ROP (right column) of the laser facets for two devices. The ridge structure can be inferred from the top central pattern of the DOP scan........33

Figure 4.6.. DOP (left column) and ROP (right column) of the laser facets for two devices. The bottom laser shows an absence of the dark region in the DOP scan. The dark region is characteristic of the shorter-tested samples. While this was not always present in the 4300 hours and 5000 hour samples, there were still more samples with this DOP distribution in the longer-tested groups (4300 hours and 5000 hours) than in the shorter-tested groups........34

Figure 4.7. This figure shows the SEM images highlighting the poor contact issue mentioned above. The light region just below the metal (white region) is the InGaAs layer, which has been considerably thinned by over-etching on the device on the left hand side. Note the shape difference at the bottom corners of the ridge. The sharp corner of the devices on the left should create a higher strain environment near the bottom of the ridge compared to the corners of the devices on the right, which are pared off *Courtesy of Dr. Marcel Boudreau, InP MZ Design, Bookham Co Ltd*........36

Figure 5.1. Areas used to determine average DOP and ROP values for the calculation of *v* and *w*. The zoomed region indicates the ridge waveguide structure. All measurements are in μm........44

Figure 5.2. I_{th} (mA) vs (Stress) Time (hours) for the Pt = Ti = 38 nm metal stack. Indicated are the unique device identifiers. 53

Figure 5.3. Typical plot of v(%DOP) vs. degradation rate (mA/khr)....55

Figure 5.4. This figure shows the probability, p(within $t\sigma$) that a measurement will fall within t-standard deviations of the mean. It is evident that this probability rapidly approaches unity as t increases....61

Figure 6.1. This figure indicates typical traction forces applied to the model to fit to the DOP and ROP data from the measurements carried out for this thesis. Indicated also are the axes systems used. The red points represent forces out of the plane of the paper (in either the positive or negative z-direction). Note that the directions and numbers of the forces indicated are simplified. Depending on the particular device, there may be as many or fewer forces, and in different directions....72

Figure 6.2. (a) and (b) show the DOP and ROP maps on the left column and their corresponding fits on the right for two different devices. 75

Figure 6.3. (a) and (b) show the DOP and ROP maps on the left column and their corresponding fits on the right for two different devices. 76

Figure 6.4. (a) and (b) show the DOP and ROP maps on the left column and their corresponding fits on the right for two different devices.... 77

Figure 6.5. (a) - (e) This series of plots shows the strain profile along horizontal sections taken 0.1, 0.3, 0.5, 0.7, and 0.9 times the height, *yt*, of the device. As noted before, $ey \equiv \varepsilon_{zz}$. 78

Figure 6.6. This figure shows the strain profile through a vertical section through the middle of the device. As before, $ey \equiv \varepsilon_{zz}$. The profile evalutated at 0.25 and 0.75 the width, wc, of the facet remained similar in shape. 82

Figure 6.7. This diagram shows the distortion to the facet that causes the strains calculated in Figure 6.4. (a) – (e). As established before, the y-axis here is the z-axis in the discussion....83

Figure 6.8. (a) - (e) This series of plots shows the strain profile along horizontal sections taken 0.1, 0.3, 0.5, 0.7, and 0.9 times the height, *yt*, of the device. As noted before, $ey \equiv \varepsilon_{zz}$. 84

Figure 6.9. This figure shows the strain profile through a vertical section through the middle of the device. As before, $ey \equiv \varepsilon_{zz}$. The profile evalutated at 0.25 and 0.75 the width, wc, of the facet remained similar in shape. 89

Figure 6.10. This diagram shows the distortion to the facet that causes the strains calculated in Figure 6.7. (a) – (e). As established before, the y-axis here is the z-axis in the discussion....90

Figure 6.11. (a) - (e) This series of plots shows the strain profile along horizontal sections taken 0.1, 0.3, 0.5, 0.7, and 0.9 times the height, *yt*, of the device. As noted before, $ey \equiv \varepsilon_{zz}$..............91

Figure 6.12. This figure shows the strain profile through a vertical section through the middle of the device. As before, $ey \equiv \varepsilon_{zz}$. The profile evalutated at 0.25 and 0.75 the width, wc, of the facet remained similar in shape. 92

Figure 6.13. This diagram shows the distortion to the facet that causes the strains calculated in Figure 6.10. (a) – (e). As established before, the *y*-axis here is the *z*-axis in the discussion..............96

Figure 6.14. (a) - (e) This series of plots shows the strain profile along horizontal sections taken 0.1, 0.3, 0.5, 0.7, and 0.9 times the height, *yt*, of the device. As noted before, $ey \equiv \varepsilon_{zz}$. 97

Figure 6.15. This figure shows the strain profile through a vertical section through the middle of the device. As before, $ey \equiv \varepsilon_{zz}$. The profile evalutated at 0.25 and 0.75 the width, wc, of the facet remained similar in shape. 101

Figure 6.16. This diagram shows the distortion to the facet that causes the strains calculated in Figure 6.13. (a) – (e). As established before, the *y*-axis here is the *z*-axis in the discussion..............102

Figure 6.17. (a) – (e) This series of plots shows the strain profile along horizontal sections taken 0.1, 0.3, 0.5, 0.7, and 0.9 times the height, *yt*, of the device. As noted before, $ey \equiv \varepsilon_{zz}$. 103

Figure 6.18. This figure shows the strain profile along a vertical section through the middle of the device. As before, $ey \equiv \varepsilon_{zz}$. The profile evalutated at 0.25 and 0.75 the width, wc, of the facet remained similar in shape. 107

Figure 6.19. This diagram shows the distortion to the facet that causes the strains calculated in Figure 6.16. (a) – (e). As established before, the *y*-axis here is the *z*-axis in the discussion..............108

Figure 6.20. (a) – (e). This series of plots shows the strain profile along horizontal sections taken 0.1, 0.3, 0.5, 0.7, and 0.9 times the height, *yt*, of the device. As noted before, $ey \equiv \varepsilon_{zz}$. 109

Figure 6.21. This figure shows the strain profile through a vertical section through the middle of the device. As before, $ey \equiv \varepsilon_{zz}$. The profile evalutated at 0.25 and 0.75 the width, wc, of the facet remained similar in shape. 113

Figure 6.22. This diagram shows the distortion to the facet that causes the strains calculated in Figure 6.19. (a) – (e). As established before, the *y*-axis here is the *z*-axis in the discussion..............114

Figure 6.23.(a) - (b) This figure shows the shear strain profile evaluated at 0.1 and 0.9 times the height, yt, of the facet. As noted before, $gxy \equiv \varepsilon_{xz}$..............117

Figure 6.24.(a) - (b) This figure shows the shear strain profile evaluated at 0.1 and 0.9 times the height, yt, of the facet. As noted before, $gxy \equiv \varepsilon_{xz}$..............120

Figure 6.25. (a) - (b) This figure shows the shear strain profile evaluated at 0.1 and 0.9 times the height, yt, of the facet. As noted before, $gxy \equiv \varepsilon_{xz}$..............122

Figure 6.26. (a) – (b) This figure shows the shear strain profile evaluated at 0.1 and 0.9 times the height, yt, of the facet. As noted before, $gxy \equiv \varepsilon_{xz}$..125
Figure 6.27. (a) – (b) This figure shows the shear strain profile evaluated at 0.1 and 0.9 times the height, yt, of the facet. As noted before, $gxy \equiv \varepsilon_{xz}$..128
Figure 6.28. (a) – (b) This figure shows the shear strain profile evaluated at 0.1 and 0.9 times the height, yt, of the facet. As noted before, $gxy \equiv \varepsilon_{xz}$..130

LIST OF TABLES

Table 3.1. List of components used in DOP measurement..24

Table 5.1. v-values for DOP data. The values are calculated from % DOP data. The thickness of metal contact is shown on the two right hand side columns. Au thickness is fixed at 564 nm..........................45

Table 5.2. v-values for ROP data. The values are calculated from % ROP data..................................46

Table 5.3. This table shows the results of a one-tailed Mann-Whitney U test carried out on v-values calculated from devices in the first five hour groups, excluding the 5000-hour group. The α-level was set at 0.025..48

Table 5.4. This table shows the effect of varying Ti thickness from between 75 nm and 50 nm for a fixed Pt thickness of 100 nm on the mean value of w(%DOP and %ROP) and v(%DOP and %ROP)..................50

Table 5.5. This table shows the effect of varying Pt thickness from 28 nm to 100 nm for a fixed Ti thickness of 28 nm on the mean value of w(%DOP and %ROP) and v(%DOP and %ROP)..................51

Table 5.6. This table shows the effect of a thin metal stack (Pt = Ti = 38 nm) on the mean value of w(%DOP and %ROP) and v(%DOP and %ROP). 51

Table 5.7. This table shows the mean degradation rate for various metal-stack-thickness groups, and their associated standard deviations, as calculated from the slopes of linear fits to I_{th} (mA) vs. stress time (hrs) data...54

Table 5.8. This table the v(%DOP) values for both aged and non-aged devices from each batch in each hour group..57

Chapter 1. Introduction

There are in general many factors that influence the lifetime of any device.

The reliability of optical sources such as diode lasers is strongly dependent on degradation modes [1]. These degradation modes are typically expressed in Arrhenius-type relationships, with each mode characterised by a specific activation energy [2].

Some of the main degradation modes are: dislocations, metal diffusion and alloy reaction, which affect the contact; solder instability due to reaction and migration, which affects the bonding parts; inherent defects in buried heterostructure devices; and the separation of metals in the heat sink bond. In addition, any facet damage due to oxidation is exacerbated by light or moisture [2].

Dislocations result from several sources, characterised by their direction of growth: those that grow in the <100> direction, and those that grow in the <110> direction [2]. Growth along the <100> direction is through nonradiative-recombination-enhanced defect motion. In this process, dislocations and point defects, such as interstitial atoms and vacancies, form nonradiative recombination centres; energy emitted here is transferred into lattice vibrations via multiple phonon emissions, giving rise to low-temperature defect motion. The dislocation network elongates by emitting a vacancy or absorbing an interstitial atom. This type of dislocation originates from threading dislocations from defects in the

substrate, as well as stacking faults introduced during crystal growth. They can therefore be reduced by improving crystal growth techniques as well as using high-quality substrate with a low defect density. The <110> dislocation network is caused by mechanical stress [2]. Its growth rate depends on both the magnitude of the stress and the bonding energy of the host atoms of the crystal. Ternary and quaternary materials tend to be resistant to this type of dislocation growth. This kind of dislocation network can be inhibited by decreasing the amount of external mechanical stress imposed on the chips, for instance stress due to the mounting process.

Degradation may also result from the diffusion of metal into the semiconductor. There are two kind of electrodes used to eliminate the metal-semiconductor energy barrier in order to obtain an ohmic contact: alloy-type and Schottky-type. In alloy-type electrodes, such as AuZnNi, the sintering process allows alloy reaction to proceed at the metal-semiconductor interface even during device operation. Metal diffusion into the interior of the device takes place, resulting in separate layers of metal – III and metal – V alloys. Additionally, individual diffusion of metal atoms from the electrode result in nonradiative recombination centres in the active layer, further decreasing device efficiency. In a Schottky-type electrode, the semiconductor is heavily doped to reduce the metal-semiconductor barrier. The metal is used here to form an inert interface between electrode and semiconductor. The electrode is therefore stable under typical operating conditions. The devices examined in this paper have Schottky-

type Ti/Pt/Au contacts. While these contacts are stable, it has been shown that increasing the thickness of the Ti layer to greater than 10 nm can lead to an increase in the resistance of the contact [3, 4].

The high optical density at the facet makes laser diodes particularly susceptible to facet degradation [2]. Optical absorption at the facet triggers facet degradation; nonradiative recombination of electrons and holes at the facet results in heating , which reduces the band gap, resulting in further absorption and more heating, in a positive-feedback loop that causes sudden failure (catastrophic optical damage, or COD). Additionally, the bond-breaking at the facet due to electron-hole pairs increases the rate of semiconductor oxidation. Since oxidation introduces extraneous atoms into the semiconductor, this process can be regarded as defect injection into the active region. It is not uncommon to observe dislocation networks at a facet subjected to COD [2].

Stress is exerted and strain induced on the chip from various sources. The difference in thermal expansion coefficients between the metal contact and the underlying semiconductor serves to induce strain as the materials cool down upon processing. The dielectric layer applied to the semiconductor exerts traction stresses on the facet. Moreover, the growth of deliberately strained layers through heteroepitaxy means the internal environment of the diode laser is inherently strained. As such any defects that may be incorporated during processing may lead to sudden, premature failures.

Soft-solders such as In, Sn and Sn-rich Au-Sn solders are susceptible to solder instabilities such as thermal fatigue, diffusion (similarly to what occurs at the contact), void formation at the bonding region and whisker growth [2]. Such instabilities lead to sudden failure. Hard solders, such as Au-rich Au-Sn materials remove many of these instabilities [2]. Additionally, such solders induce strain on the overlying semiconductor via mechanisms similar to the metal contact [5].

The investigation for this thesis has solely concerned itself with the influence of strain on the reliability of the devices investigated. While not all strain has deleterious effects on the performance of a diode laser (a fact which has been taken advantage of in strained quantum well lasers), external strain, such as that derived from bonding, has been shown to accelerate degradation modes in optoelectronic devices [6, 7]. Large strains near the active region of the device impact the optical guidance, transfer properties and optical grating providing feedback for the laser. Strain may be deliberately introduced to ensure lateral confinement via the optoelastic effect, and therefore any extraneous strain may detract from the performance of the device.

The method used to investigate strain in these devices is the degree of polarisation of photoluminescence (DOP) and its equivalent, the rotated degree of polarisation of photoluminescence (ROP). This has been shown to be an adequate method of extracting strain- and stress-related information from photoluminescent materials [8, 9,10,11].

Two metrics, v and w, have been introduced in this thesis in order to quantify and make sense of these findings. This is a value that measures the change in strain as one moves from the middle to the top of the facet, and it is used to characterise the difference in lifetime observed between different groups of devices.

The finite element method is exploited for further analysis of the data. Fits are made to the data in order to extract stresses and strain on the laser facets.

This document is organised into seven chapters.

Chapter 1 is introductory, giving an overview of the issues to be dealt with later.

Chapter 2 provides a theoretical treatment of the concepts involved in elasticity.

Chapter 3 describes the details of the experimental system used to make DOP and ROP measurements, as well as outlining the processing steps used to fabricate the devices used in this investigation.

Chapter 4 provides a qualitative treatment of the data accumulated for this thesis. It will describe the general trends observed in the DOP and ROP maps for the different devices and interpret them within some general scheme.

Chapter 5 furnishes a more quantitative treatment, introducing the figures of merit, v and w, and explaining how they relate to the different performances observed between different groups of devices.

Chapter 6 presents an introduction to the finite element method and how it pertains to this study. Fits to the data will be presented and the strains explained according to their possible origins for various groups of devices.

Chapter 7 summarises the work in this thesis as well as providing avenues for future research in this area.

Chapter 2. Theoretical Background

2.1. Introduction

The process of manufacturing semiconductor laser diodes introduces stresses and strains in the device via various mechanisms. The epitaxial deposition of thin semiconductor films creates lattice mismatches between layers composed of different materials. Processing takes place at elevated temperatures. Therefore, the difference in thermal expansion coefficients between different materials introduces strain between the various layers of the device.

Strain is important as it influences key physical properties of semiconductor films. It changes electronic states, resulting in the shifting of band-edge energies as well as modifying the effective masses of individual bands [12]. This impacts the transfer properties of the film. Additionally, strain affects the refractive index of the crystal, and both these factors affect the carrier and light confinement of a semiconductor laser diode.

This chapter presents an overview of some of the concepts involved in stress and strain in semiconductor materials, as well as the experimental means used to detect strain in these materials. Further particulars will be dealt with in later chapters as the need arises.

2.2. Stress and Strain

The strain in one dimension at any point, *P*, is defined as [13]:

$$e = \lim_{\Delta x \to 0} \frac{\Delta u}{\Delta x} = \frac{du}{dx} \qquad (2.1)$$

That is, the rate of change of displacement, u, with distance, x. This definition captures the intuitive understanding of strain, since a body is said to be strained when the positions of points within it are changed relative to one another. It is therefore a dimensionless quantity. The generalised form of this gives one an antisymmetrical, three-dimensional tensor of the second rank. In linear elasticity theory, this is found to be [13,14]:

$$e_{ij} = \frac{\partial u_i}{\partial x_j} \qquad (i, j = 1,2,3) \qquad (2.2)$$

For a strain tensor to make physical sense, it must vanish for rigid-body rotation, which equation (2.2) does not do [13]. To overcome this problem, one defines the strain tensor, ε_{ij} to be the symmetrical part of e_{ij}. Thus

$$\varepsilon_{ij} = \frac{1}{2}\left(e_{ij} + e_{ji}\right) \qquad (2.3)$$

or

$$\begin{bmatrix} \varepsilon_{11} & \varepsilon_{12} & \varepsilon_{13} \\ \varepsilon_{12} & \varepsilon_{22} & \varepsilon_{23} \\ \varepsilon_{13} & \varepsilon_{23} & \varepsilon_{33} \end{bmatrix} = \begin{bmatrix} e_{11} & \frac{1}{2}\left(e_{12} + e_{21}\right) & \frac{1}{2}\left(e_{13} + e_{31}\right) \\ \frac{1}{2}\left(e_{12} + e_{21}\right) & e_{22} & \frac{1}{2}\left(e_{23} + e_{32}\right) \\ \frac{1}{2}\left(e_{13} + e_{31}\right) & \frac{1}{2}\left(e_{23} + e_{32}\right) & e_{33} \end{bmatrix}$$

The diagonal components of ε_{ij} are the tensile, or normal, strains, while the off-diagonal values are the shear strains.

Stress, σ, is defined as the force acting per unit area on a given body, or more rigorously [13,14]:

$$\sigma = \lim_{\Delta A \to 0} \frac{\Delta F}{\Delta A} = \frac{dF}{dA} \qquad (2.4)$$

The stress acting on an element of area, *dA*, is in the direction of the force, ***dF***. Therefore, the stress acting on an element of area, *dA*, is a vector in the direction of *dF*. Thus, the stress on a *given plane* is a vector, the stress vector [14]. To find the stress at a given point, it is first necessary to define a plane containing the point at which we seek to determine the stress. There is a different stress vector for each of the multitude of planes that pass through the point of interest; that is, each direction of space (as determined by a unique plane) has associated with it a different (stress) vector. This is characteristic of a tensor quantity, which assigns vector quantities to each direction in space. As such, the state of stress on a given body in three dimensions may be described by a tensor, specifically one of second rank, with nine components; it is symmetrical in the absence of a distributed body-torque (one proportional to the volume, such as is present when an electric or magnetic field is put through it), and therefore it has only six independent

components [13]. Three of the components are normal stresses, and the other three independent components are shear stresses, which act in the plane.

So, we may write the stress tensor, σ_{ij}, as

$$\sigma_{ij} = \begin{bmatrix} \sigma_{11} & \sigma_{12} & \sigma_{13} \\ \sigma_{12} & \sigma_{22} & \sigma_{23} \\ \sigma_{13} & \sigma_{23} & \sigma_{33} \end{bmatrix} \qquad (i, j = 1,2,3) \qquad (2.5)$$

Both the strain and stress tensors may be written in matrix notation as column vectors, respectively:

$$\begin{bmatrix} \varepsilon_{11} \\ \varepsilon_{22} \\ \varepsilon_{33} \\ \varepsilon_{23} \\ \varepsilon_{13} \\ \varepsilon_{12} \end{bmatrix} \text{ and } \begin{bmatrix} \sigma_{11} \\ \sigma_{22} \\ \sigma_{33} \\ \sigma_{23} \\ \sigma_{13} \\ \sigma_{12} \end{bmatrix} \qquad (2.6)$$

where only the independent components are shown.

One usually uses engineering shear strains in performing calculations, and these are defined as [14]:

$$\gamma_{23} = 2\varepsilon_{23} \qquad \gamma_{13} = 2\varepsilon_{13} \qquad \gamma_{12} = 2\varepsilon_{12} \qquad (2.7)$$

The shear strain measures the change in angle between two previously orthogonal directions (axes) in units of radians.

Now, Hooke's Law relates the strain imposed on a body subject to a particular stress; that is [13,14]:

$$\sigma = c\varepsilon \qquad (2.8)$$

where c is the elastic stiffness constant, or stiffness. It is also called the modulus of elasticity, or Young's modulus.

Since this is only in one dimension, it needs to be generalised. Briefly, we find that the relationship between the stress and strain tensor is maintained by a fourth-rank tensor, the modulus tensor:

$$\sigma_{ij} = c_{ijkl}\varepsilon_{kl} \qquad (i, j, k, l = 1,2,3) \qquad (2.9)$$

A fourth-rank tensor has 81 components, but symmetry reduces the number of independent components to 36. Thus, we have [13,14]:

$$c_{ijkl} = c_{mn} \qquad (i, j, k, l = 1,2,3; m,n = 1,\ldots,6) \qquad (2.10)$$

As such, one can write (2.9) in matrix form as:

$$\begin{bmatrix}\sigma_{11}\\ \sigma_{22}\\ \sigma_{33}\\ \sigma_{23}\\ \sigma_{13}\\ \sigma_{12}\end{bmatrix} = \begin{bmatrix} c_{11} & c_{12} & c_{13} & c_{14} & c_{15} & c_{16}\\ c_{21} & c_{22} & c_{23} & c_{24} & c_{25} & c_{26}\\ c_{31} & c_{32} & c_{33} & c_{34} & c_{35} & c_{36}\\ c_{41} & c_{42} & c_{43} & c_{44} & c_{45} & c_{46}\\ c_{51} & c_{52} & c_{53} & c_{54} & c_{55} & c_{56}\\ c_{61} & c_{62} & c_{63} & c_{64} & c_{65} & c_{66}\end{bmatrix}\begin{bmatrix}\varepsilon_{11}\\ \varepsilon_{22}\\ \varepsilon_{33}\\ 2\varepsilon_{23}\\ 2\varepsilon_{13}\\ 2\varepsilon_{12}\end{bmatrix}$$

or (2.11)

$$\begin{bmatrix}\varepsilon_{11}\\ \varepsilon_{22}\\ \varepsilon_{33}\\ 2\varepsilon_{23}\\ 2\varepsilon_{13}\\ 2\varepsilon_{12}\end{bmatrix} = \begin{bmatrix} s_{11} & s_{12} & s_{13} & s_{14} & s_{15} & s_{16}\\ s_{21} & s_{22} & s_{23} & s_{24} & s_{25} & s_{26}\\ s_{31} & s_{32} & s_{33} & s_{34} & s_{35} & s_{36}\\ s_{41} & s_{42} & s_{43} & s_{44} & s_{45} & s_{46}\\ s_{51} & s_{52} & s_{53} & s_{54} & s_{55} & s_{56}\\ s_{61} & s_{62} & s_{63} & s_{64} & s_{65} & s_{66}\end{bmatrix}\begin{bmatrix}\sigma_{11}\\ \sigma_{22}\\ \sigma_{33}\\ \sigma_{23}\\ \sigma_{13}\\ \sigma_{12}\end{bmatrix}$$

(2.11) is the generalised form of Hooke's Law. The components of c_{mn} are in units of force per unit area. The inverse quantity is the compliance tensor, s_{ijkl}, and it may similarly be reduced to the matrix representation s_{mn}. Its components have units of area per unit force.

Some of these components vanish, and others are equal to each other, depending on what class of material is being considered. For cubic crystals such as GaAs or InP, the s_{ijkl}, referred to the coordinate system with a basis parallel to the <001> directions takes the form [13]:

$$\begin{bmatrix} s_{11} & s_{12} & s_{12} & 0 & 0 & 0\\ s_{12} & s_{11} & s_{12} & 0 & 0 & 0\\ s_{12} & s_{12} & s_{11} & 0 & 0 & 0\\ 0 & 0 & 0 & s_{44} & 0 & 0\\ 0 & 0 & 0 & 0 & s_{44} & 0\\ 0 & 0 & 0 & 0 & 0 & s_{44}\end{bmatrix} \quad (2.12)$$

And similarly for c_{mn}.

One may re-write this matrix in order to refer it to the {110}cleavage plane of a III-V semiconductor by rotating it by 45° about the z or (001) axis [10]

$$\begin{bmatrix} s_{11}' & s_{12}' & s_{12} & 0 & 0 & 0 \\ s_{12}' & s_{11}' & s_{12} & 0 & 0 & 0 \\ s_{12} & s_{12} & s_{11} & 0 & 0 & 0 \\ 0 & 0 & 0 & s_{44} & 0 & 0 \\ 0 & 0 & 0 & 0 & s_{44} & 0 \\ 0 & 0 & 0 & 0 & 0 & s_{66}' \end{bmatrix}_{\{110\}} \quad (2.13)$$

where $s_{11}' = (2s_{11} + 2s_{12} + s_{44})/4, s_{12}' = (2s_{11} + 2s_{12} - s_{44})$, and $s_{66}' = 2(s_{11} - s_{12})$.

Now, these expressions are essentially derived from a purely mathematical approach to the problem. Considerable simplification can be achieved by employing a semi-empirical approach. Certain assumptions can be made based on observing the behaviour of materials under infinitesimal deformations: the normal stress, σ_x, does not produce shear strain on the x, y or z planes; a shear stress, σ_{xy}, does not produce a normal strain on the x, y or z planes; a shear stress component, σ_{xy}, causes only one shear strain component, ε_{xy}; and finally, that the principle of superposition can be applied to determine the strain components produced if more than one stress component is involved [14].

With these assumptions in place, one obtains for a general state of stress in a material a simpler version of (2.11):

$$
\begin{aligned}
\varepsilon_{11} &= \frac{1}{E}\left[\sigma_{11} - \nu(\sigma_{22} + \sigma_{33})\right] \\
\varepsilon_{22} &= \frac{1}{E}\left[\sigma_{22} - \nu(\sigma_{33} + \sigma_{11})\right] \\
\varepsilon_{33} &= \frac{1}{E}\left[\sigma_{33} - \nu(\sigma_{11} + \sigma_{22})\right] \\
\varepsilon_{12} &= \frac{1}{2G}\sigma_{12} \\
\varepsilon_{23} &= \frac{1}{2G}\sigma_{23} \\
\varepsilon_{31} &= \frac{1}{2G}\sigma_{31}
\end{aligned}
\qquad (2.12)
$$

where E is Young's modulus, ν is Poisson's ratio, and $G = E/[2(1+\nu)]$ is the rigidity modulus. For an isotropic, elastic material, the principal axes of stress and those of strain coincide, leading to even more computational simplification [13,14].

2.3. Measuring Strain Using the Degree of Polarisation of Photoluminescence

Measurements carried out in this thesis are all made by exploiting the stress-induced degree of polarisation changes in luminescence in III-V semiconductors. A brief account of the concepts involved will therefore be given.

2.3.1. The effect of strain on band structure

The devices investigated in this thesis are distributed feedback lasers based on the InGaAsP system, with a standard ridge waveguide structure. These material structures have a zinc-blende configuration [13,14,15]. In this type of

material, the lowest direct band gap occurs at the centre of the Brillouin zone (the **Γ** point). The heavy hole and light hole valence bands are degenerate at this point, provided the material is not under stress.

Under non-hydrostatic strain, however, the material's crystal symmetry is lowered, and the degeneracy at the Γ point lifted [12,15]. Strain also creates a change in the band gap depending on whether the nature of the strain is compressive or tensile; the band gap increases if the material is under compression and decreases if it is under tension, depending on the direction of strain relative to the electron wave vector [12,15]. Additionally, band deformation occurs, with the consequence that the dispersion curves are no longer the same along the x-, y-, and z-axes, making the effective mass dependent on the direction of the strain. These ideas are shown in the figure below [16]:

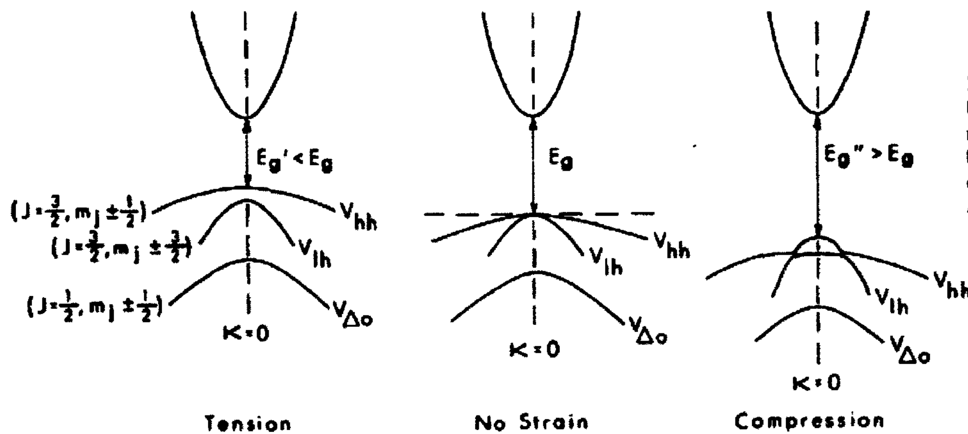

Figure 2.1: An illustration of the lifting of degeneracy, band deformation and band gap change brought about by strain. The system dispersion curves are evaluated at the Γ point. Figure adapted from C.P. Kuo, S.K. Vong, R.M. Cohen, & G.B. Stringfellow, "Effect of Mismatch Strain on Band Gap in III-V Semiconductors," J. Appl. Phys. **57**(12), 5428-5432, (1985).

2.3.2. The degree of polarisation of photoluminescence (DOP)

Starting with the direction-dependent energy shifts far from the Brillouin zone centre, and employing thermodynamic arguments, it can be shown that strain changes the probability of emission of light into a particular polarisation state [8]. The probability of interaction of a photon with an electron in the semiconductor is determined from the optical matrix element. The total emission intensity from each valence band into a given polarisation is evaluated from an integral

containing the hole and electron densities as well as the matrix element, which integral is over all possible ***k*** values, where ***k*** is the electron wave vector [8]. Strain alters the population distribution of holes and thereby directly impacts the emission intensity into a particular polarisation state.

One can then define the DOP of luminescence from a material as [10]:

$$DOP_y = \frac{\int_0^{\infty}[L_x(\varepsilon) - L_z(\varepsilon)]R(\varepsilon)d\varepsilon}{\int_0^{\infty}[L_x(\varepsilon) + L_z(\varepsilon)]R(\varepsilon)d\varepsilon} \qquad (2.13)$$

$L_x(\varepsilon)$ and $L_z(\varepsilon)$ are the magnitudes of the luminescence with energies between ε and $d\varepsilon$ that are polarised along the x and z directions and propagating along the y direction, where the y direction is perpendicular to the material (see Figure 2). $R(\varepsilon)$ is the responsivity of the detector for light energy ε. The DOP is a quantity that varies from -1 to $+1$.

For an isotropic material, it has been shown that the DOP is proportional to the difference in the components of the strain *or* the stress along two orthogonal directions [8,10]:

$$DOP_y = -C_\varepsilon(\varepsilon_{xx} - \varepsilon_{zz}) = -C_\varepsilon \frac{(1+\nu)}{E}(\sigma_{xx} - \sigma_{zz}) \qquad (2.14)$$

where C_ε is a positive calibration constant, and ε_{xx} and ε_{zz} are the normal components of strain along the x and z directions respectively; the second equation on the right follows from the stress-strain relations discussed previously in equation (2.12).

Thus, in a {110} plane:

$$DOP_y = -C_\varepsilon \left[\frac{2s_{11} - 2s_{12} + s_{44}}{4} \sigma_{xx} - (s_{11} - s_{12}) \sigma_{zz} \right] \tag{2.15}$$

as σ_{yy} vanishes at the free surface of any {110} facet where the y direction is perpendicular to the facet.

As such, the DOP is not generally equal to the difference in both strain and stress, as can be seen by comparing (2.15) to (2.14), except in the special case of an isotropic material, where $2(s_{11} - s_{12}) = s_{44}$.

There is a quantity related to the DOP, which can be obtained by rotating the sample by 45° about the y-axis. This is the rotated degree of polarisation of luminescence (ROP), defined as [10]:

$$ROP_y = \frac{\int_0^\infty [L_{x'}(\varepsilon) - L_{z'}(\varepsilon)] R(\varepsilon) d\varepsilon}{\int_0^\infty [L_{x'}(\varepsilon) + L_{z'}(\varepsilon)] R(\varepsilon) d\varepsilon} \tag{2.16}$$

where the polarisations of the luminescence are referred to the axes x' and z', which are both rotated by 45° clockwise about the y-axis (Figure 2.2).

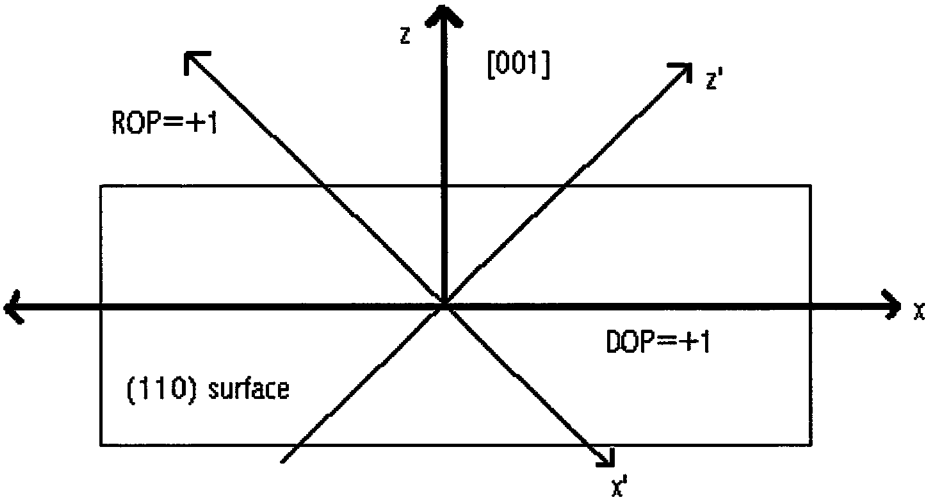

Figure 2.2: A diagram of a typical DOP and ROP measurement arrangement. Indicated are the transmission axes of the polariser necessary to achieve +1 for the measurement of DOP and ROP as viewed by the detector. The y-axis is out of the plane defined by the page.

ROP_y is related to the shear strain or shear stress in an isotropic material, and is determined by [10,14]:

$$ROP_y = 2C_\varepsilon \varepsilon_{xz} = C_\varepsilon \frac{1}{G_{xz}} \sigma_{xz} \qquad (2.17)$$

It has been shown that difference in strain provide a better fit to data than does difference in stress [10]. This might be expected, as the physical origin of DOP lies directly in band structure modification due to crystal asymmetry brought about by an applied force. For InP, C_ε has been determined to be 65 ± 10 [10].

Therefore, it is possible to extract strain and stress information by measuring the DOP and ROP from a III-V semiconductor.

2.4. Conclusion

This chapter introduced and explained the concepts entailed in analysing stress and strain in materials. Stress and strain are defined, and their tensor nature explained. Various representations are outlined, including the tensor and matrix representations. The relationship between stress and strain is also introduced and explained based on both the mathematical and semi-empirical approaches in 2.2. The matrix representation for the specific, important case of cubic crystals is also elucidated. Section 2.3. introduces and explains the quantities DOP and ROP. Their physical origins and relevance to the analysis of strain and stress in photoluminescent materials are outlined.

Chapter 3. Measurement System

3.1. Introduction

It was established in Chapter 2 that one may use the DOP and ROP of luminescence from a sample of III-V semiconductor material in order to determine strain and stress information. This chapter details the experimental apparatus.

3.2. DOP Apparatus

The experiments made for this thesis determine the DOP and ROP at a point (note that the word 'point' is used here only for convenience; the system really measures luminescence collected over a small *area* of the sample surface, and 'point' should henceforth be understood to mean this). They accomplish this by measuring the sum and differences of the orthogonal polarisation intensities at the point using the apparatus shown in Figure 3.1 below.

The set-up is designed to excite and collect light emitted from a semiconductor sample placed in the optical path. The He-Ne (later Coherent diode) laser functions as the optical pump. Light emitted from the laser goes through an optical isolator in order to minimise feedback noise due to back-reflection, and then through a neutral density filter. The latter has adjustable filtering settings that can be used to control the pump intensity. The laser light

was mechanically chopped at a frequency of 1020 Hz. A high-precision chopper is used to control this frequency to within 1 Hz. The internal frequency of the phase sensitive detector (PSD) built into the computer controlling and recording the experiment is phase-locked to the chopper frequency.

The chopped beam is reflected through a mirror, passes through a lens, reflected off a cold mirror and thence through the microscope objective onto the sample. The function of the lens is to compensate for chromatic aberration: it is necessary in a confocal system to ensure that both the pump light focused and the photoluminescent light collected by the microscope objective lie along the same optical path and are focused at the same point.

The cold mirror and filter both remove the pump light, permitting only the photoluminescence to pass. This light then passes through a rotating linear polariser and is collected by a stationary photodetector. The polariser rotates at a frequency of 200 Hz.

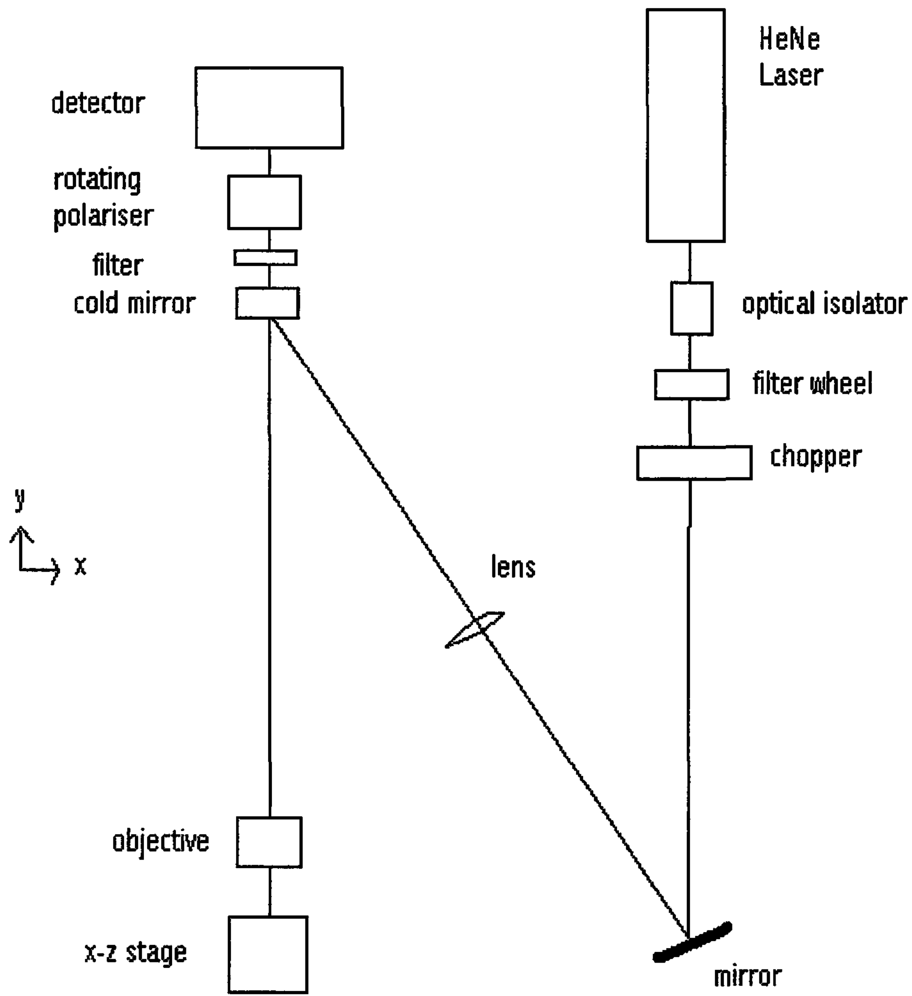

Figure 3.1. Apparatus used to measure DOP and ROP of the given samples.

The components are tabulated below:

Component	Particulars
Laser	Uniphase 632.8 nm HeNe Laser (later changed to Coherent 632.8 nm diode laser)
Optical isolator	Optics for Research IO-3-633-LP Narrowband Adjustable Isolator
Filter wheel	New Focus 5215 0.008-3.0 Dual Neutral Density Filter Wheel
Chopper	New Focus 3501 Optical Chopper
Detector	EG&G silicon C30807E
Rotating polariser	Polarcor optical glass polariser 900HC
Cold mirror	Melles Griot 03MCS005
Objective	Melles Griot 20x N.A.: 0.40
x-z stage	Melles Griot Nanomotion II Positioning Actuator System

Table 3.1. List of components used in DOP measurement.

The use of a rotating linear polariser affords one several advantages. PSD detection of the signal at the frequency of the chopper gives an output proportional to $\left\langle \int (L_x + L_z) R(\varepsilon) d\varepsilon \right\rangle$; at twice the rate of the rotating linear polariser gives $\left\langle \int (L_x - L_z) R(\varepsilon) d\varepsilon \right\rangle$ for in-phase detection and $\left\langle \int (L_{x'} - L_{z'}) R(\varepsilon) d\varepsilon \right\rangle$ for the quadrature (out-of-phase) detection [10]. The pointed brackets indicate a weighted time average. One can therefore deduce the DOP and ROP simultaneously by making ratios of the PSD outputs. This therefore allows one to ensure that measurements of these values are made from the same point on the sample. Another important advantage is that it makes measurement largely independent of wavelength over a wide range of λ ($\approx 850 - 1800$ nm).

The outputs of the PSDs are digitised with a 12-bit analogue-digital converter; the DOP and ROP values recorded by the computer are based on about 200 samples averaged from the ADC.

The chopped pump is, however, non-ideal due to the non-zero width of the laser beam as well as the finite bandwidth of the electronics. To compensate for this, a polariser with an extinction ratio of $< 10^{-3}$ is placed in the beam and aligned prior to each run. The DOP with the polariser in place should be 1 and the ROP 0. As such, setting the phases of the PSDs with the polariser in place and using this signal to normalise those obtained during a run should compensate for the imperfect nature of the square wave.

As mentioned previously, the experiment is computer-controlled. The entire apparatus is fixed on a pneumatically stabilised optical table; the sample is mounted on a motorised stage and raster-scanned. The stage is capable of sub-micrometre step sizes, though step sizes of less than 1 micron were rarely used due to the diffraction-limited nature of the optics. The sample is scanned along the x-direction then stepped in the z-direction. In this way, one obtains a map of the DOP and ROP.

Since the pump light is absorbed within a short distance of the sample surface, the strain maps inferred correspond to values close to the surface.

3.3. The Devices

The devices analysed in this thesis are distributed feedback lasers based on the InGaAsP material system, with a standard ridge waveguide structure [3, 17]. The active region was grown by metalorganic chemical vapour deposition, and a periodic grating holographically patterned and etched onto the surface. A second epitaxial layer consisting of a thick *p*-InP upper waveguide cladding and a 200-nm-thick *p*-$In_{0.53}Ga_{0.47}As$ contact layer was grown to complete the vertical waveguide structure. Ridges were etched out to achieve lateral confinement of the current and optical mode, and a dielectric passivation layer applied to the processed surface. A via was opened over the ridge and the metal stack deposited. The wafers were cleaved into bars and the cleaved facets coated with dielectric, following which the bars were diced into individual chips and mounted, active region up, on a ceramic carrier (AlN) using Au-Sn solder. The devices varied from between about 200 to 500 microns wide and 100 to 150 microns high.

The original purpose of these devices was to form a study of the influence of electrical contact on the reliability of laser diodes. As such, the thickness of metal contact atop lasers from different batches varied. Specifically, while the gold thickness was fixed at 564 nm, that of both platinum and titanium was varied. The devices were then life-tested under stress conditions intended to accelerate device degradation so that reasonable experiment times could be achieved. The metric used to assess device reliability was the threshold current, I_{th}. Degradation rates were calculated based on linear fits to an I_{th} vs. time plot [3].

Unless a device failed, testing continued to greater than 2000 hours. The tests were carried out at a temperature of 100 °C and with a current of 250 mA.

There are different ways employed to organise and subsequently analyse the data. The first is via life-test duration; the life-test regimes are 24 hours, 2400 hours, 3100 hours, 3200 hours, 4300 hours and 5000 hours. The second is according to varying metal thickness. The third is according to degradation rates.

3.4. Summary

This chapter has presented the details of the experimental apparatus used to carry out DOP and ROP measurements. The structure of the devices investigated in this thesis and processing used to manufacture them has also been discussed.

Chapter 4. DOP and ROP Maps – Qualitative Analysis

4.1. Introduction

This chapter presents the DOP and ROP maps obtained from measurements carried out on the laser facets using the apparatus described in the previous chapter. Qualitative differences in the maps are outlined and explained as they relate to differences in the performance of the respective devices.

4.2. The Experiment

DOP and ROP measurements were carried out at room temperature. Owing to the varied dimensions of the chips, different step sizes were used as needed. Due to the details of the scanning system, the controlling computer can only record a maximum of 201 step sizes in either direction (up or down). As such, the step sizes were chosen so that reasonably clear maps could be obtained from the samples at reasonable times. The horizontal step sizes ranged from about 1.80 to 2.50 microns, while the vertical step size ranged from about 0.80 to 1.20 microns. Scanning times varied between 1.5 – 9 hours.

4.3. Results

A representative sample of well over 100 devices was scanned. Some of the scans indicated extraneous damage likely associated with handling, such as

pits and scratches as well as chips to the corners of the dies at the metal-semiconductor interface, which induce a strain field at the edges of the sample. These were not considered in the thesis because they would likely skew the results. A final selection of around 120 samples was therefore used.

The figures below show the ROP and DOP maps of some of the devices scanned. These maps are derived from an in-house programme written specifically for this purpose, and called X3D.

24 Hours

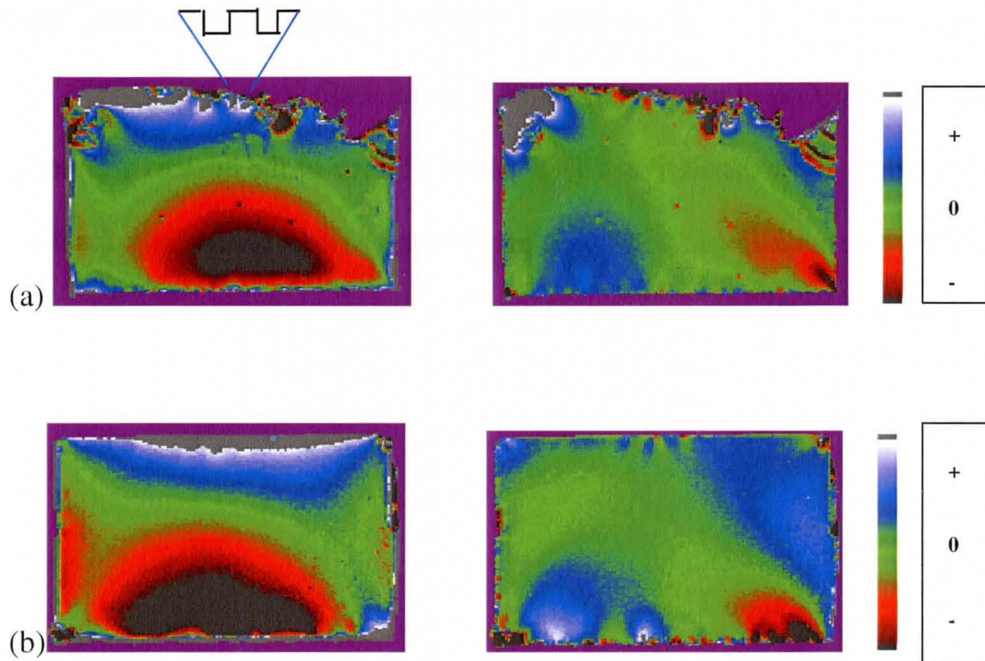

Figure 4.1. DOP (left column) and ROP (right column) of the laser facets for two devices. Note the extensive damage to the top of the device (a). This is typical of samples from this hour group, being present in 7 of the 19 scanned devices from this group. At the top of (a) is indicated where the ridge structure would be in an undamaged sample.

2400 Hours

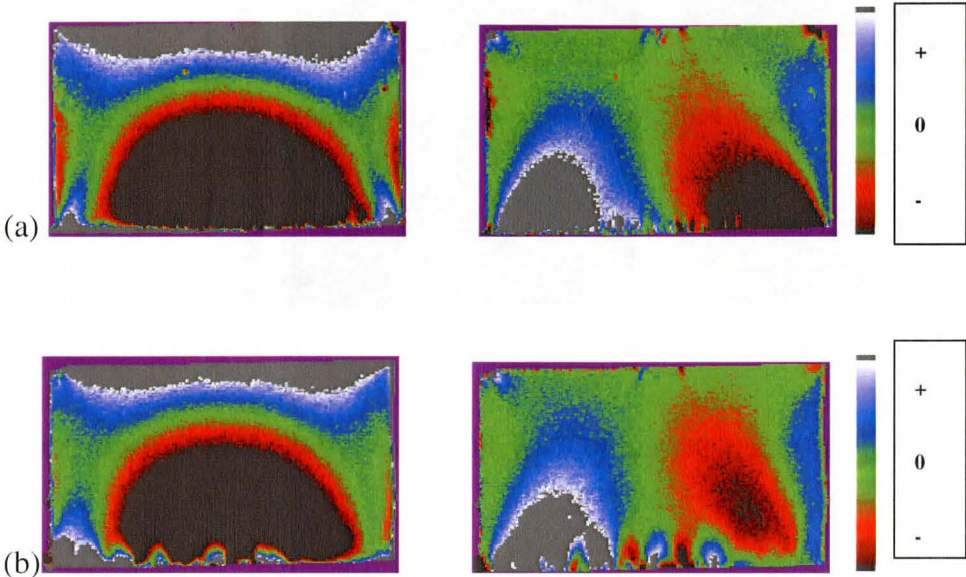

Figure 4.2. DOP (left column) and ROP (right column) of the laser facets for two devices. The prominent black regions at the centre of the device in the DOP scans are a common feature of the shorter-tested devices.

3100 Hours

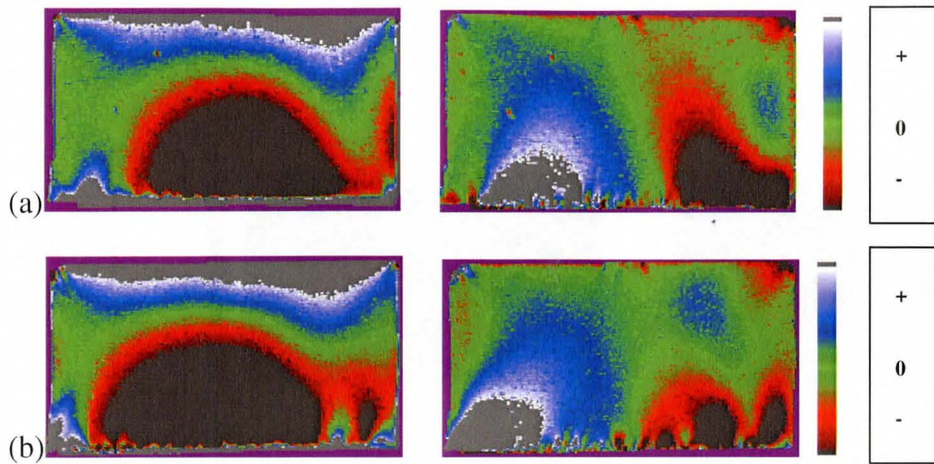

Figure 4.3. DOP (left column) and ROP (right column) of the laser facets for two devices.

3200 Hours

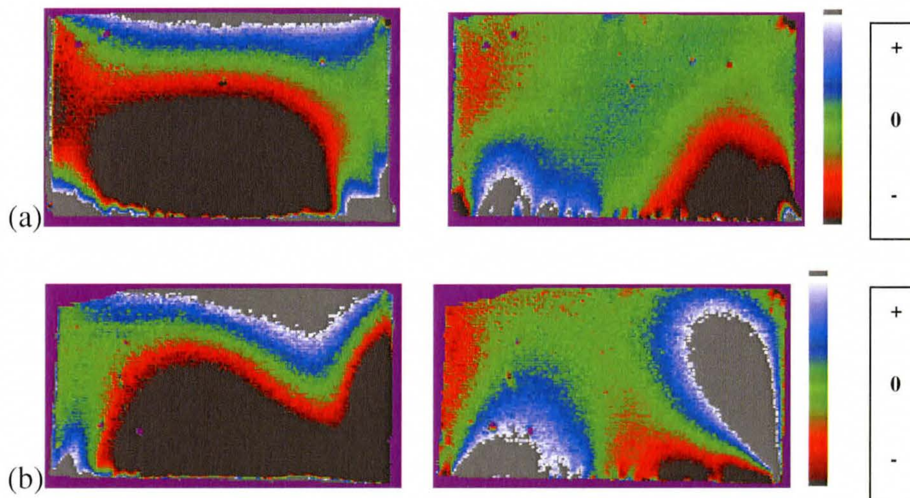

Figure 4.4. DOP (left column) and ROP (right column) of the laser facets for two devices. The bottom device shows an extensive dark region.

4300 hours

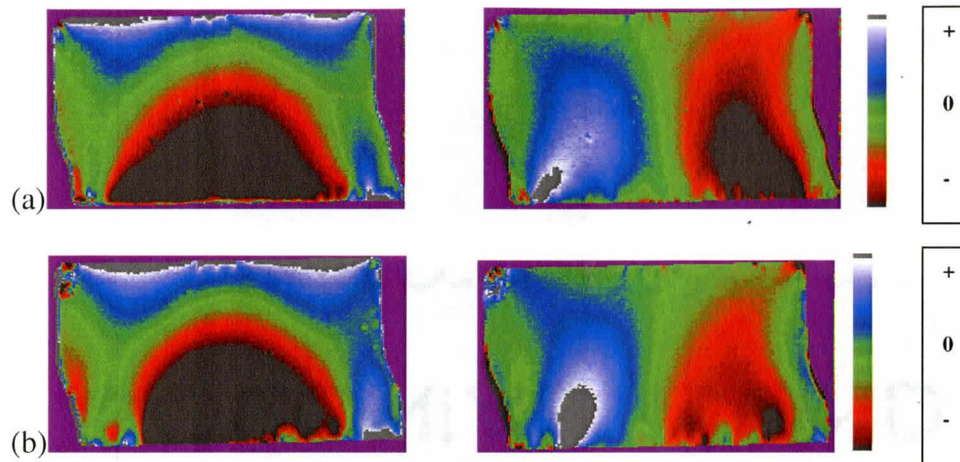

Figure 4.5. DOP (left column) and ROP (right column) of the laser facets for two devices. The ridge structure can be inferred from the top central pattern of the DOP scan.

5000 Hours

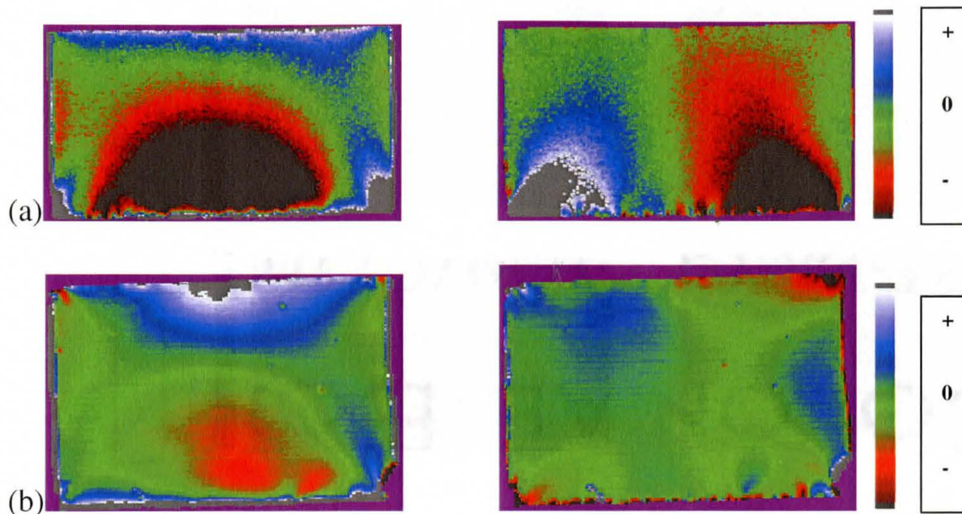

Figure 4.6. DOP (left column) and ROP (right column) of the laser facets for two devices. The bottom laser shows an absence of the dark region in the DOP scan. The dark region is characteristic of the shorter-tested samples. While this was not always present in the 4300 hours and 5000 hour samples, there were still more samples with this DOP distribution in the longer-tested groups (4300 hours and 5000 hours) than in the shorter-tested groups.

4.4. Discussion

The preceding images are false colour maps of DOP and ROP data. At the side of each figure is indicated the key to interpreting the colour: green hues are neutral (zero) values of DOP and ROP; while blue represents positive and red represents negative values. The grey and black regions are off-scale values, while the purple colour represents regions in the sample where the photoluminescence

was too low for a DOP or ROP signal to be resolved, such as occurs off the sample.

Figure 4.1. shows the DOP and ROP patterns from laser samples with a lifetime of 24 hours. The DOP pattern at the top shows considerable damage to the contact InGaAs layer. This was expected from previous work [18]. 12 of the 19 samples examined from this group, however, did not show obvious damage to the top of the device, near the active region.

The processing problem with the 24-hour devices involved overexposure to dielectric etch plasma. The step-by-step process in fabricating these devices is outlined below [18]:

1) After growth, the ridge is defined, the masking layer removed, leaving a bare semiconductor ridge about 30 microns wide.
2) Dielectric layers consisting of silicon oxide and then silicon nitride are applied to the wafer, and these coat everything including the sidewall of the ridge.
3) Areas away from the top of the ridge are protected by a resist mask, and a via is opened in the dielectric stack on the ridge with a dry etch plasma.

The problem with the 24-hour group devices is they underwent step (3) twice; there was some residual dielectric after initial processing and a short etch was

intended to try and remove it. However, the full etch was run, resulting in semiconductor erosion and subsequent damage.

The SEM images below, courtesy of Nortel Corporation, show the problem.

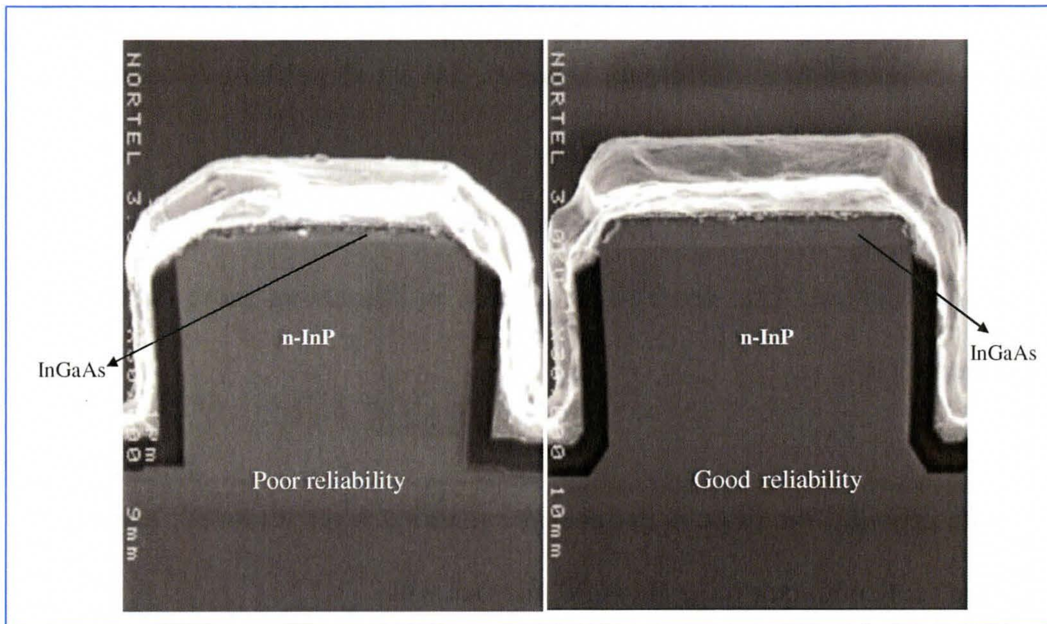

Figure 4.7. This figure shows the SEM images highlighting the poor contact issue mentioned above. The light region just below the metal (white region) is the InGaAs layer, which has been considerably thinned by over-etching on the device on the left hand side. Note the shape difference at the bottom corners of the ridge. The sharp corner of the devices on the left should create a higher strain environment near the bottom of the ridge compared to the corners of the devices on the right, which are pared off *Courtesy of Dr. Marcel Boudreau, InP MZ Design, Bookham Co Ltd.*

Comparing DOP maps from the different hour groups and focusing on the top of the facets, near the active region, one sees that the DOP values at the top

become larger as the life-test duration of the device decreases. This is indicated by the large grey off-scale values, which dominate the top of the facets in shorter-tested devices. An exception occurs in the 24-hour group, where the devices not obviously damaged show a DOP map comparable to the 3100-3200-hour groups. This implies that the poor performance of devices in the 24-hour group is due to the poor nature of the contact. Additionally, it can be seen from the SEM images in Figure 4.7. that the corners on devices from the 24-hour group are sharp, while those from the more reliable devices are pared off.

From this, it may be expected that the areas immediately beneath the ridges of devices in the 24-hour group should be under more strain than those in the other, more reliable devices owing to the shape of the metal and dielectric there.

A common occurrence in all devices is the blue region at the top. It is reasonable to attribute this to the strain induced by the metal on top on the InP below. Zhang et al. have studied how the stress in the metal changes with varied thickness [3]. The contribution of each metal layer on neighbouring metal is beyond the scope of this thesis. However, the coefficients of thermal expansion (CTE) of the metal stack (consisting of Au, Pt and Ti) at room temperature are on average more than double that of InP ($15.8\times10^{-6}\,K^{-1}$ is the average for the metals, while that of InP is $4.6\times10^{-6}\ K^{-1}$) [19]. As such, while the contribution of individual metal layers may possibly be tensile or compressive depending on the metal and the deposition conditions, it is expected that a resultant component will

be induced on the underlying semiconductor. From the false colour maps of the data collected, it can be seen that the metal stack gives a consistent sign for the DOP regardless of the details of its composition.

Given that the DOP_y is proportional to the difference in orthogonal strains in the x and z directions, it is not straightforward to determine the absolute values of the strain components. However, one can deduce the sense of the nature of the strain induced on the InP. The metal on top of the laser is deposited uniformly on semiconductor under elevated temperatures. In this case, it is reasonable to expect that, as the system cools, the metal will exert a compressive force on the underlying semiconductor.

Therefore, the blue regions at the top of the facet correspond to regions under compressive strain, which strain is likely caused by the metal layer. The bottom of the facets reveal more complicated DOP patterns. The varying regions of blue, green and red colouration means that the devices are under a high strain gradient both vertically and horizontally. This is evident in Figures 4.2(b), 4.3(b), 4.5(b) and 4.6(a), where there are 'arches' at the bottom consisting of lobes of blue, green and red. The complex patterns may be attributed to both the inhomogeneities in the deposited solder, as well as the fact that the die is not always completely attached to the solder: there is sometimes some semiconductor overhang, so that there is more solder to one side than the other.

This is related to another common feature to the DOP maps of most of the samples examined in this study is the blue lobes on the bottom corners. It is

believed this is also due to the fact that the Au-Sn bond does not extend across the entire bottom of the devices in all cases; rather, there is an overhang of semiconductor on at least one side of the devices.

The ROP maps are quite similar throughout the sampled devices, with a few exceptions such as shown in the last device of the 5000-hour group. The maps are essentially bisected by an imaginary line, with a lobe on each side opposite in polarity to the one on the other side. As will be shown in Chapter 6, these features can be attributed to both the bending of the InP, due to compressive strain induced by either the metal contact or the ceramic carrier; they may also be due to a torsion component owing to inhomogeneities in the solder in some instances.

The relationship between ROP_y and the shear strain is very straightforward and affords one the ability to interpret the ROP maps directly. From the data, it is clear that the tops of the facets are not under a lot of shear strain. There is a uniform green colour except in regions corresponding to the ridge. Shear strain is known to strongly impact device performance [25]. It was therefore expected that a correlation between ROP and device reliability would be observed. However, these images are very similar in most of the devices.

4.5. Summary

This chapter presented a qualitative discussion of the DOP and ROP maps gleaned from measuring the photoluminescence from the laser diodes. It was found that some of the devices in the 24-hour group showed extensive damage at the top contact region (near the active region). This was possibly due to the processing error that occurred during manufacture. From the DOP pattern, it was also observed that while all the devices showed a compressive strain near the top owing to metallisation, this was especially severe in shorter-tested devices. The DOP pattern near at the bottom was generally more complex due to the high strain environment and possible inhomogeneities in the Au-Sn solder. It was not possible to discern a pattern relating the device performance to the DOP map at the bottom of the device from the data collected for this thesis. However, mechanical stress generally originates at the junction between device chip and carrier [2]. The mechanical stress per unit length, S_{bond}, can be expressed as

$$S_{bond} = \left|\alpha_{th2} - \alpha_{th1}\right|\left(T_{bond} - T_a\right)Y_m \quad (4.1.)$$

where α_{th1} and α_{th2} are respectively the coefficients of thermal expansion for the device chip and carrier stem, T_{bond} and T_a are the bonding temperature (near the melting point of the solder) and the ambient temperature (the temperature at which the device operates); and Y_m is the Young's Modulus of the chip (nearly equal to that of the semiconductor). Consequently, the mechanical stress increases

with an increase in melting point of the solder; devices packaged at the melting point of a hard solder like Au-rich Au/Sn, which has a comparatively high melting point, should have a larger strain induced on them by the underlying carrier. It is known that solder-related degradations can cause sudden failure even in otherwise stable devices, that is, those that show no damage in the active region itself [2, 5]. It is possible that the absence of a correlation between the DOP pattern at the bottom and device performance is due to the fact that the strain induced at the bonding junction becomes less pronounced the higher up the device (the nearer the active region) one goes [5].

The ROP maps are similar across all devices in every hour group, and are characterised by an asymmetry due to a twisting moment caused by the solder. Since the tops of the facets are not under substantial shear strain, it is not thought that they would contribute to understanding the strain-related issues involved in device performance.

5. DOP and ROP Maps: Quantitative Analysis

5.1. Introduction

The previous chapter presented an overview of the general, salient features exhibited by the devices investigated for this thesis. It was a qualitative treatment. The purpose of this chapter is to introduce two useful metrics by which the lifetimes of the different devices could be categorised and explained.

5.2. Extracting Quantitative Information

While false colour DOP and ROP maps are quite a useful aid in visualising the effects of strain in a region of space, they can also be rather complex. The sheer volume of data makes it difficult to determine pertinent information that would distinguish one set of maps from another. It would therefore be useful to obtain a figure of merit by which devices from different hour groups may be distinguished. Such a figure of merit is afforded one by using an area average of the DOP and ROP, which corresponds to the average strain over that region.

The areas chosen to carry out this analysis are shown in figures 5.1. and 5.2. below. It seemed reasonable to expect the area close to the active region was important in determining the performance of the device. In order to obtain some measure of the change in DOP or ROP across space on the facet as well as eliminate the effect of different offsets for the different devices, it was necessary

to compare at least two regions. Defects due to handling tend to occur at the edges of the devices, and propagate their strain fields into regions close by. As such, apart from the top region, areas near the edges were avoided. The second area chosen was therefore located in the centre of the devices.

An area of $40\times 20\,\mu\text{m}^2$ was chosen over which to evaluate the average values. Two figures of merit, v and w, were determined by the following equations:

$$\begin{aligned} v &= m - t \\ w &= 2t - tl - tr \end{aligned} \qquad 5.1.$$

This process is designed to eliminate the offset, which varies from one measurement to another. v measures the strain gradient between the top and middle of the device; w provides a measure of the strain across the top of the device, comparing the %DOP value in the region just beneath the ridge to those to the left and right of it. It is therefore expected to pick up any influence that the varying thickness of metal stack atop the die should have.

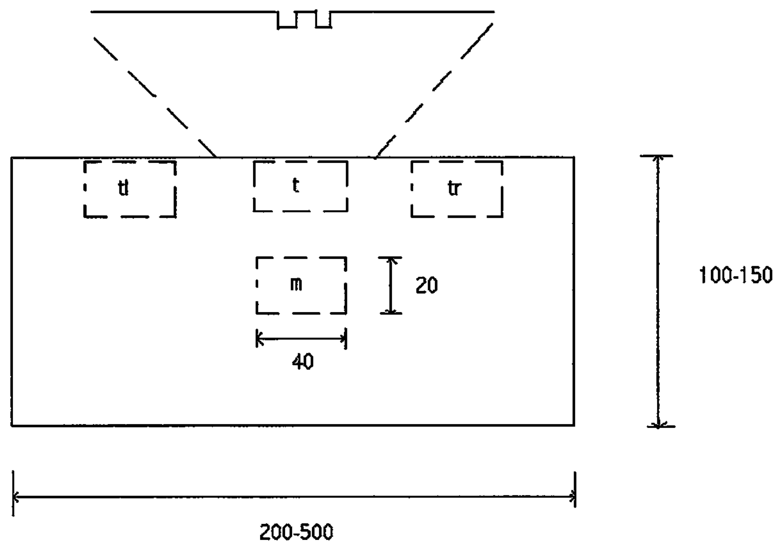

Figure 5.1. Areas used to determine average DOP and ROP values for the calculation of v and w. The zoomed region indicates the ridge waveguide structure. All measurements are in μm.

5.3. Results

5.3.1. The Influence of Number of Life-test Hours on v

Tables 5.1. and 5.2. show the v-values of devices in each hour group. Also indicated are the numbers corresponding to the wafer batch from which each device was derived. The v-values determined from ROP measurements are scattered, but those from DOP measurements are not. In fact, they show that the v-value becomes more positive on average the longer the life-test of the device. Consequently, it was decided to concentrate on DOP-derived v-values.

Lifetime / Batch	*v* (%DOP)	standard deviation of the mean	Ti(nm)	Pt(nm)
24 hours	**-2.82**	**0.58**	38	38
2400 hours				
Batch 1	-4.99	0.82	75	100
Batch 2	-4.39	0.74	50	100
mean	**-4.69**	**0.55**		
3100 hours				
Batch 1	-3.57	0.46	75	100
Batch 2	-3.61	0.43	50	100
mean	**-3.59**	**0.32**		
3200 hours				
Batch 1	-3.48	0.44	28	28
Batch 2	-3.09	0.42	28	50
Batch 3	-3.76	0.55	28	100
mean	**-3.44**	**0.27**		
4300 hours				
Batch 1	-2.17	0.32	28	28
Batch 2	-1.84	0.33	28	50
Batch 3	-2.53	0.47	28	100
mean	**-2.18**	**0.22**		
5000 hours				
Batch 1	-2.77	0.70	38	38
Batch 2	-2.18	0.22	38	38
Batch 3	-2.33	0.34	38	38
Batch 4	-2.06	0.19	38	38
Batch 5	-2.23	0.40	38	38
Batch 6	-2.08	0.35	38	38
mean	**-2.28**	**0.16**		

Table 5.1. ν-values for DOP data. The values are calculated from % DOP data. The thickness of metal contact is shown on the two right hand side columns. Au thickness is fixed at 564 nm.

Lifetime / Batch	*v* (%ROP)	standard deviation of the mean
24 hours	**0.0337**	**0.37**
2400 hours		
Batch 1	-0.138	0.16
Batch 2	-0.0110	0.14
mean	**-0.0856**	**0.22**
3100 hours		
Batch 1	-0.00533	0.12
Batch 2	0.184	0.069
mean	**0.0892**	**0.067**
3200 hours		
Batch 1	0.0615	0.076
Batch 2	0.0810	0.12
Batch 3	0.0892	0.025
mean	**0.0772**	**0.048**
4300 hours		
Batch 1	0.157	0.13
Batch 2	-0.0548	0.11
Batch 3	0.0832	0.12
mean	**0.0617**	**0.071**
5000 hours		
Batch 1	-0.105	0.10
Batch 2	0.0540	0.080
Batch 3	-0.0625	0.084
Batch 4	-0.0731	0.079
Batch 5	-0.0138	0.11
Batch 6	0.308	0.076
mean	**0.0179**	**0.033**

Table 5.2. v-values for ROP data. The values are calculated from % ROP data.

A one-tailed Mann-Whitney U test was chosen to evaluate the statistical significance of this result. It is a non-parametric test, although it does assume that the two distributions being compared are similar in shape. It calculates the statistic, U, which is used to test the null hypothesis that the difference between two groups of data is due to chance [20,21,22].

The ν-values from each device in each hour group were calculated and compared via the U test. The α, or significance, level was set at 0.025 for all evaluations of the U test. Table 5.3. below shows the results of this analysis.

There were 36 devices from the 5000-hour-group. This means that one can assume that this sample group has a normal distribution. The mean of this distribution as calculated from the ν-values of individual devices is -2.28 with a standard deviation of 0.16.

Comparison	Statistically significant?
24 hrs vs. 2400 hrs	Significant
24 hrs vs. 3100 hrs	Significant
24 hrs vs. 3200 hrs	Significant
24 hrs vs. 4300 hrs	Significant
2400 hrs vs. 3100 hrs	Significant
2400 hrs vs. 3200 hrs	Significant
2400 hrs vs. 4300 hrs	Significant
3100 hrs vs. 3200 hrs	Not significant
3100 hrs vs. 4300 hrs	Significant
3200 hrs vs. 4300 hrs	Significant

Table 5.3. This table shows the results of a one-tailed Mann-Whitney U test carried out on ν-values calculated from devices in the first five hour groups, excluding the 5000-hour group. The α-level was set at 0.025.

Comparing this value with those of the other groups, one finds that the means of the 24-hour, 2400-hour, 3100-hour and 3200-hour groups are respectively 3.25, 14.9, 8.06 and 7.12 standard deviations to the *left* of the mean of the 5000-hour group. The mean of the 4300-hour group is only 0.75 standard deviations to the *right* of the mean of the 5000-hour group.

Considering the first four cases, the probability of randomly obtaining a ν-value within this number of standard deviations from a sample from the 5000-hour group is very small. This can be seen at a glance from an assessment of the

values of the normal error integral. For instance, the probability that one could obtain a v-value equal to or less than -2.82 (the mean of the 24-hour group) is around 0.004.

Performing a similar analysis on the mean of the 4300-hour group shows that the probability of obtaining a mean within 0.75 standard deviations is 55%. It proved instructive to compare this with the result obtained using the Mann-Whitney U-test. The 36 devices from the 5000-hour group were randomly divided into two groups of 18 each and then compared to the devices from the 4300-hour group via a one-tailed U-test. The results were statistically insignificant at the 0.025 level. This was expected from the results of the normal distribution, which indicated that the probability of obtaining a v-value comparable to one in the 4300-hour group by choosing a device from the 5000-hour group was about the same as flipping a fair coin.

5.3.2. The Influence of Metal Thickness on v and w

The devices were organised into groups according to their metal thickness, and values of v and w were calculated for them.

Tables 5.4.,5.5., and 5.6. below show the influence of varying respectively the Pt and Ti thickness, and of keeping them both the same, but at only 38 nm. Indicated are the means and standard deviations thereof.

Pt=100 nm Ti=75 nm				
	Mean	standard deviation of the mean		
w (%DOP)	-0.048		0.26	
w (%ROP)	-0.397		0.10	
v (%DOP)	-2.61		0.18	
v (%ROP)	-0.118		0.083	
Pt=100 nm Ti=50 nm				
	Mean	standard deviation of the mean		
w (%DOP)	-0.0189		0.27	
w (%ROP)	0.610		0.092	
v (%DOP)	-2.89		0.19	
v (%ROP)	0.258		0.075	

Table 5.4. This table shows the effect of varying Ti thickness from between 75 nm and 50 nm for a fixed Pt thickness of 100 nm on the mean value of *w*(%DOP and %ROP) and *v*(%DOP and %ROP).

Pt=28 nm Ti=28 nm				
	Mean	standard deviation of the mean		
w (%DOP)	-0.0988		0.28	
w (%ROP)	0.150		0.093	
v (%DOP)	-2.33		0.19	
v (%ROP)	0.172		0.073	
Pt=50nm Ti=28 nm				
	Mean	standard deviation of the mean		
w (%DOP)	-0.181		0.26	
w (%ROP)	0.0591		0.11	
v (%DOP)	-2.03		0.17	
v (%ROP)	0.158		0.074	
Pt=100 nm Ti=28 nm				
	Mean	standard deviation of the mean		
w (%DOP)	0.355		0.43	
w (%ROP)	-0.0561		0.15	
v (%DOP)	-2.44		0.29	
v (%ROP)	-0.0765		0.11	

Table 5.5. This table shows the effect of varying Pt thickness from 28 nm to 100 nm for a fixed Ti thickness of 28 nm on the mean value of *w*(%DOP and %ROP) and *v*(%DOP and %ROP).

Pt=38 nm Ti=38 nm				
	Mean	standard deviation of the mean		
w (%DOP)	1.08		0.17	
w (%ROP)	0.0254		0.080	
v (%DOP)	-1.57		0.11	
v (%ROP)	-0.0160		0.058	

Table 5.6. This table shows the effect of a thin metal stack (Pt = Ti = 38 nm) on the mean value of *w*(%DOP and %ROP) and *v*(%DOP and %ROP).

The Mann-Whitney U-test was performed on *w*-and *v*-values for each device analysed from each metal-thickness group. None of the comparisons yielded statistically significant results for these metrics, except those between the *v*(%ROP) values of 100nm Pt/75 nm Ti and 100 nm Pt/50 nm Ti, for varying Ti thickness ($\alpha = 0.05$, two-tailed); between the *v*(%ROP) values of 28 nm Ti/28 nm Pt and 28 nm Ti/100 nm Pt for varying Pt thickness ($\alpha = 0.05$, two-tailed); and between *w*(%DOP) values of 28 nm Ti/50 nm Pt and 28 nm Ti/100 nm Pt for varying Pt thickness ($\alpha = 0.10$, two-tailed).

5.3.3. The Correlation of Degradation Rate to %DOP/ROP-derived Metrics

Degradation rates were calculated from slopes to linear fits to I_{th} (mA) vs. stress time (hours) plots [3]. The slope was evaluated post-100 hours of stress data since it was observed that there was an initial phase during which I_{th} decreased before resuming a linear increase [18].

The figures below show an example of such threshold-current vs. time plots.

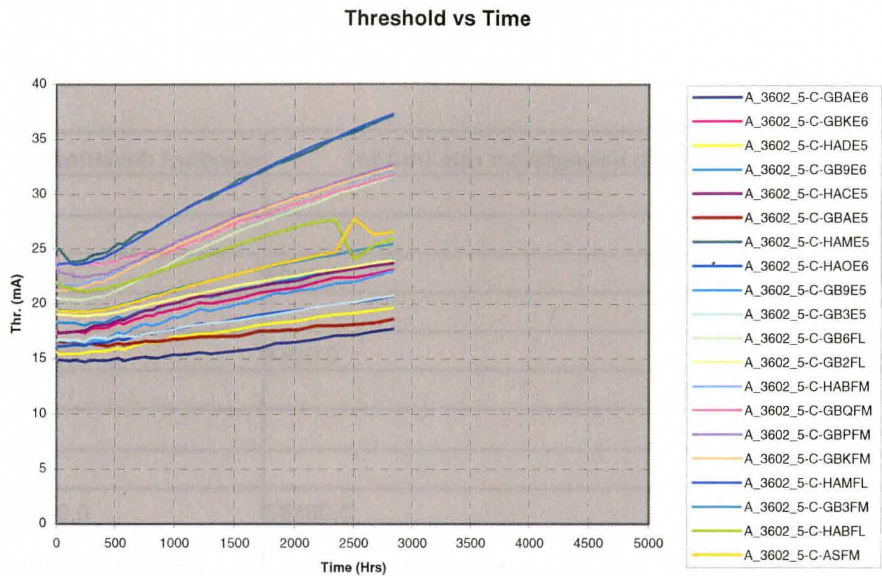

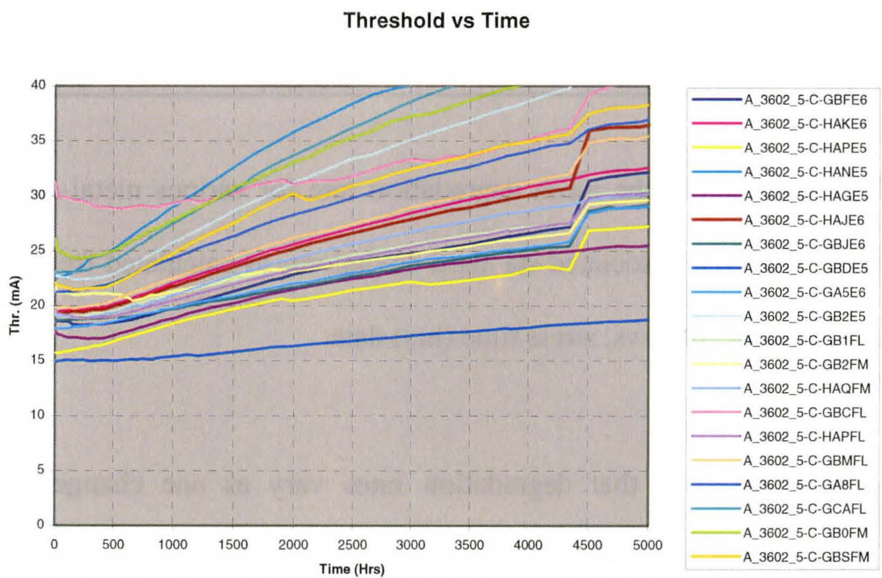

Figure 5.2. I_{th} (mA) vs (Stress) Time (hours) for the Pt = Ti = 38 nm metal stack.

Indicated are the unique device identifiers.

The tables below indicate the mean degradation rates for devices from different metal-thickness groups.

	Mean degradation rate (mA/hr)	standard deviation
Ti thickness, Pt= 100 nm		
Ti=75 nm	0.0267	0.00091
Ti=50 nm	0.0164	0.00023
Pt thickness, Ti=28 nm		
Pt=28 nm	0.00197	0.000025
Pt=50 nm	0.00489	0.00035
Pt=100 nm	0.00330	0.00015
Ti and Pt thickness		
Ti=Pt=38 nm	0.00229	0.000010

Table 5.7. This table shows the mean degradation rate for various metal-stack-thickness groups, and their associated standard deviations, as calculated from the slopes of linear fits to I_{th} (mA) vs. stress time (hrs) data.

While it is observed that degradation rates vary as one changes the composition of the metal stack atop the die, these variations are not statistically significant based on U-tests evaluated at the $\alpha = 0.05$ and 0.10 significance levels. The only exception was observed between the 28 nmTi/28 nm Pt and 28nm Ti/50 nm Pt metal-thickness-groups for varying Pt thickness.

Additionally, the degradation rates were compared to the metrics w and v derived previously to determine whether there was a correlation among them. The devices were compared by metal stack composition; for example, devices from batches in the 4300-hour and 3200-hour groups having a metal stack composition of 28 nm Ti/50 nm Pt were compared to their respective degradation rates.

No correlation was found between the degradation rate and either of the metrics w or v. A typical plot of the relationship between the two is shown below.

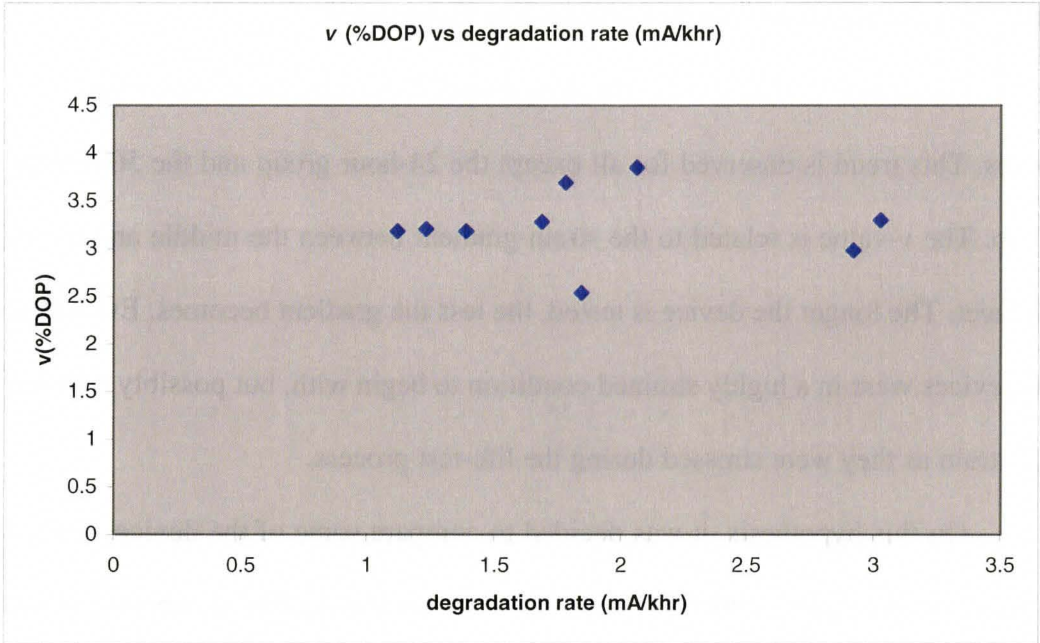

Figure 5.3.Typical plot of v(%DOP) vs. degradation rate (mA/khr).

A linear fit to this particular set of data yields an r-value of 0.0132 from 9 observations. If any two variables of a parent population are uncorrelated, the probability a random sample of N observations will give a correlation coefficient

for those two variables greater in magnitude than r is given by P_c. The values of P_c for given N and r are indicated in standard tables for the linear correlation coefficient [24].

Thus the probability of exceeding r from a random sample of uncorrelated data points is $P_c >> 50\%$. The data is hardly linearly correlated.

5.4. Discussion

5.4.1. The Influence of Number of Life-test Hours on ν

As shown in Table 5.1., the longer-tested devices have less negative ν-values. This trend is observed for all except the 24-hour group and the 5000-hour group. The ν-value is related to the strain gradient between the middle and top of the facet. The longer the device is tested, the less the gradient becomes. Evidently, the devices were in a highly strained condition to begin with, but possibly relieved this strain as they were stressed during the life-test process.

On this hypothesis, it was decided to compare some of the devices known to have not been aged, with their aged counterparts and determine whether or not these tended to have a more negative ν-value. These findings are summarised in the table below.

Life-test Duration/ Batch		v (%DOP)	Standard deviation of mean
2400 hrs			
Batch 1	aged	-4.95	1.7
	not aged	-5.03	1.3
Batch 2	aged	-4.08	0.85
	not aged	-4.71	1.2
3100 hrs			
	aged	-3.19	0.73
	not aged	-3.96	0.55
4300 hrs			
	aged	-2.00	0.46
	not aged	-2.34	0.46
5000 hrs			
Batch 1	aged	-2.19	0.29
	not aged	-2.17	0.34
Batch 2	aged	-1.74	0.54
	not aged	-2.73	0.59
Batch 3	aged	-1.98	0.40
	not aged	-2.22	0.62

Table 5.8. This table compares the v(%DOP) values for both aged and non-aged devices from each batch in each hour group.

At first glance, these results show that the aged samples in general have a less negative v-value than the non-aged samples. This implies that the strain gradient (the difference between the strain in the middle and at the top of the facet) is greater in non-aged than in aged samples; that is, aged samples show on average a higher %DOP value in the top region as compared to the middle region of the facets.

However, but for the case of the Batch 2 of the 5000-hour group, these differences are within the limits of experimental error. It is therefore possible that

such a difference is due to chance. Only three devices from each group (aged vs. non-aged) were measured, and therefore the U test could not be used at the level of confidence required ($\alpha = 0.025$) in order to resolve the difference.

Physically, the ν-value is a measure of the average strain gradient between regions at the centre of the device and those near the top. The evidence suggests a more negative ν-value is correlated with a shorter stress time for the device. Aging as well as annealing the device ameliorates its strain condition by allowing it to dissipate via various relaxations mechanisms, such as the formation of dislocations, resulting in a lower strain environment and more positive ν-value. In this sense, it seems reasonable to expect that the ν-values of aged devices should be more positive than those that have not been aged.

This is not borne out by the evidence collected.

However, the very consistent trend makes one reluctant to abandon the idea.

In sampling regions of DOP and ROP to make ν-value calculations, it was observed that the root mean square error values tended to be larger compared with the DOP or ROP value for that area the more the DOP or ROP varied. This was noticed since the ROP for the devices measured tended to be uniform over the same area and their rms errors correspondingly smaller. As such, these differences between DOP rms error and ROP rms error could not be attributed to noise within the system; rather, they were more likely to be from the inherent variation in DOP within the sampled region, as may be expected from the mathematics of

calculating the rms error. It therefore seems reasonable to expect that non-aged devices that have presumably not dissipated their strain will have a larger variation in the sampled regions compared to those devices that have been aged (and therefore dissipated their strain). This might be expected to exaggerate their rms value to a sufficient extent to cause the calculated ν-value to lie within experimental error of their aged counterpart.

The only batch for which the respective ν-values of the aged and not-aged samples do *not* fall within experimental error of each other are those in Batch 2 of the 5000 hour group, for which strain relaxation is significant, as can be seen from the difference between the ν-values. It is clear that the difference in their rms values is very small; in fact, it is small enough compared to the difference between the aged and non-aged ν-values for there to be no overlap due to experimental error. Therefore the author does not consider the argument for statistical insignificance due to experimental error to be sufficiently convincing to neglect the consistently more positive ν-values for the aged as compared to the non-aged devices.

It therefore seemed justifiable to pursue a further analysis of ν(%DOP).

The exception that occurs in devices from the 24-hour group is possibly due to two factors: the mistake made during processing, explained before; and the shape of the metal and dielectric (see Figure 4.7. above), which increases the amount of strain in the region just beneath the ridge. This leads to the device

showing a strain profile similar to one that has been aged between 3000 and 4000 hours as determined from its ν(%DOP).

The ν-values calculated for the 5000-hour group are more negative than those for the 4300-hour group. This is contrary to what one might expect given previous trends. However, the average ν-value from the 4300-hour group and that from the 5000-hour group are within experimental error of each other as indicated in Table 5.1. (-2.18 ± 0.22 for the 4300-hour group vs. -2.28 ± 0.16 for the 5000-hour group). There is the same life-test-hours difference between the 4300-hour devices and the 5000-hour devices as well as between the 2400-hour devices and the 3100-hour devices. This means that the ν-value can resolve the strain profile due to a difference in life-test hours of this magnitude, and that there must be other factors making distinguishing the former pair problematic.

Table 5.3. shows the results of the Mann-Whitney U test carried out on ν-values calculated from devices in the first five hour groups, excluding the 5000-hour group. The table indicates that there is no statistical significance between ν-values of devices in the 3100-hour group and of those in the 3200-hour group. This raises the possibility that the ν-value cannot resolve the strain profile between devices aged to such a small hour difference.

There were relatively many samples in the 5000-hour group, enough for one to assume a normal distribution. The mean of each hour-group, with the exception of the 4300-hour group, lies more than 3 standard deviations away from the mean of the ν-value of the 5000-hour group.

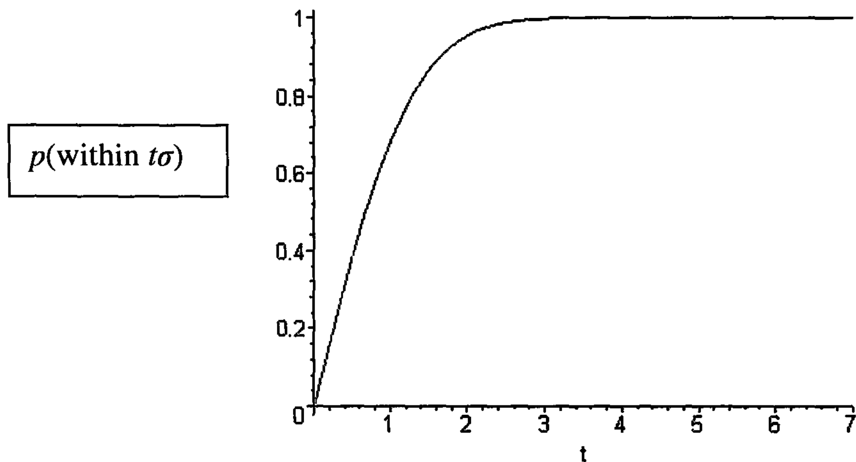

Figure 5.4. This figure shows the probability, p(within $t\sigma$) that a measurement will fall within t-standard deviations of the mean. It is evident that this probability rapidly approaches unity as t increases.

Figure 5.2. above shows the values assumed by the normal error integral, that is, the probabilities associated with measurements falling within t standard deviations of normally-distributed data. It is therefore highly unlikely to obtain ν-values with the means of the 24-, 2400-, 3100- and 3200-hour groups by sampling devices from the 5000-hour group.

However, there is a 55% chance that a randomly selected device from the 5000-hour group could result in a ν-value comparable to one in a 4300-hour group. This is consistent with the data in Table 5.1., which indicated that the mean values of the 4300-hour and 5000-hour groups were within experimental error of each other. It is also consistent with a U-test carried out to compare data from both groups; the test showed that the difference in ν-values between the devices

were not statistically significant at the 0.025 level, as might have been expected from the 55% probability figure. The difference in v-values between the two groups of devices is due to chance.

5.4.2. The Influence of Metal thickness on v and w

None of the comparisons between devices yielded statistically significant results under the U-test except for those between the v(%DOP) values of 100 nm Pt/75nm Ti and 100 nm Pt/50 nm Ti for varying Ti thickness (α = 0.05; two-tailed); v(%DOP) values of 28 nm Ti/28 nm Pt and 28 nm Ti/100 nm Pt for varying Pt thickness (α = 0.05; two-tailed); and w(%DOP) between 28 nm Ti/50 nm Pt and 28nm Ti/100 nm Pt for varying Pt thickness (α = 0.10; two-tailed).

In previous work [3], it was observed that maximum stress in the metal stack occurred 28 nm Ti/50 nm Pt, and 50nm Ti/100 nm Pt for varying Pt and Ti thickness respectively. As such, it makes sense that w(%DOP) comparisons with this group should yield some statistically significant results. However, it is surprising that none of the other w(%DOP or %ROP) yielded statistically significant results. As may be recalled, w is related to the difference in average strain just beneath the ridge compared to regions just either side of it. It is therefore reasonable to expect its value to be sensitive to changing metal thickness.

A possible reason may be that a change in metal thickness is such that it introduces a symmetrical change in the strain profile across the semiconductor

immediately beneath it. As such, any differences between the region just beneath the ridge, and those to the side of it would not be significant beyond what might be expected due to chance.

In general, however, the calculated metrics appear largely independent of metal thickness.

5.4.3. The Correlation of Degradation Rate to %DOP and %ROP-Derived Metrics

While previous work has shown a correlation between device reliability and %ROP, no correlation was observed between the degradation rate and the %DOP- and %ROP-derived metrics. The samples from previous work were not aged as long, typically several hundred hours. The devices investigated for this thesis, however, have been aged for at least 1000 hours. As such, it is possible that the extra annealing time masked strain-related effects.

5.5. Summary

This chapter has introduced a quantitative treatment of the data by defining two figures of merit, v and w. v is a measure of the change in strain between the top and middle of the device, while w is related to the strain profile across the top of the device; specifically, it measures the difference in strain between the region immediately beneath the ridge and the regions just to the right and left of the ridge.

The ν(%DOP) value is found to be a more useful metric. Longer-tested devices are found to have a more positive ν(%DOP)-value than shorter-tested ones. These differences in ν-value are found to be statistically significant at the 0.025 level by a one-tailed Mann-Whitney U test. Similar statistical tests find that the difference between the 5000-hour group and the rest of the hour groups is also significant. It was also found that aged samples have a less negative ν-value than non-aged samples. While consistent with the notion that strain relief mechanisms such as dislocation formation would reduce the strain difference between the top and middle of the devices, these differences were found to be negligible in comparison to experimental error. The exaggeration of the rms error due to a higher strain environment in the non-aged devices was posited to explain why such a conclusion was not definitive, especially given the consistent trend seen in the data and expected from the physics.

No correlation was observed between the metrics and device reliability. A possible reason for this is the extended aging time for the devices used in this study.

In general, the metrics appeared uncorrelated to the metal thickness, possibly because varying the metal thickness induced symmetrical changes in the underlying semiconductor, and taking differences between different regions to analyse these changes would therefore prove ineffective in picking them up.

Chapter 6: Finite Element Method and Fitting to Data

6.1. Introduction

This chapter explains the finite element method (FEM) used to fit to DOP and ROP data gleaned from the series of measurements carried out on the samples. The fits and general results are then presented.

As mentioned previously, the interpretation of DOP and ROP maps is not straightforward, as the DOP is proportional to the difference in strain or stress. Thus, a negative DOP value implies that $\varepsilon_{xx} > \varepsilon_{zz}$, but does not furnish information about the values of the components themselves. Therefore, unless one knows something about the samples in order to make certain simplifying assumptions (say, $\varepsilon_{xx} >> \varepsilon_{zz}$), getting quantitative information about the state of strain or stress from a map can be a problem.

The FEM is used to generate a model based on actual forces, and their resultant strain distributions. This model is then fit to the measured data in such a way as to minimise the chi-squared value in a manner analogous to ordinary regression.

6.2. Overview of the Finite Element Method

The FEM is rather similar to the finite difference method used for numerically solving partial differential equations (PDEs). As may be recalled, the finite difference method involves dividing the solution domain into a grid of

discrete points or nodes. A PDE is written for each node and its derivatives replaced by finite-divided differences. However, this method becomes unworkable when dealing with systems with irregular geometry, unusual boundary conditions, or variegated composition [25, 26].

The FEM is a more powerful technique, geared at solving for such systems. It involves dividing the solution domain into 'elements', simply shaped areas where an approximate solution to the PDE can be developed. The complete solution is then formed by seamlessly 'assembling' the individual solutions such that continuity is satisfied at the inter-element boundaries.

Therefore, a number of standard steps go into solving a PDE system using the FEM, and these are explained below.

6.2.1. Discretisation

As mentioned before, the solution domain is divided into finite elements [26]. The points at which the lines making up the sides of the elements intersect are called nodes, while the lines themselves are called nodal lines or nodal planes, depending on the dimensions of the system.

6.2.2. Approximating Equations

One then develops functions that approximate the solution in each element.

A suitable function with unknown coefficients that will be used to approximate the solution is chosen [25, 26].

It is then necessary to obtain an optimal fit of the chosen set of functions to the solution of the underlying differential equation. Several methods, analogous to curve fitting, are available to do this, for instance the variational approach, the method of weighted residuals and the direct approach. However, these methods, rather than fitting to data directly, specify relationships between the unknown coefficients that optimally satisfy the underlying PDE.

For many practical situations, the resulting element equations are a set of linear algebraic equations that can be expressed in matrix form.

6.2.3. Assembly

Contiguous elements are linked together in order to satisfy continuity: the solutions are matched so that the unknown values as well as the derivatives at their common nodes are equivalent. The final assembled solution is also a set of linear algebraic equations [25].

6.2.4. Boundary Conditions

One then modifies the system of equations generated in 6.2.3. by incorporating the relevant boundary conditions.

6.2.5. Solution

The system of equations thus generated in 6.2.4. is then solved by the usual techniques, for instance *LU* decomposition [25].

The solution can then be displayed in graphical or tabular format.

In general, the greater the number of elements used to solve the problem, the more accurate the resulting solution. However, increasing the number of elements comes at the cost of increasing computational resources, and so a trade-off needs to be made.

6.3. Fitting to Data

The DOP and ROP data was subjected to FEM fitting using a commercial package, FlexPDE 5.0™. The programme utilises a user-written script to turn a (first or second order) PDE, in one, two or three-dimensions, into a finite element model and present the output in both tabular and graphical form.

6.3.1. The System

The model developed to fit to the data uses the PDEs relating the stress and strain in an elastic material to the displacement they produce on points in the material [13,14]. That is:

$$
\begin{aligned}
U &: \frac{\partial}{\partial x}S_x + \frac{\partial}{\partial y}T_{xy} + \frac{\partial}{\partial z}T_{zx} = 0 \\
V &: \frac{\partial}{\partial x}T_{xy} + \frac{\partial}{\partial y}S_y + \frac{\partial}{\partial z}T_{yz} = 0 \\
W &: \frac{\partial}{\partial x}T_{zx} + \frac{\partial}{\partial y}T_{yz} + \frac{\partial}{\partial z}S_z = 0
\end{aligned} \tag{6.1}
$$

where U,V, and W are the displacements in the x, y and z directions, the S_i are the tensile stresses, while the T_{ij} are the shear stresses. These are related to the tensile and shear strains via the stiffness matrix so that [13,14]:

$$
\begin{aligned}
S_x &= c_{11}e_x + c_{13}e_y + c_{12}e_z \\
S_y &= c_{13}e_x + c_{33}e_y + c_{23}e_z \\
S_z &= c_{12}e_x + c_{23}e_y + c_{22}e_z \\
T_{xy} &= c_{44}g_{xy} \\
T_{yz} &= c_{44}g_{yz} \\
T_{zx} &= c_{66}g_{zx}
\end{aligned} \tag{6.2}
$$

where the e_i are the tensile strains and the g_{ij} the shear strains. Incidentally, the fourth rank modulus tensor that yields (4.2) has been rotated by 45° about the (001) axis as explained in Section 2.2.

The values of the constants in the stiffness matrix are (in N/m^2):

$$
\begin{aligned}
c_{11} &= 123.95\times10^{9} \\
c_{12} &= 35.55\times10^{9} \\
c_{13} &= 57.3\times10^{9} \\
c_{22} &= c_{11} \\
c_{23} &= c_{13} \\
c_{33} &= 102.2\times10^{9} \\
c_{44} &= 44.2\times10^{9} \\
c_{66} &= 22.45\times10^{9}
\end{aligned} \tag{6.3}
$$

The grids were set to be finer near to the surface of the devices (since DOP and ROP are sampled from regions close to the surface) as well as at the periphery of the facets (since it was observed that DOP and ROP changed more rapidly at the top and bottom edges of the devices).

The strains, e_i, were written as a linear combination of simple polynomials and applied to different parts of the model as appropriate in order to generate the strain distribution that best replicates the DOP and ROP data. Similarly, both Dirichlet and natural boundary conditions were specified to achieve an optimal solution.

FlexPDE was configured to output both tabular and graphical information. Using equations (2.14) and (2.17) allows for the presentation of DOP and ROP data directly from the solution of (6.1) using the relationship between strain and displacement. FlexPDE has a feature that allows the user to monitor the state of the solution. The contribution of each of the basis functions used to approximate the e_i is displayed in both graphical and tabular form. The tabular output is

essentially a text file containing an array of DOP and ROP values. This can be converted into a format that the fitting routine built into X3D can interpret.

The fitting routine finds the combination of functions and coefficients that best matches the measured data. This amounts to a least-squares fit to two arbitrary functions, with the functions being the DOP and ROP values at each point in the dataset. The task, then, is to minimise the difference between the data from each point in the measured pattern and a linear combination of the modelled data. That is, one seeks to minimise [5]:

$$\chi^2 = \sum_{j=1}^{n} \left\{ y_j - \sum_{i=1}^{m} a_i x_{ij} \right\}^2 \qquad (6.4)$$

where χ^2 is the sum of the squares of the difference between the measured and a linear combination of the modelled values; y_j is one of n measured values on the facet; x_{ij} is one of the n modelled values of the facet due to m applied forces; and a_i one of m linear coefficients. The fitting routine is searching for the a_i that minimise χ^2.

6.3.2. Modelling

Before beginning carrying out the finite element method and subsequent fitting routine, it was first necessary to come up with a model on which to approximate the strain conditions of the facets.

From the processing details, one can see that the devices are mostly InP [3]. As such, the model presented is of a rectangular block of InP subjected to traction forces at various points on its perimeter, which forces are due to metallisation, the action of the thin dielectric at the top of the device as well as due to the action of the bonding Au-Sn solder at the bottom of the chips. An example of the forces applied to the die for the simulation is shown in Figure 6.1. below:

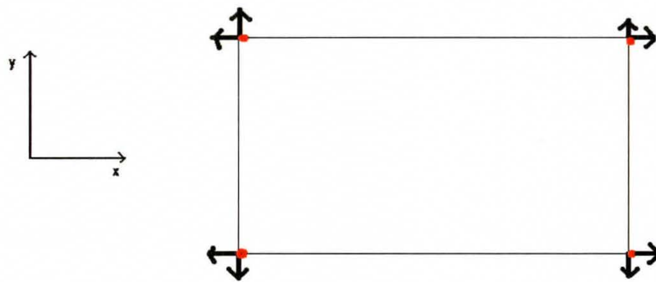

Figure 6.1. This figure indicates typical traction forces applied to the model to fit to the DOP and ROP data from the measurements carried out for this thesis. Indicated also are the axes systems used. The red points represent forces out of the plane of the paper (in either the positive or negative z-direction). Note that the directions and numbers of the forces indicated are simplified. Depending on the particular device, there may be as many or fewer forces, and in different directions.

Note that, for the simulation, the axes were defined differently from how they were defined in Chapter 1. The *y*-axis here corresponds to the *z*-axis in Chapter 1. Thus the plane of the facet in the *x-y* plane rather than the *x-z* plane as before. The strains in the respective plots are defined differently from Chapter 1, with

$$
\begin{aligned}
e_x &\equiv \varepsilon_{xx} \\
e_y &\equiv \varepsilon_{zz} \\
e_z &\equiv \varepsilon_{yy} \\
g_{xy} &\equiv \varepsilon_{xz} \\
g_{yz} &\equiv \varepsilon_{zy} \\
g_{zx} &\equiv \varepsilon_{yx}
\end{aligned}
$$

And so on.

However, discussions in the following sections will preserve the coordinate system introduced in Chapter 1.

Also note that the positions of the forces indicated in Figure 6.1. above are simplified. Assuming that the strain induced on the die has as its point of origin the point of application of the traction forces, it was often necessary to offset some of these forces long the *x*-direction in order to account for die overhang. This will be clarified by an example. As mentioned before, linear expansions of simple polynomials were used. An expression linear in *x*, *pt(x)* was defined as:

$$pt(x) = \frac{2x}{wc} - 1 \qquad (6.5.1)$$

where wc is the width of the chip. One can see that this expression is dimensionless and normalised to the width of the chip. One then expands the strains in powers of $pt(x)$. By subtracting off a constant, xi, one can shift the point of application of the various forces (and therefore the origin of the strains):

$$pt(x) = \frac{2(x - xi)}{(wc - 2xi)} - 1 \qquad (6.5.2)$$

xi varied depending on the sample being fit to.

6.4. Results

The figures below present the DOP and ROP images derived from fits to the data. The DOP and ROP images derived from the data are juxtaposed for comparison.

5000 hours

DOP $\chi^2 = 347$

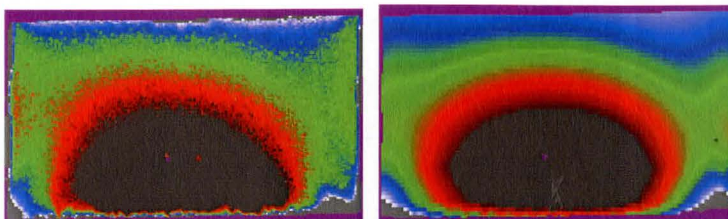

ROP $\chi^2 = 200$

(a) 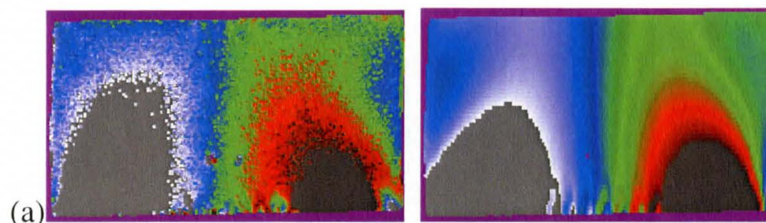

DOP $\chi^2 = 247$

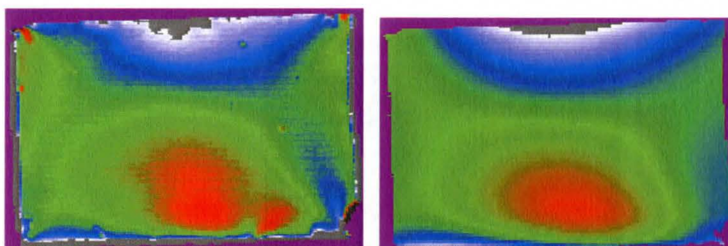

ROP $\chi^2 = 165$

(b) 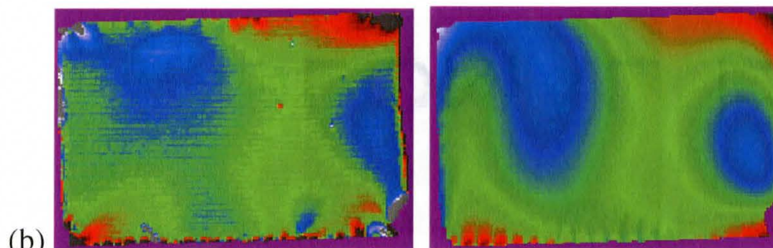

Figure 6.2. (a) and (b) show the DOP and ROP maps on the left column and their corresponding fits on the right for two different devices.

3100 hours

DOP $\chi^2 = 343$

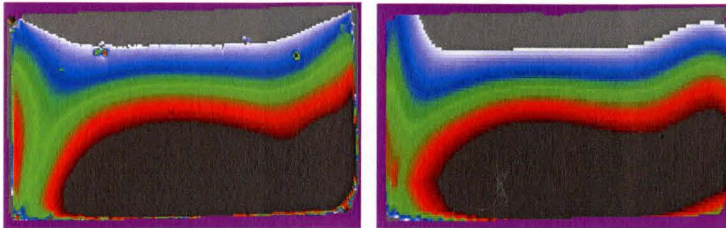

ROP $\chi^2 = 192$

(a) 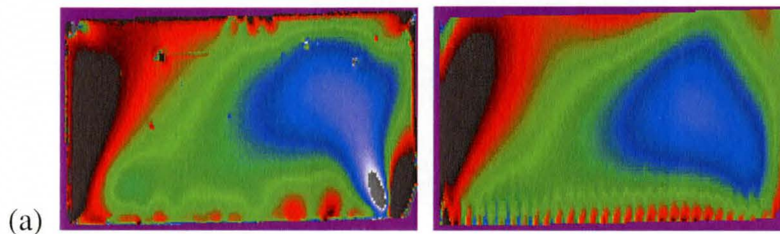

DOP $\chi^2 = 338$

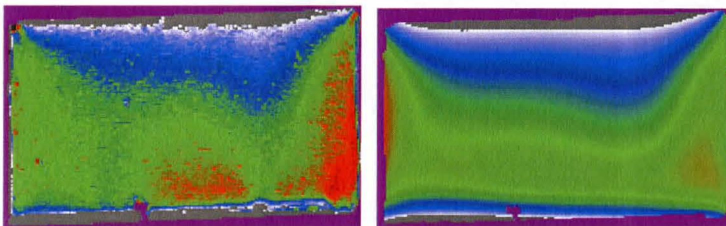

ROP $\chi^2 = 184$

(b) 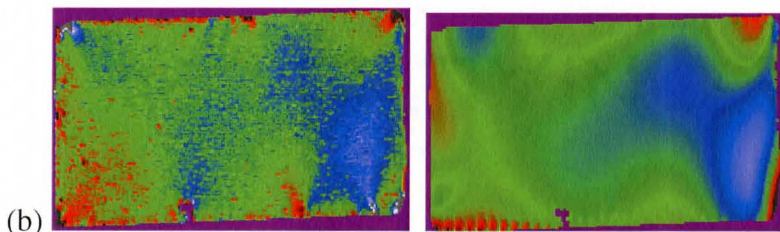

Figure 6.3. (a) and (b) show the DOP and ROP maps on the left column and their corresponding fits on the right for two different devices.

2400 hours

DOP $\chi^2 = 362$

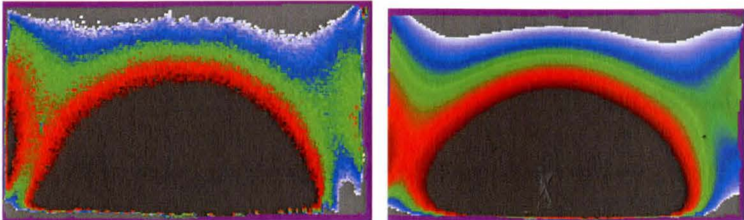

ROP $\chi^2 = 199$

(a)

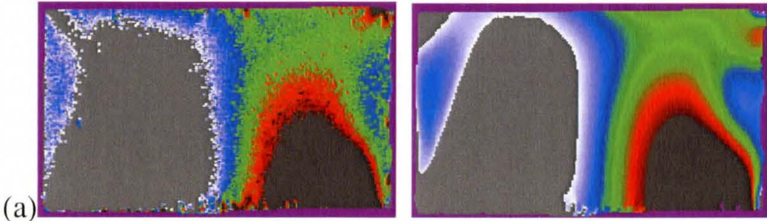

DOP $\chi^2 = 351$

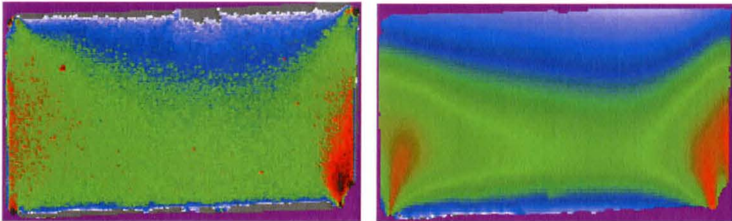

DOP $\chi^2 = 205$

(b)

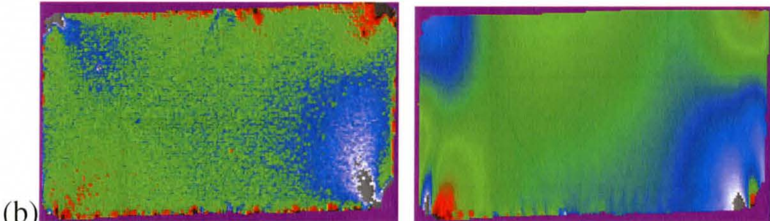

Figure 6.4. (a) and (b) show the DOP and ROP maps on the left column and their corresponding fits on the right for two different devices.

6.4.1. Discussion: Strain Plots Extracted from DOP Fits

The series of figures below show the ε_{xx} and ε_{zz} plots extracted from FlexPDE for the DOP data above.

Briefly, the series shows the strain profile at different sections of the given device as determined from the finite element method. The sections are sampled at regular intervals, from one-tenth, three-tenths, one-half, seven-tenths and nine-tenths of the height of the chip.

5000 hours (a) las2

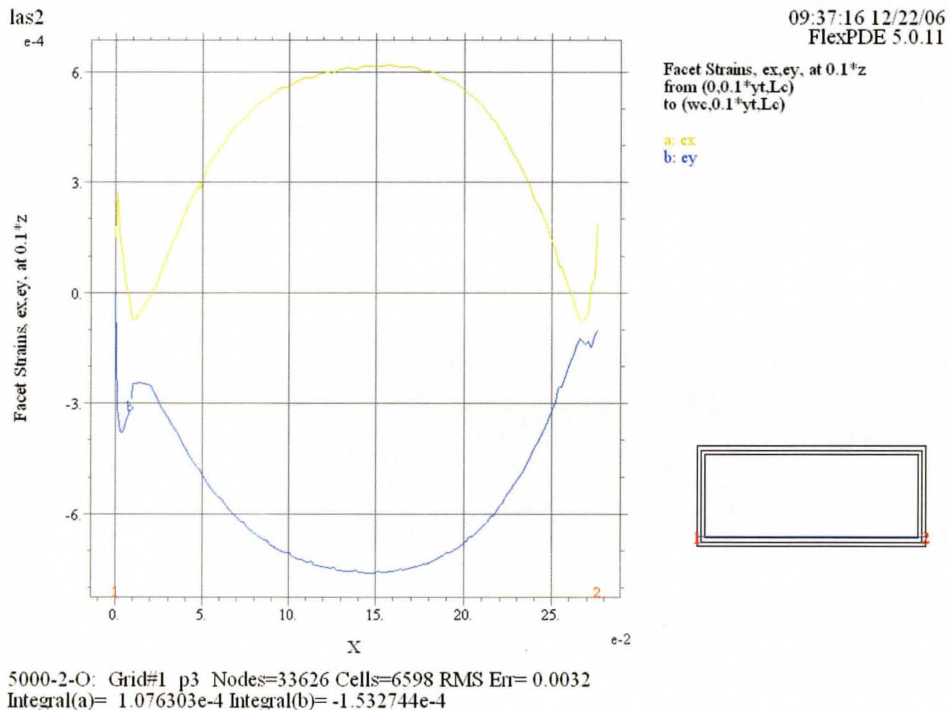

(a)

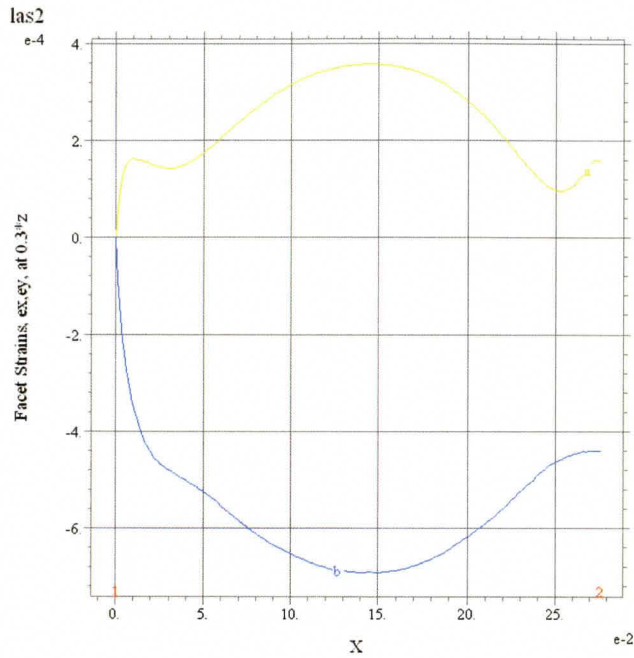

5000-2-O: Grid#1 p3 Nodes=33626 Cells=6598 RMS Err= 0.0032
Integral(a)= 6.606248e-5 Integral(b)= -1.564380e-4

(b)

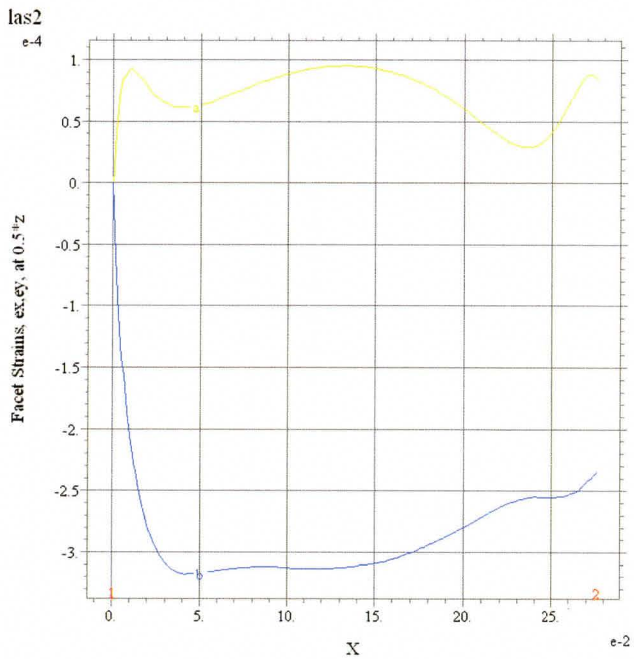

5000-2-O: Grid#1 p3 Nodes=33626 Cells=6598 RMS Err= 0.0032
Integral(a)= 1.969553e-5 Integral(b)= -7.872882e-5

(c)

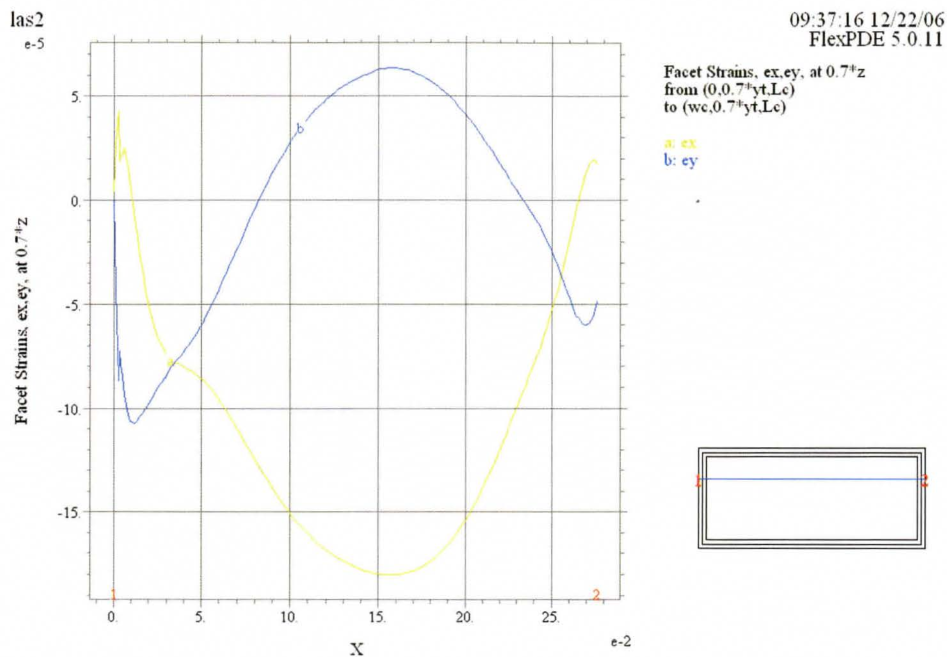

(d)

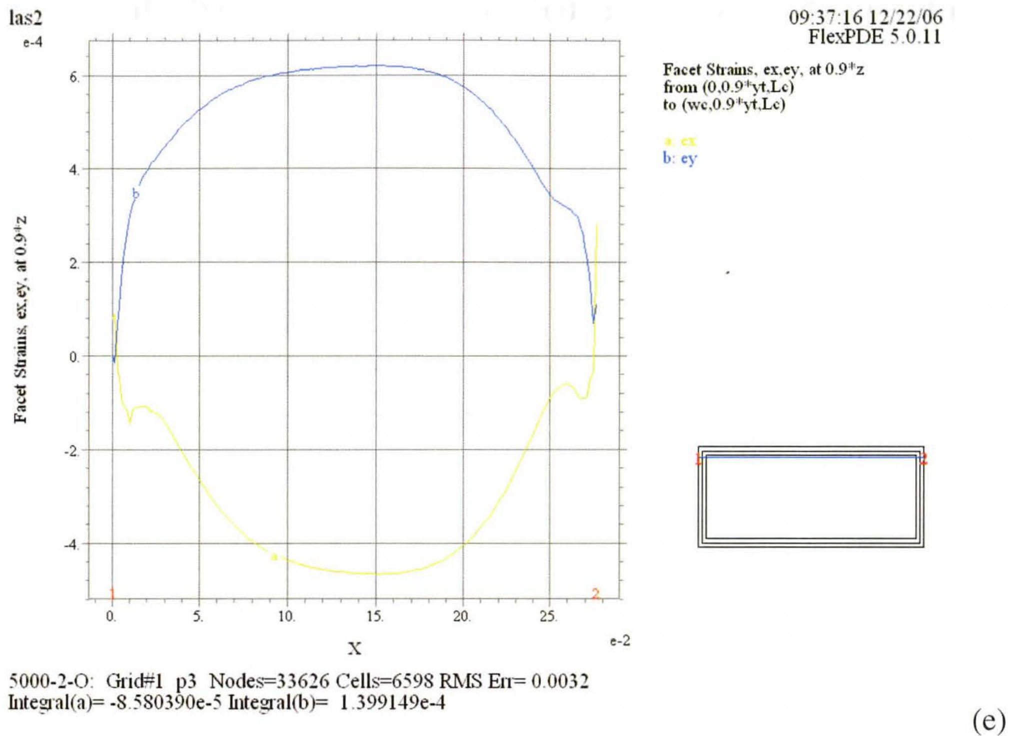

(e)

Figure 6.5. (a) - (e) This series of plots shows the strain profile along horizontal sections taken 0.1, 0.3, 0.5, 0.7, and 0.9 times the height, *yt*, of the device. As noted before, $ey \equiv \varepsilon_{zz}$.

This series of plots can be analysed by tracking the behaviour of a unit cell along the central line bisecting the device. Proceeding this way reveals that regions near the bottom of the device are under compressive ε_{zz} strain while those at the top are under ε_{zz} tensile strain. Evidently, there is a region of the device not under ε_{zz} strain. A similar analysis performed on the ε_{xx} strain reveals the opposite trend: The regions near the bottom are under tensile ε_{xx} strain, while those near the top are under compressive ε_{xx} strain. A map of imaginary vertical planes in this region would show a bottleneck effect, with the narrow end at the top.

The figure below shows the strain profile in a vertical section through the middle of the device.

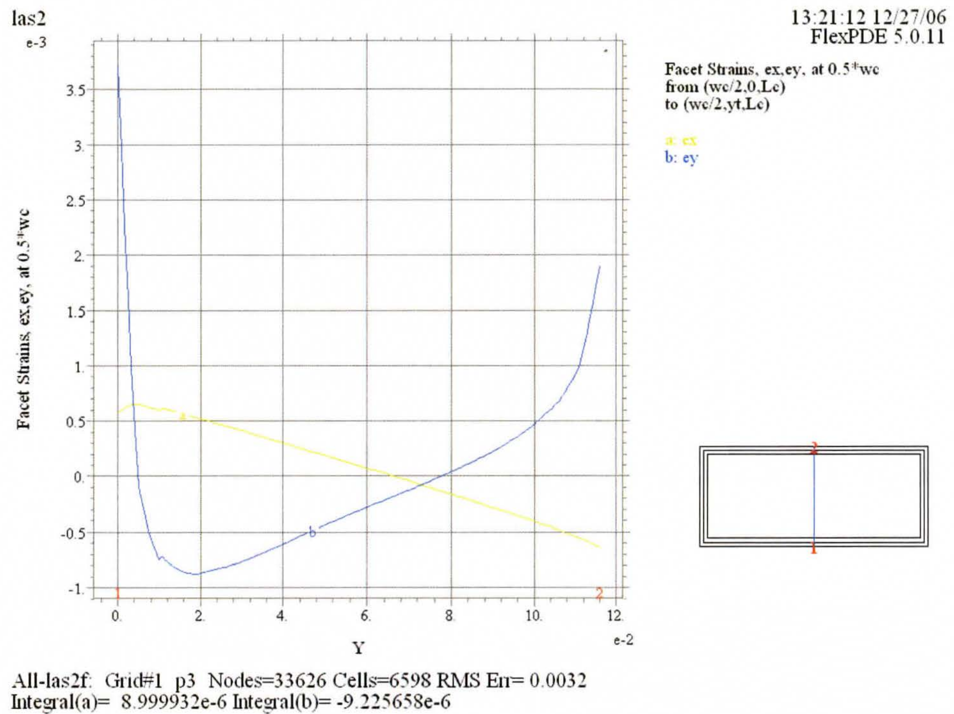

Figure 6.6. This figure shows the strain profile through a vertical section through the middle of the device. As before, $ey \equiv \varepsilon_{zz}$. The profile evalutated at 0.25 and 0.75 the width, *wc*, of the facet remained similar in shape.

The diagram below shows the distortion to the facet that causes these strains.

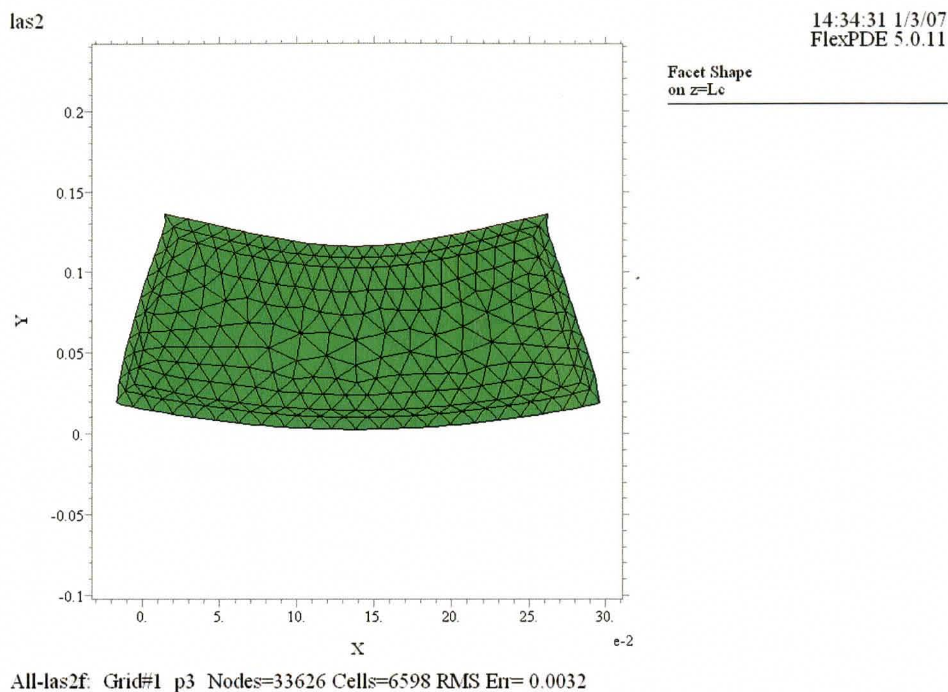

Figure 6.7. This diagram shows the distortion to the facet that causes the strains calculated in Figure 6.4. (a) – (e). As established before, the *y*-axis here is the *z*-axis in the discussion.

As is evident from the diagram above, the device experiences an overall bending motion. This seems consistent with a lateral expansion of the ceramic carrier. This would induce a tensile ε_{xx} strain near the bottom of the facet. From general elasticity considerations, this tensile strain would cause a compressive ε_{zz} strain, as observed.

5000 (b) las6

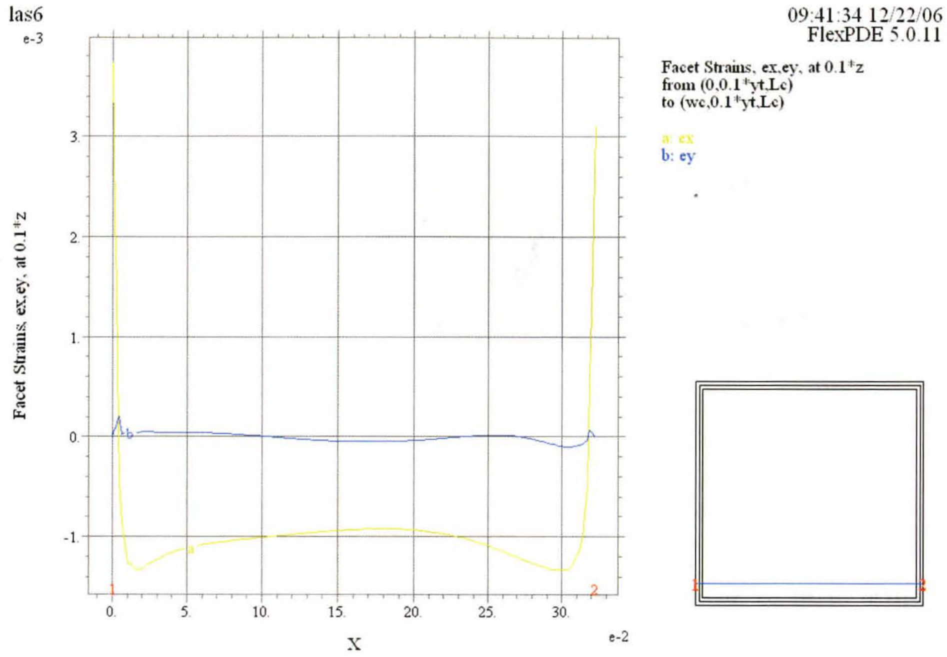

(a)

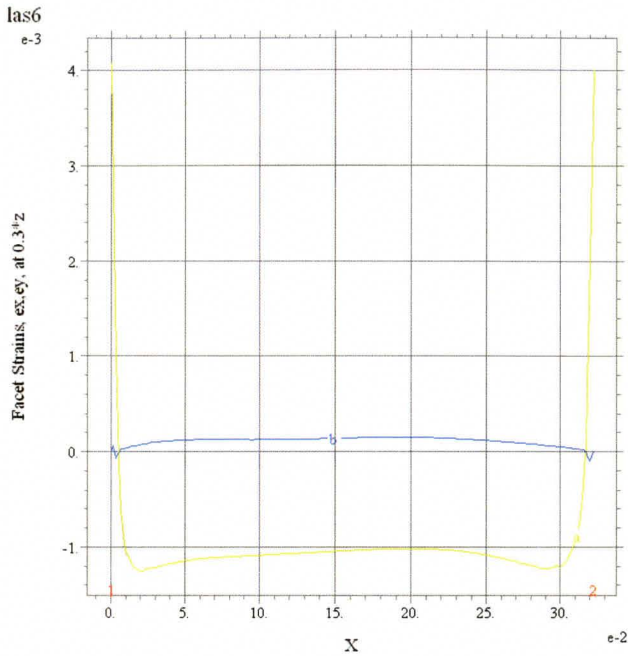

09:41:34 12/22/06
FlexPDE 5.0.11

Facet Strains, ex,ey, at 0.3*z
from (0,0.3*yt,Lc)
to (wc,0.3*yt,Lc)

a: ex
b: ey

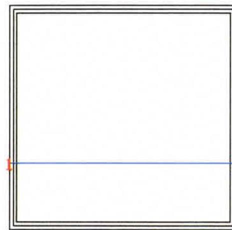

5000-6-O: Grid#1 p3 Nodes=73400 Cells=14746 RMS Err= 0.0119
Integral(a)= -3.190634e-4 Integral(b)= 3.633539e-5

(b)

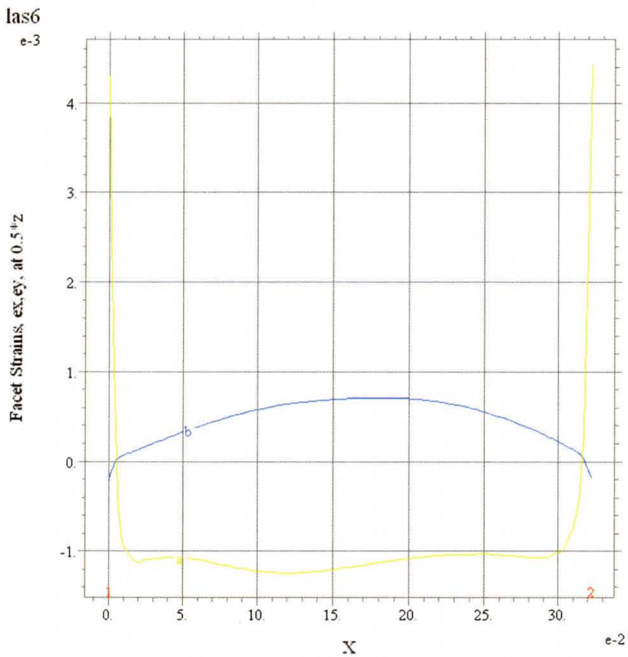

09:41:34 12/22/06
FlexPDE 5.0.11

Facet Strains, ex,ey, at 0.5*z
from (0,0.5*yt,Lc)
to (wc,0.5*yt,Lc)

a: ex
b: ey

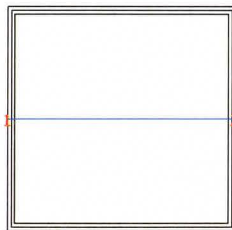

5000-6-O: Grid#1 p3 Nodes=73400 Cells=14746 RMS Err= 0.0119
Integral(a)= -3.189818e-4 Integral(b)= 1.530356e-4

(c)

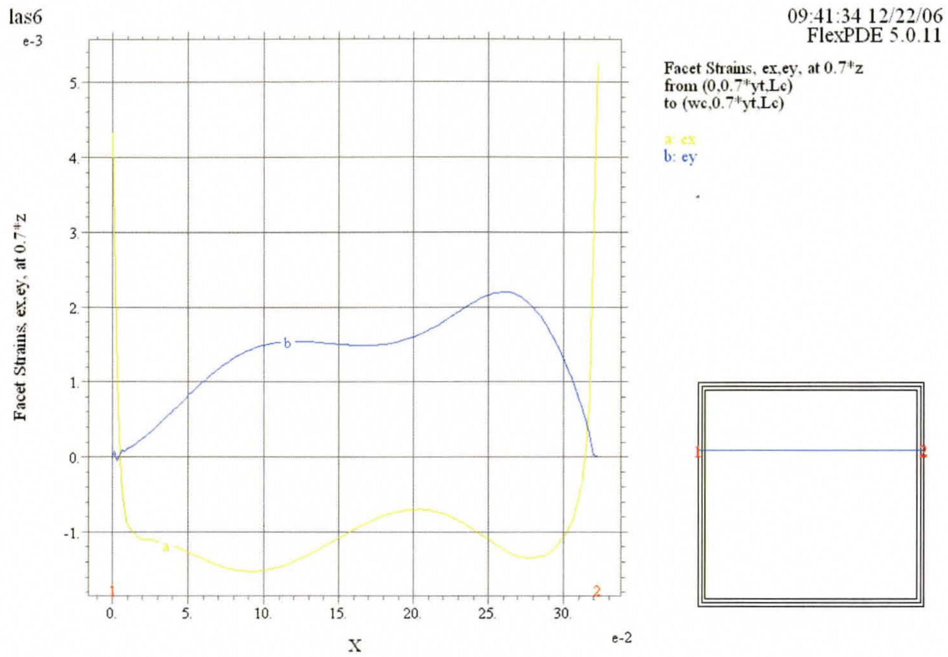

(d)

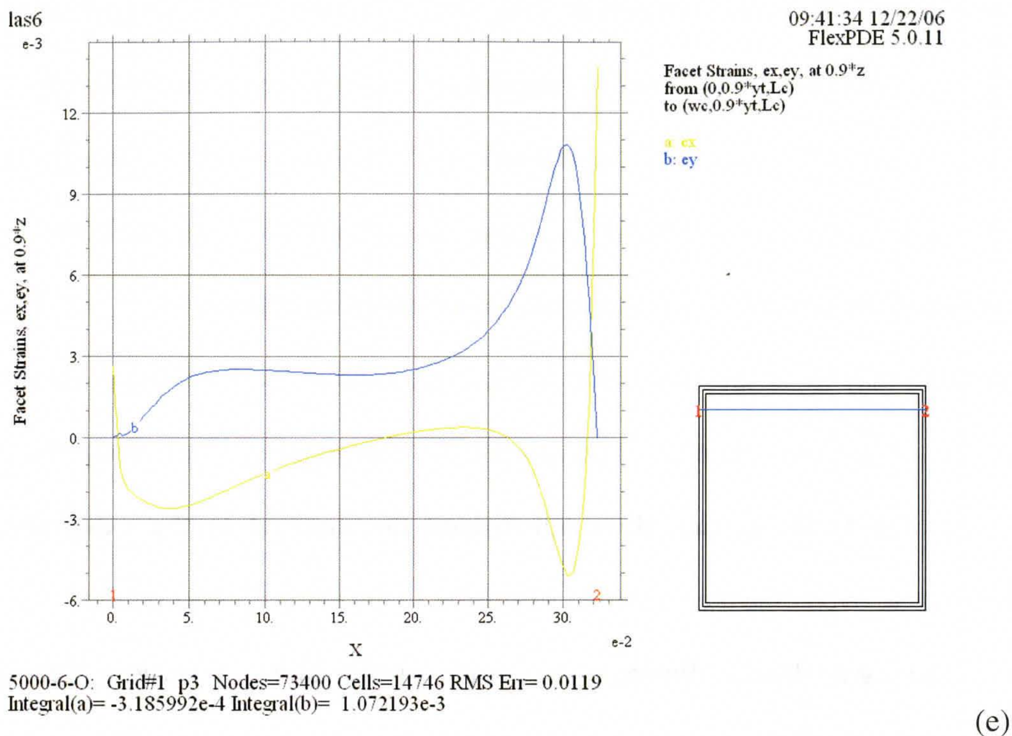

(e)

Figure 6.8. (a) - (e) This series of plots shows the strain profile along horizontal sections taken 0.1, 0.3, 0.5, 0.7, and 0.9 times the height, *yt*, of the device. As noted before, $ey \equiv \varepsilon_{zz}$.

This device shows less compressive strain in the ε_{zz} direction at the bottom than the previous one. The majority of the device as one moves from the bottom is under tensile ε_{zz} strain. Additionally, the magnitude of the ε_{zz} strain increases the higher up the device one goes from a value very nearly zero at the bottom. The material is also consistently under compressive ε_{xx} strain, though this decreases in magnitude near the top.

The semiconductor at the top of the device is under compressive ε_{xx} strain, possibly due to the metal contact on top. Compression in the *x*-direction accounts

for the tensile strain in the z-direction. This view is reinforced by the observation that the respective strains diminish in magnitude as one moves down the device.

It is not very clear why the material at the bottom is simultaneously in compressive ε_{xx} and a compressive ε_{zz} strain. A compressive ε_{xx} strain should be accompanied by a tensile ε_{zz} strain from linear elasticity arguments. A possible explanation may lie in the interaction of the force exerted by the carrier with the force due to the metal contact. Presumably the compressive force along the x direction, due to the carrier, does not distend the material in the z-direction sufficiently to overcome the tensile ε_{zz} strain due to the metal contact on top.

The figure below illustrates the strain profile along a vertical section through the middle of the device.

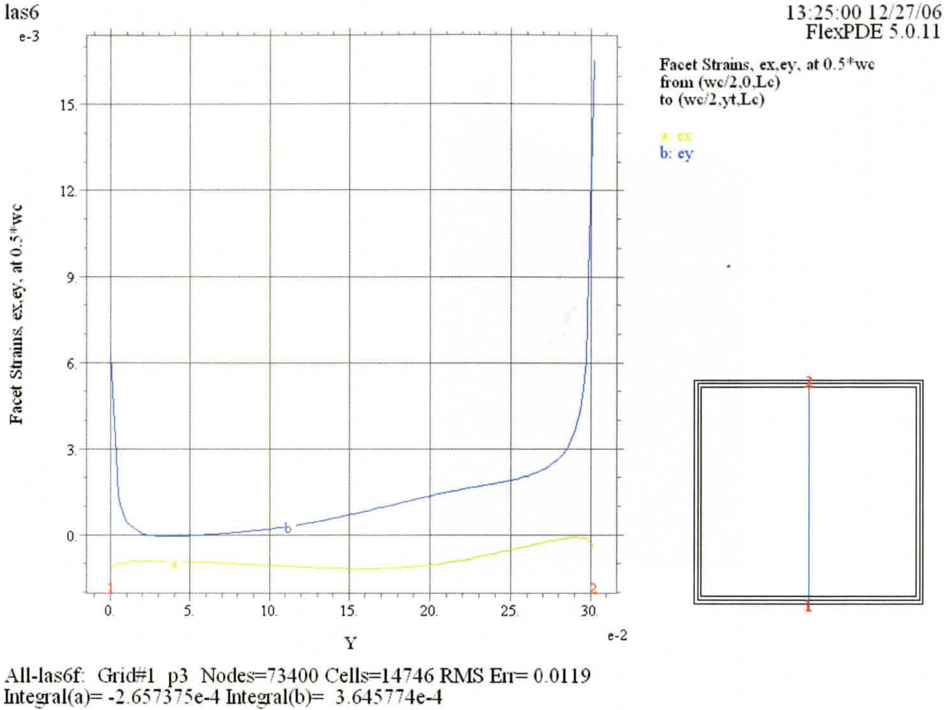

Figure 6.9. This figure shows the strain profile through a vertical section through the middle of the device. As before, $ey \equiv \varepsilon_{zz}$. The profile evalutated at 0.25 and 0.75 the width, wc, of the facet remained similar in shape.

The diagram below shows the distortion to the facet that causes these strains.

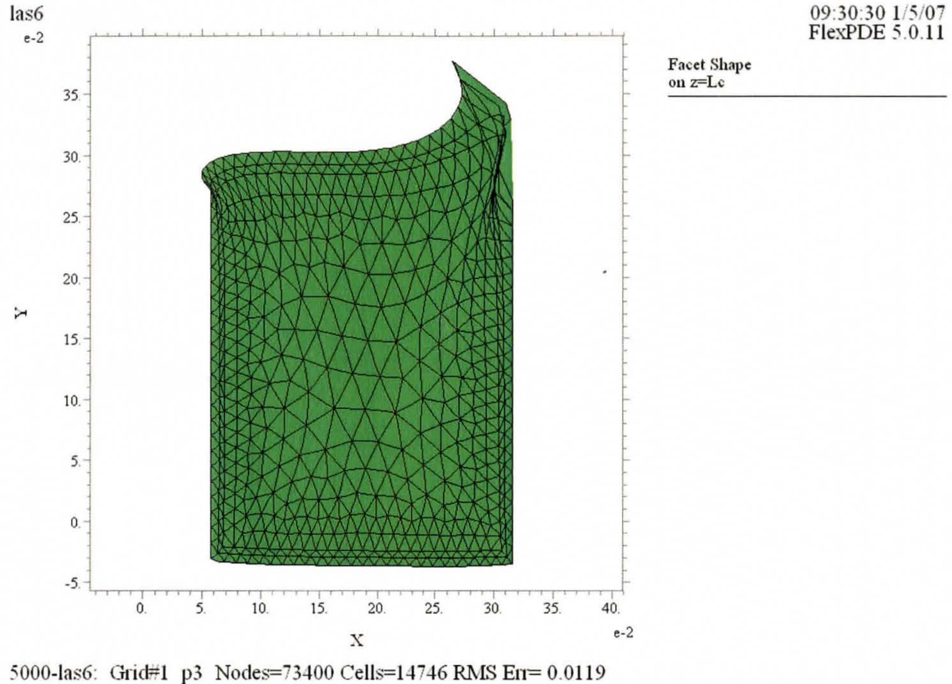

Figure 6.10. This diagram shows the distortion to the facet that causes the strains calculated in Figure 6.7. (a) – (e). As established before, the *y*-axis here is the *z*-axis in the discussion.

The figure above shows the device to be in compressive ε_{xx} strain, which causes it to be generally distended in the *z*-direction (the initial, undistorted grid had a square profile). However, the bottom of the facet shows a slight bending, which may account for the compressive ε_{zz} strain that was observed.

An interesting feature is also observed at the top of the device. It seems likely that the curvature observed to the right-hand side is due to the non-uniform deposition of metal contact. This will lead to both the torsion and asymmetric bending that will be mentioned later.

3100 hours (a) las2

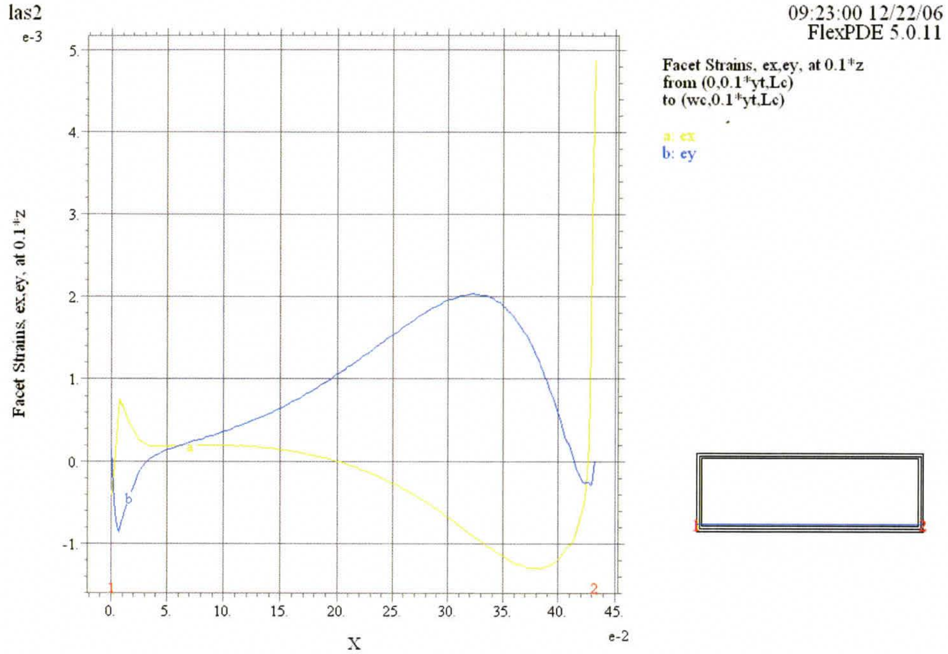

(a)

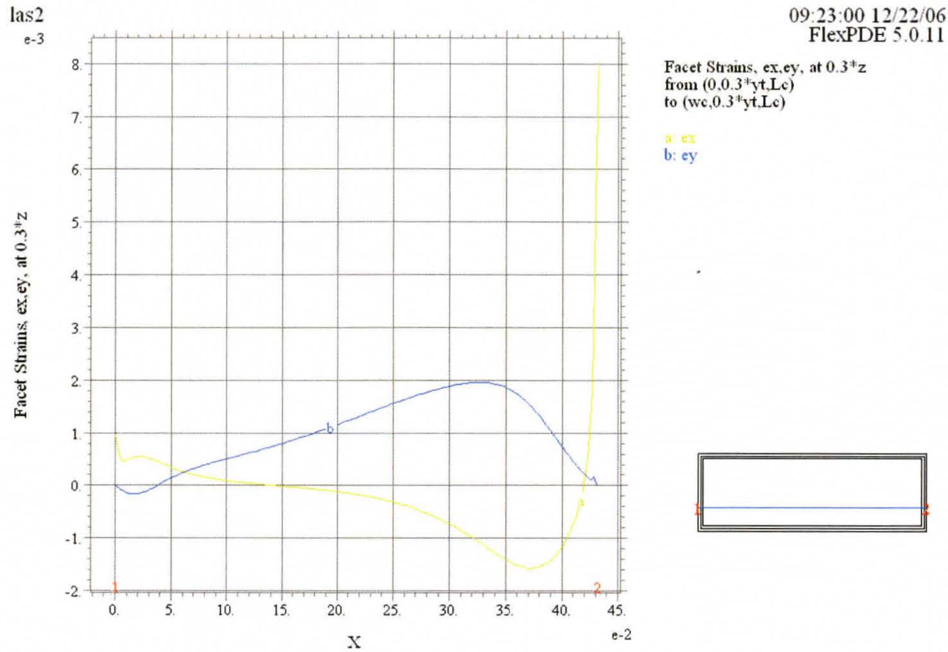

(b)

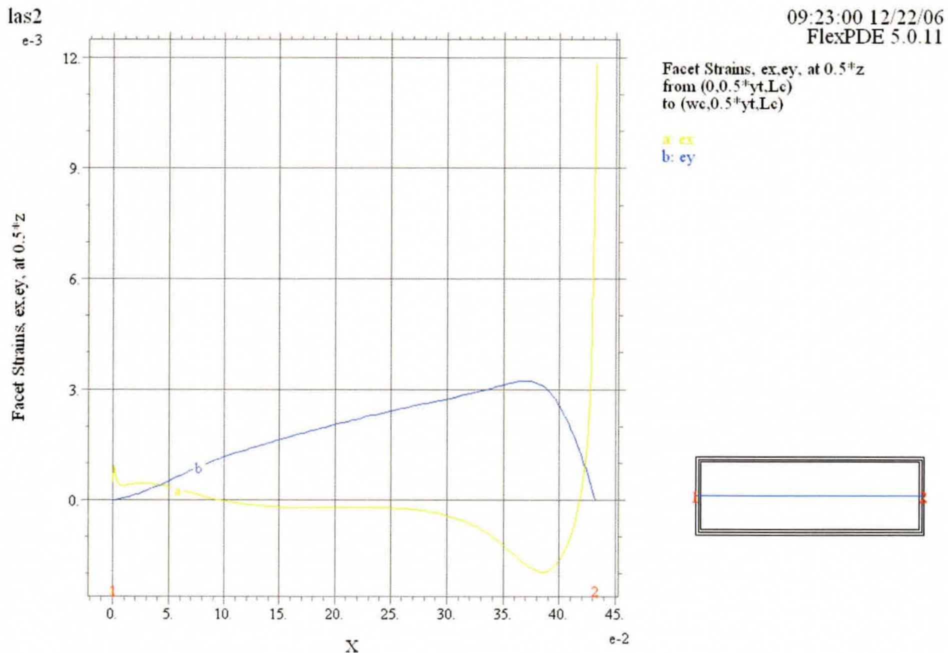

(c)

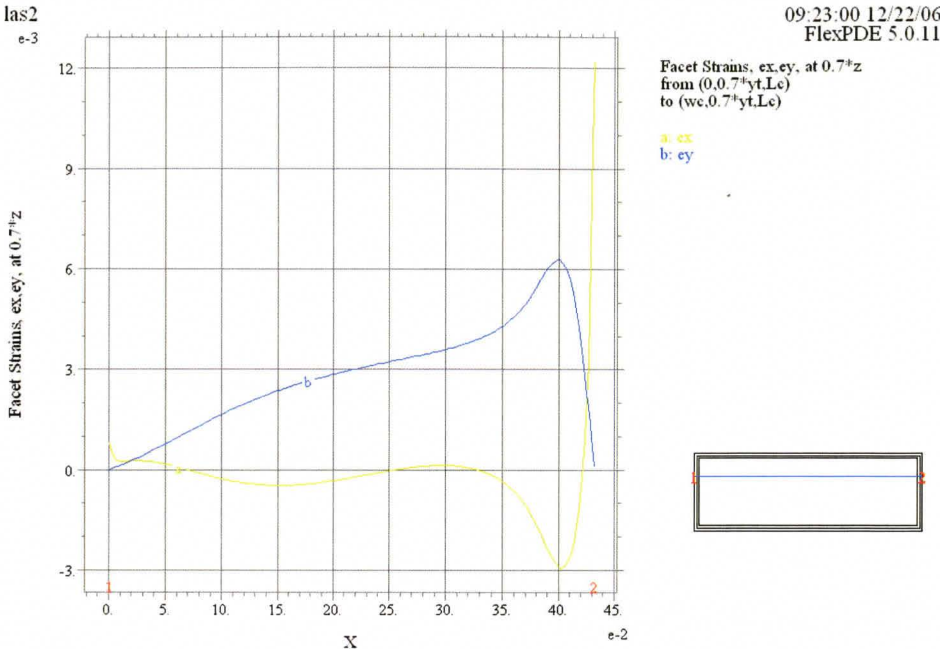

3100-2-O: Grid#1 p3 Nodes=54076 Cells=10704 RMS Err= 0.0085
Integral(a)= -1.137315e-4 Integral(b)= 1.227335e-3

(d)

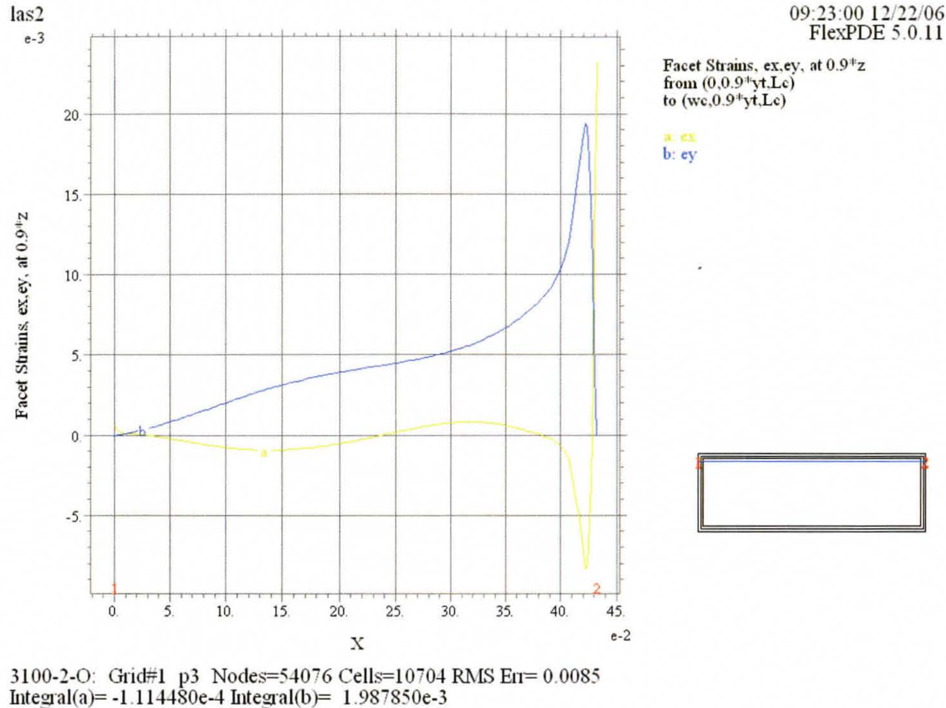

(e)

Figure 6.11. (a) - (e) This series of plots shows the strain profile along horizontal sections taken 0.1, 0.3, 0.5, 0.7, and 0.9 times the height, *yt*, of the device. As noted before, $ey \equiv \varepsilon_{zz}$.

This sample is consistently under tensile ε_{zz} strain. The magnitude of the strain increases as one moves to the top of the device. On the other hand, the ε_{xx} strain is consistently compressive, except near the bottom, where it is very nearly zero. It increases in magnitude as one approaches the top of the device.

These observations suggest that the metal on top is the primary origin for the strain patterns observed. The compressive ε_{xx} strain at the top is due to the metal. Consequently the material is distended in the *z*-direction, but compressed in the *x*-direction in accordance with the principles of linear elasticity theory. As

one moves down the device, the influence of the metal-induced compression is gradually dampened.

The figure below show the strain profile along a vertical section through the middle of the device.

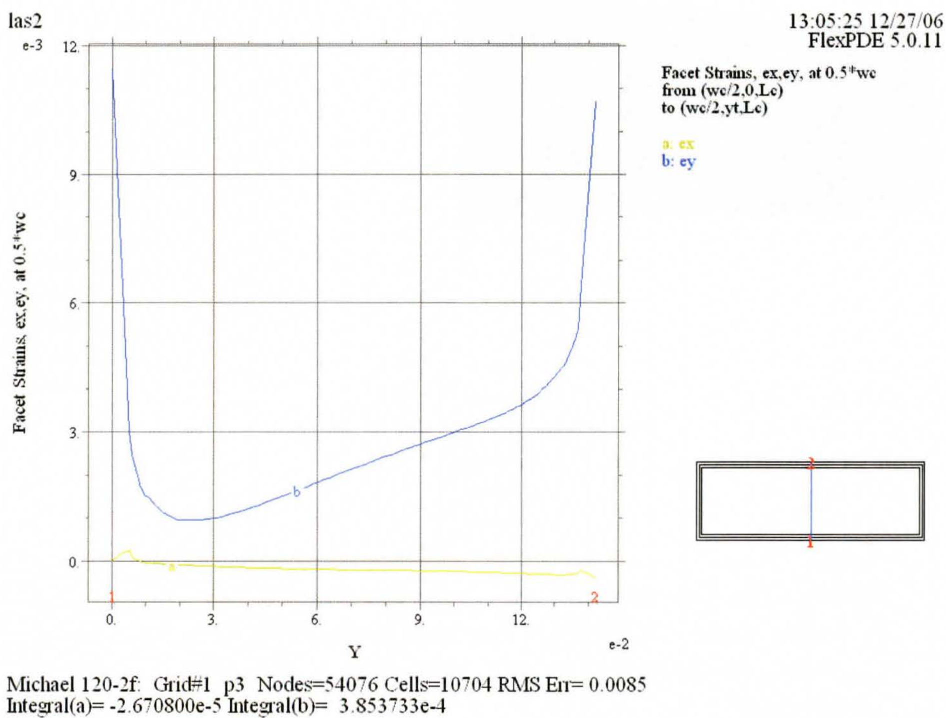

Figure 6.12. This figure shows the strain profile through a vertical section through the middle of the device. As before, $ey \equiv \varepsilon_{zz}$. The profile evalutated at 0.25 and 0.75 the width, *wc*, of the facet remained similar in shape.

The diagram below shows the distortion to the facet that causes these strains.

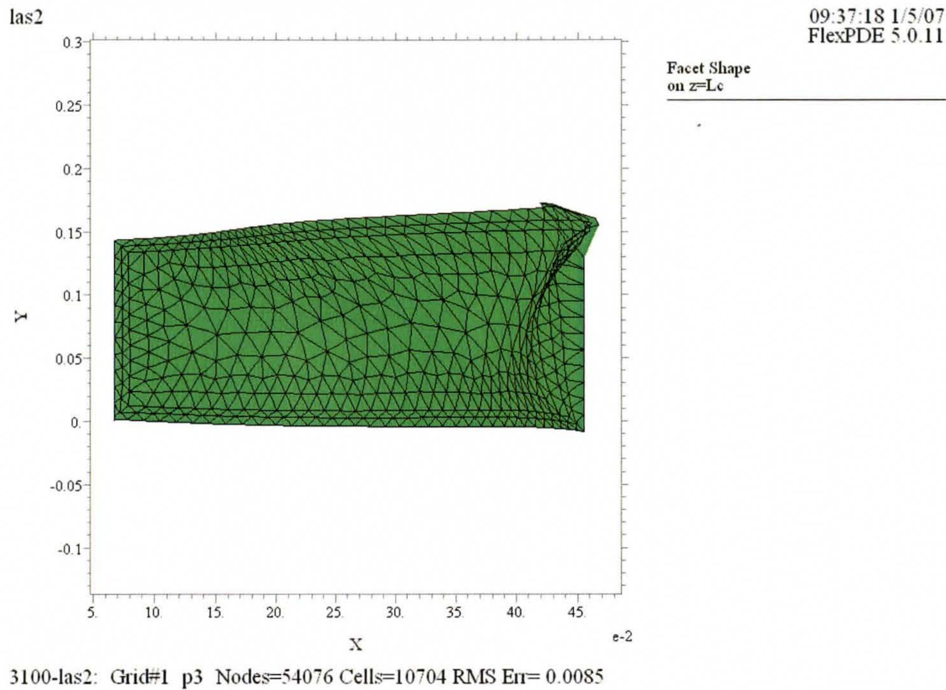

Figure 6.13. This diagram shows the distortion to the facet that causes the strains calculated in Figure 6.10. (a) – (e). As established before, the *y*-axis here is the *z*-axis in the discussion.

It is evident from the diagram above that the bottom regions of the facet are under relatively little strain, and there is consequently very little distortion here, except toward the edges, at the bottom right hand corner. It is also evident that this distortion is due to that at the top right-hand corner, whose influence propagates down the facet.

3100(b) las9

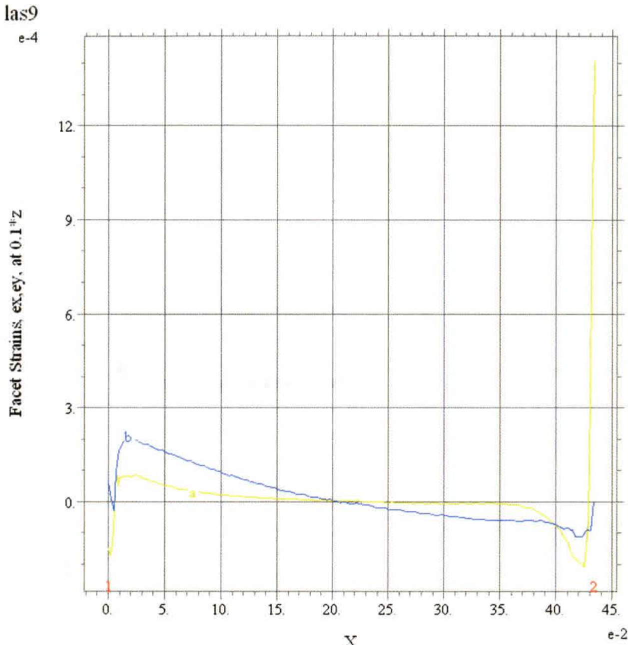

(a)

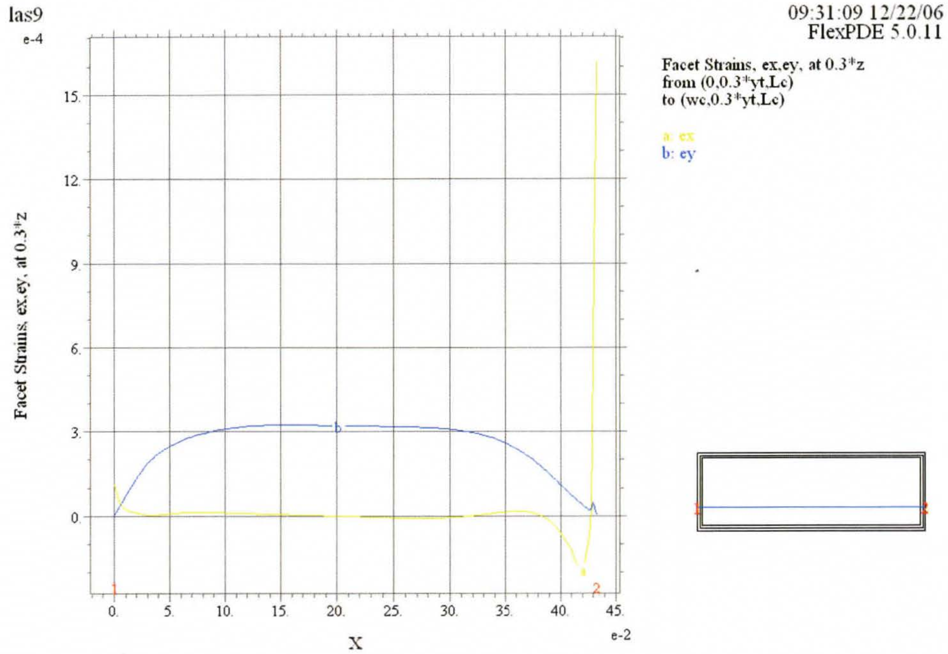

(b)

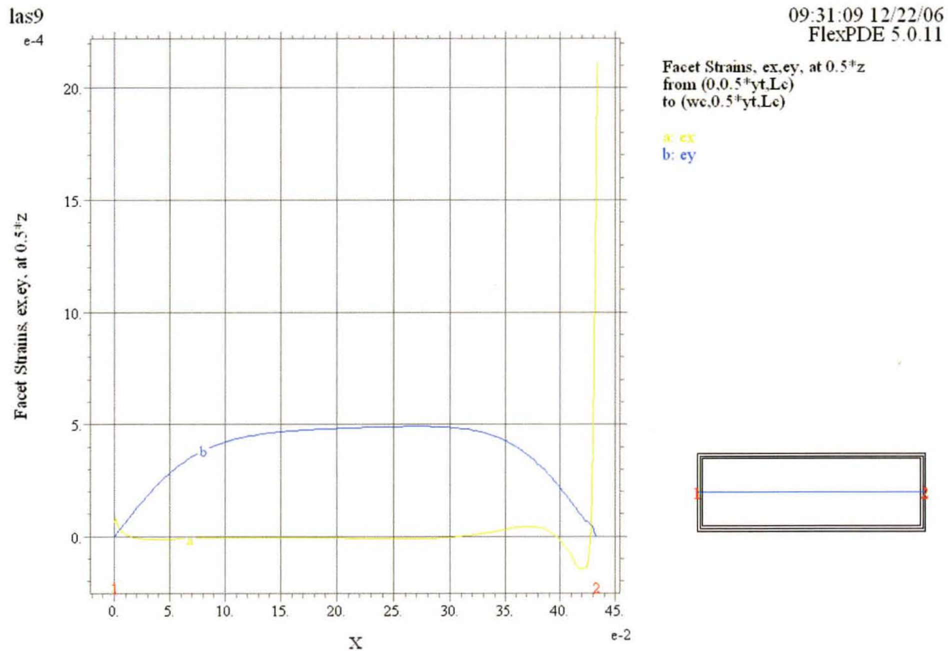

(c)

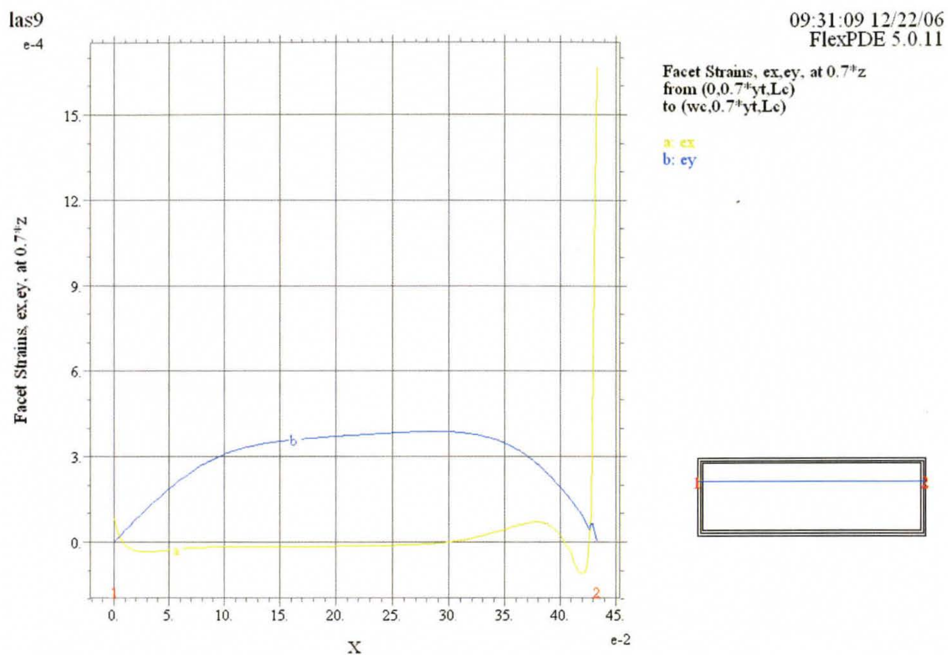

(d)

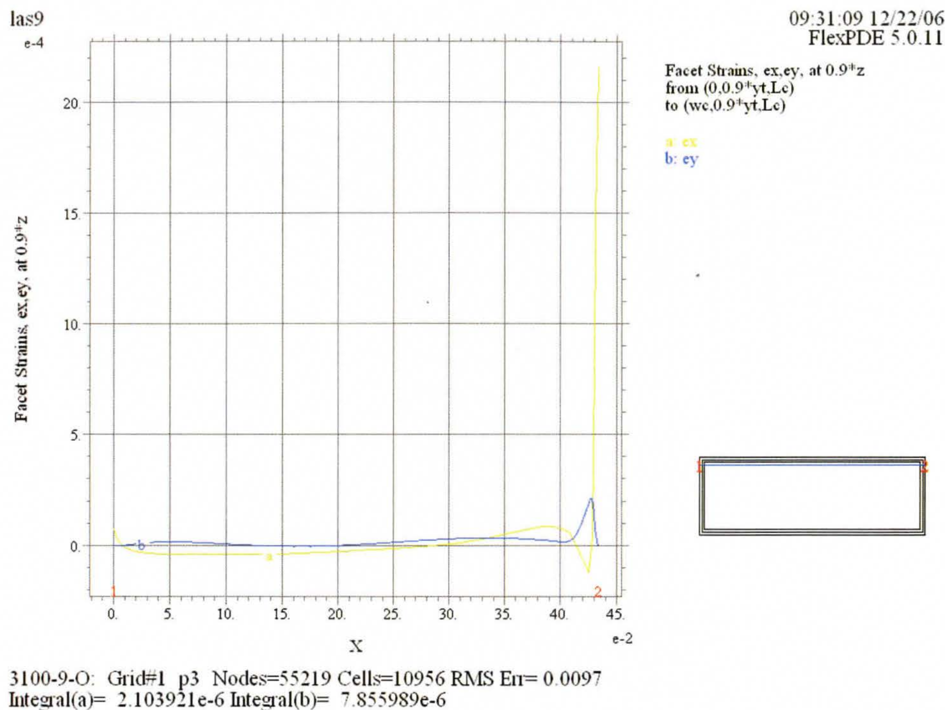

(e)

Figure 6.14. (a) - (e) This series of plots shows the strain profile along horizontal sections taken 0.1, 0.3, 0.5, 0.7, and 0.9 times the height, *yt*, of the device. As noted before, $ey \equiv \varepsilon_{zz}$.

The device is under tensile ε_{zz} strain for most of its length from top to bottom. The peak magnitude is in the middle, with very little near the bottom, a little distance away from the edges; the strain becomes compressive just beneath the top edge. As such, there is a region of zero ε_{zz} strain near the top of the device. The sample is under very little ε_{xx} strain near the bottom, but there is a gradual increase in magnitude (though not by much) as one moves to the top of the device. The ε_{xx} strain is consistently compressive.

Neither the carrier nor the metal contact can account for the high tensile ε_{zz} strain in the middle of the facet. It is possible that the material is curved in the plane of the facet.

The figure below illustrates the strain profile along a vertical section taken through the middle of the facet.

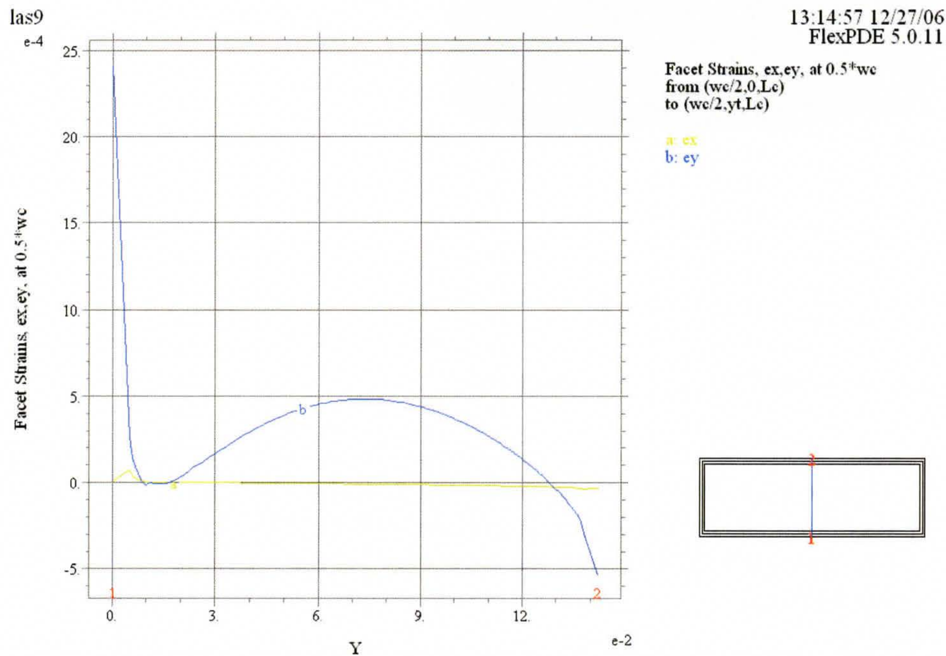

Figure 6.15. This figure shows the strain profile through a vertical section through the middle of the device. As before, $ey \equiv \varepsilon_{zz}$.
The profile evalutated at 0.25 and 0.75 the width, *wc*, of the facet remained similar in shape.

The diagram below shows the distortion to the facet that causes these strains.

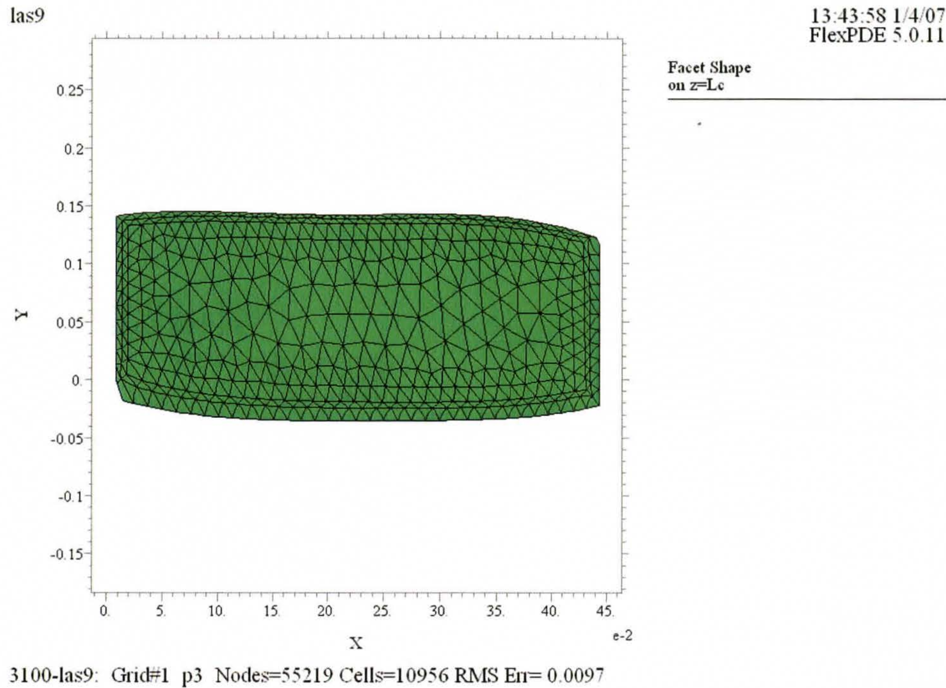

Figure 6.16. This diagram shows the distortion to the facet that causes the strains calculated in Figure 6.13. (a) – (e). As established before, the *y*-axis here is the *z*-axis in the discussion.

The figure above indicates that there is some asymmetry about a vertical line through the middle of the facet, primarily at the top. The slight bending at the bottom is consistent with a bending motion brought about by the underlying carrier. However, if the device were 'pinned' to the carrier by a uniform solder while the carrier contracted on cooling to ambient temperature, one would expect the convex distortion of the top of the facet, as is seen in the diagram, though not

necessarily the downward buckling seen at the bottom of the device. Presumably, therefore, the device-solder bond is not uniform. This would account for the fact that the facet bends upwards more at the bottom left-hand side than the at the bottom right-hand side. It would also mean that any downward bending at the top would be more pronounced where the upward curvature at the bottom is less: that is, more downward curvature at the top right-hand side and less at the top left-hand side. This is indeed observed in figure 6.15. above.

2400 hours (a) las9

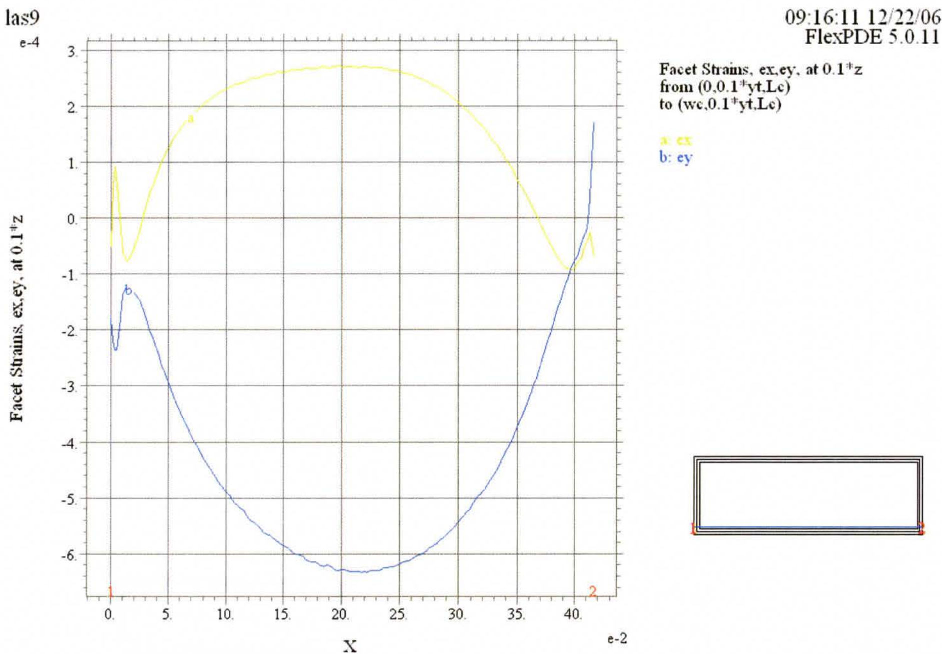

(a)

09:16:11 12/22/06
FlexPDE 5.0.11

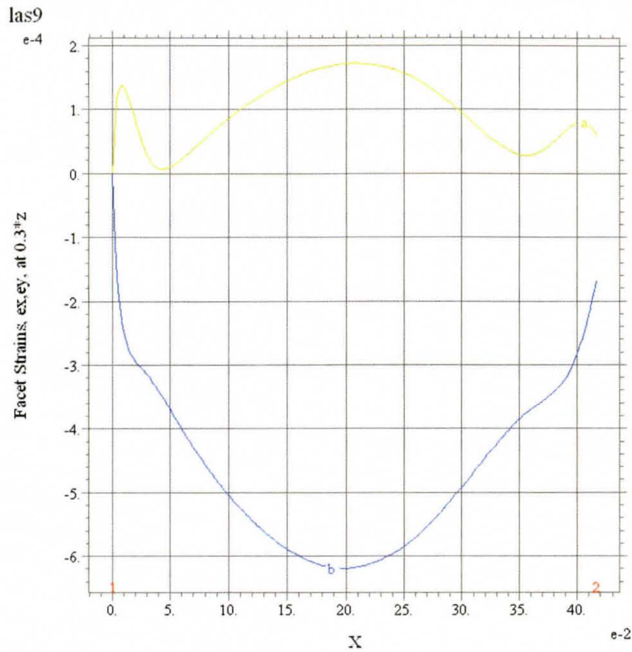

Facet Strains, ex,ey, at 0.3*z
from (0,0.3*yt,Lc)
to (wc,0.3*yt,Lc)

a: ex
b: ey

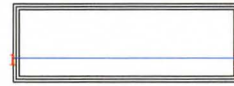

2400-9-O: Grid#1 p3 Nodes=52459 Cells=10374 RMS Err= 0.0015
Integral(a)= 4.057692e-5 Integral(b)= -1.944104e-4

(b)

09:16:11 12/22/06
FlexPDE 5.0.11

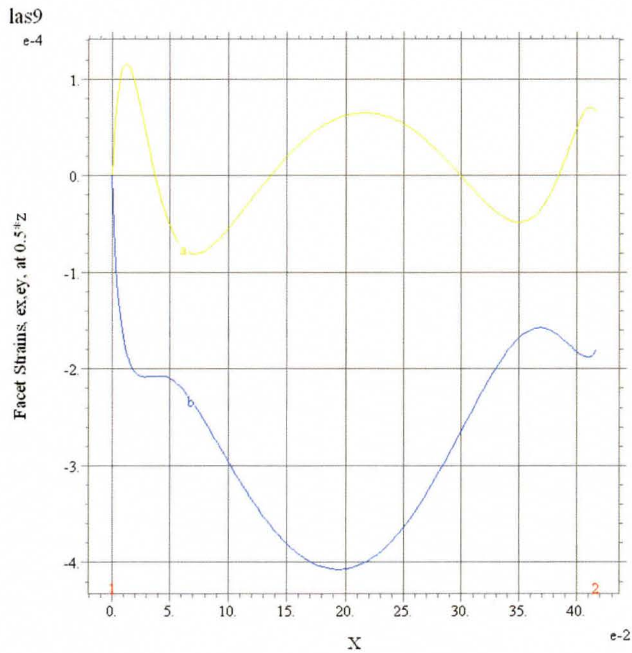

Facet Strains, ex,ey, at 0.5*z
from (0,0.5*yt,Lc)
to (wc,0.5*yt,Lc)

a: ex
b: ey

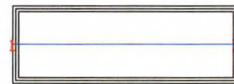

2400-9-O: Grid#1 p3 Nodes=52459 Cells=10374 RMS Err= 0.0015
Integral(a)= 3.457670e-6 Integral(b)= -1.157224e-4

(c)

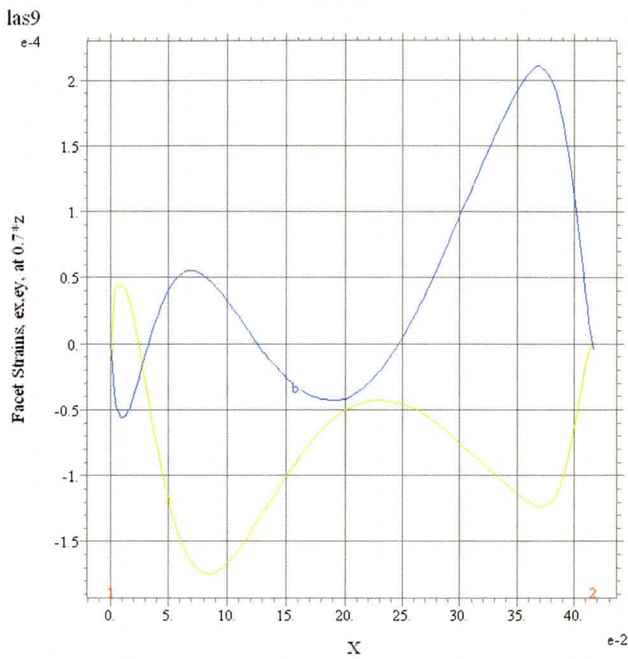

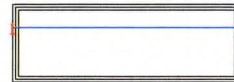

(d)

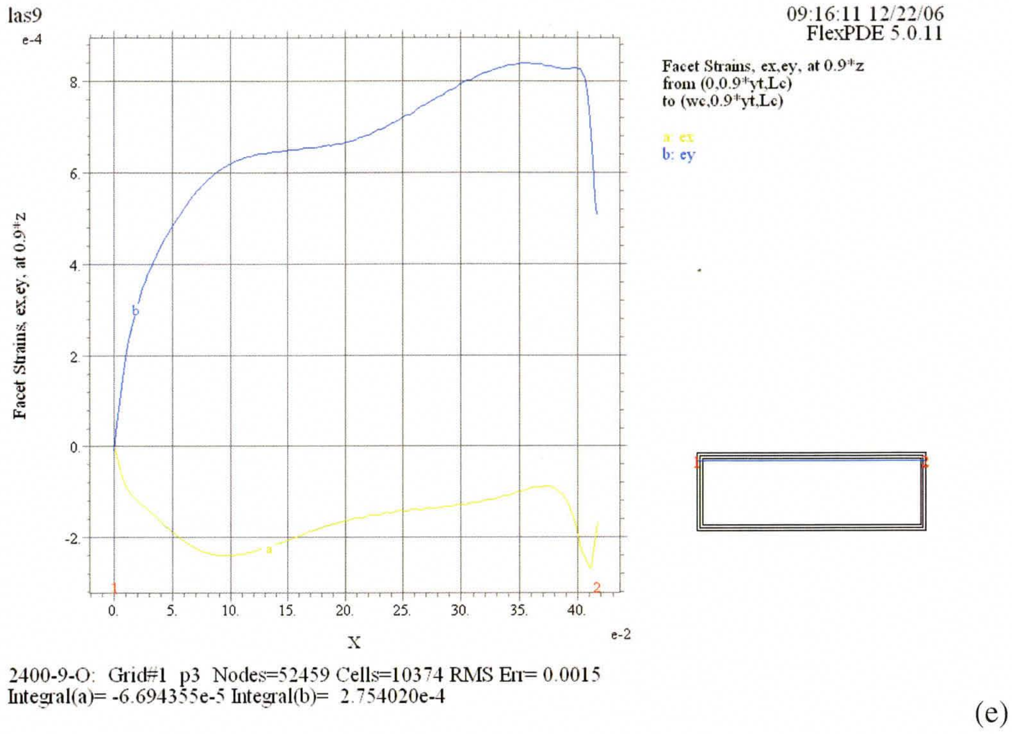

(e)

Figure 6.17. (a) – (e) This series of plots shows the strain profile along horizontal sections taken 0.1, 0.3, 0.5, 0.7, and 0.9 times the height, *yt*, of the device. As noted before, $ey \equiv \varepsilon_{zz}$.

The bottom region of the material is under compressive ε_{zz} strain. This is true for most of the device as one moves up. The magnitude of the strain decreases monotonically until the top regions, where the material is under significant tensile ε_{zz} strain. As such, there is a region, about a third of the way up, under no ε_{zz} strain whatsoever.

The trend for the ε_{xx} strain is exactly opposite. There is an almost linear decrease in the magnitude of the strain as one moves up the device. The ε_{xx} strain changes from tensile to compressive.

The figure below shows the strain profile along a vertical section through the middle of the facet.

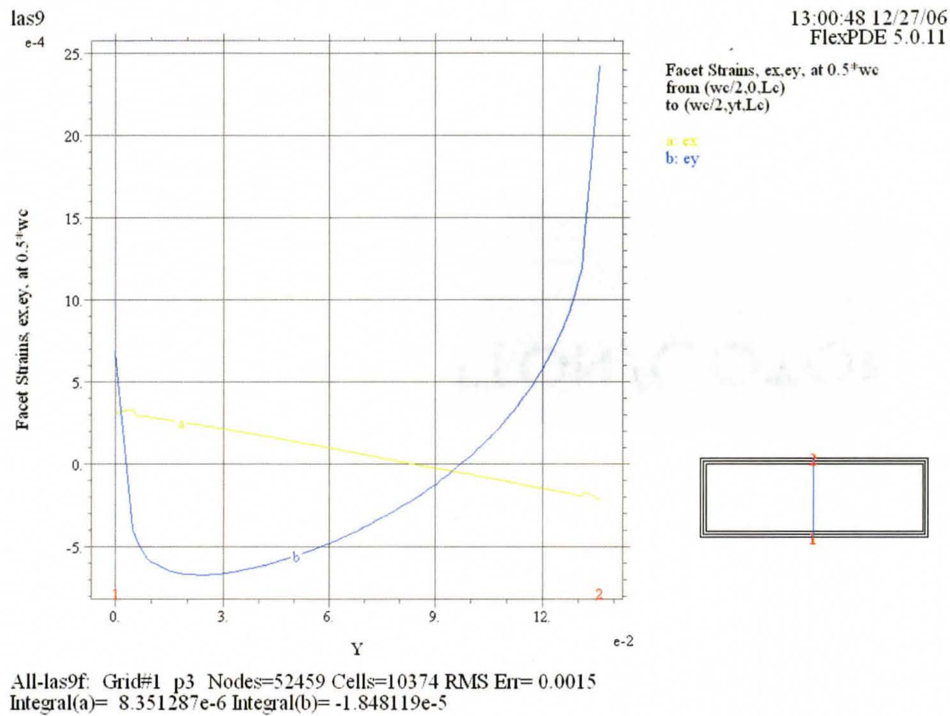

Figure 6.18. This figure shows the strain profile along a vertical section through the middle of the device. As before, $ey \equiv \varepsilon_{zz}$.
The profile evalutated at 0.25 and 0.75 the width, *wc*, of the facet remained similar in shape.

The diagram below shows the deformation of the facet that causes these strains.

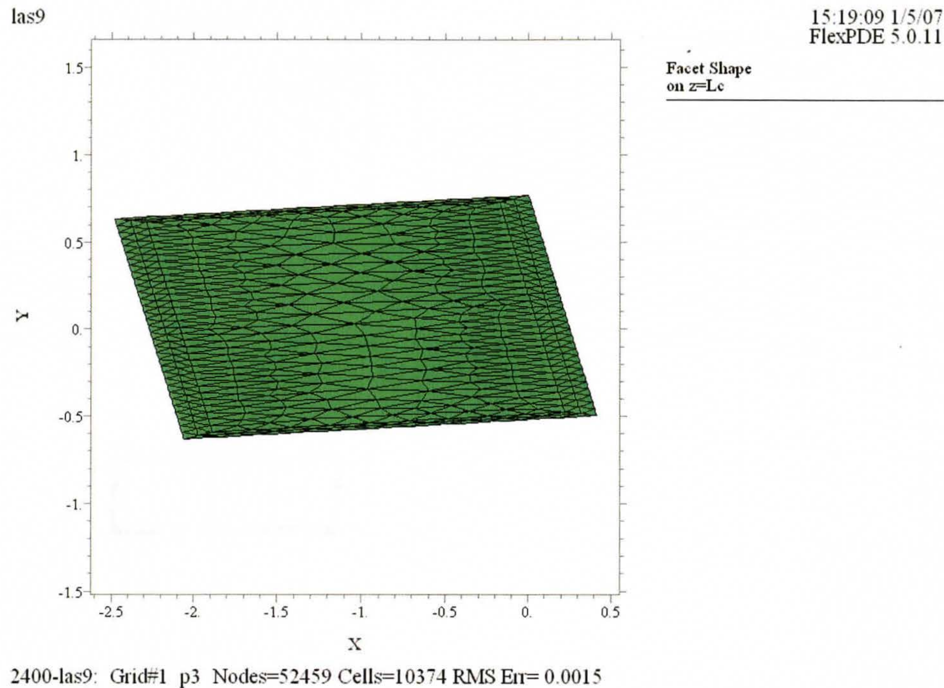

Figure 6.19. This diagram shows the distortion to the facet that causes the strains calculated in Figure 6.16. (a) – (e). As established before, the *y*-axis here is the *z*-axis in the discussion.

From figure 6.18. above, it is clear that this device shows very little bending in the *x*-*z* plane. However, the device does show pure shear. This accounts for the compression along the *z*-direction that is present along much of the height of the facet, and the concomitant tensile strain along the *x*-direction, also present for a similar length.

2400 hours (a) las7

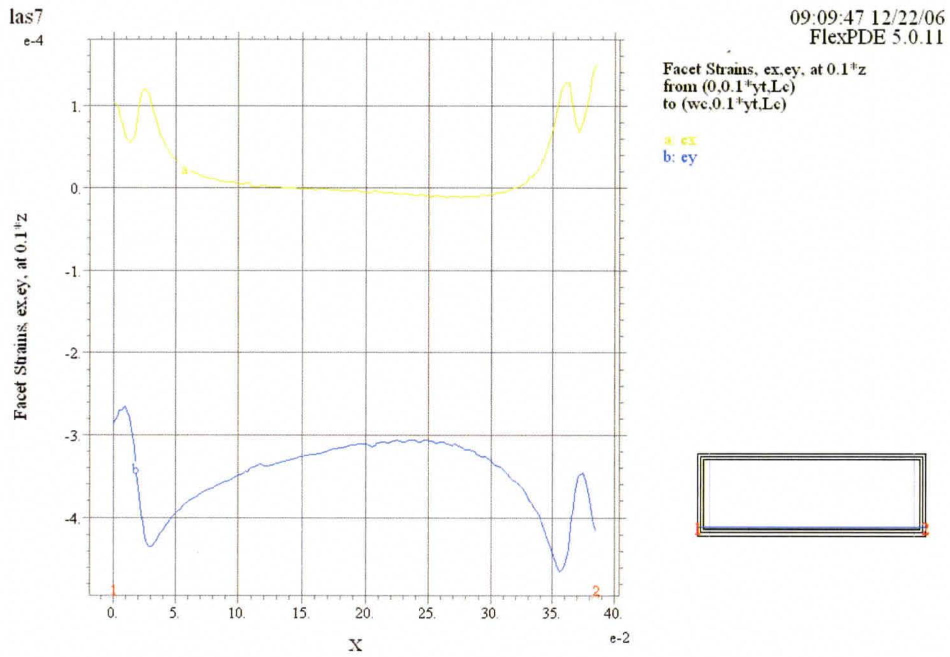

(a)

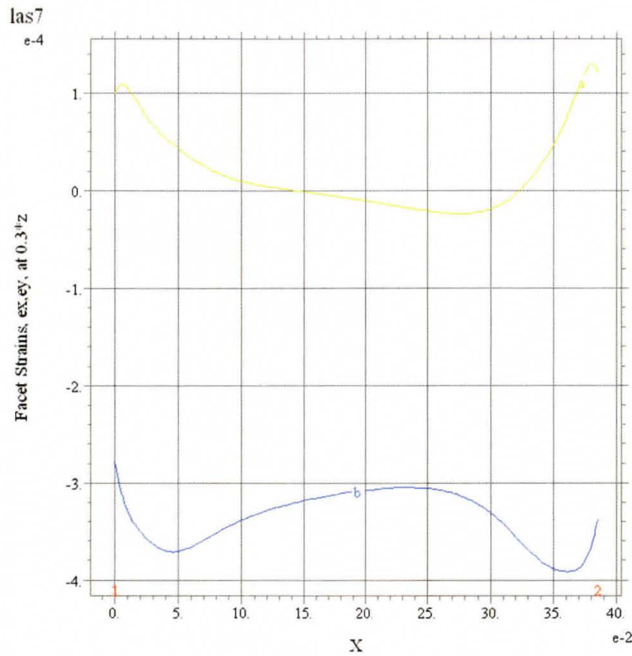

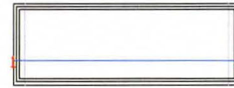

(b)

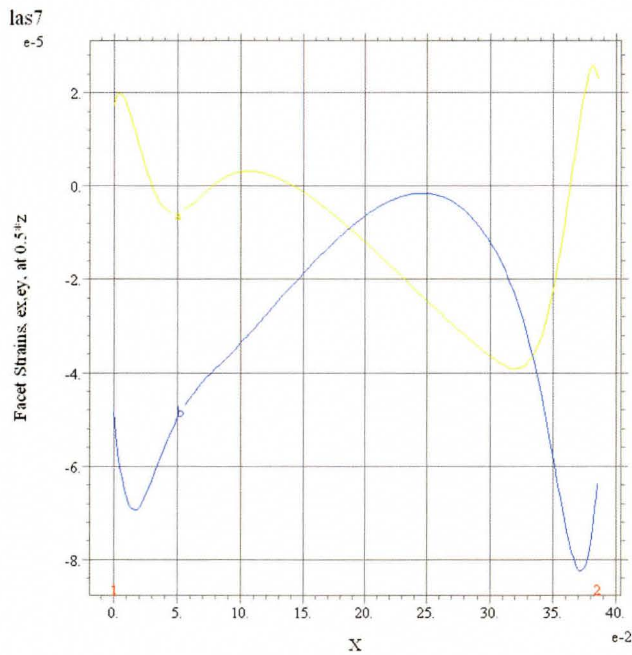

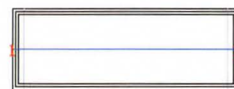

(c)

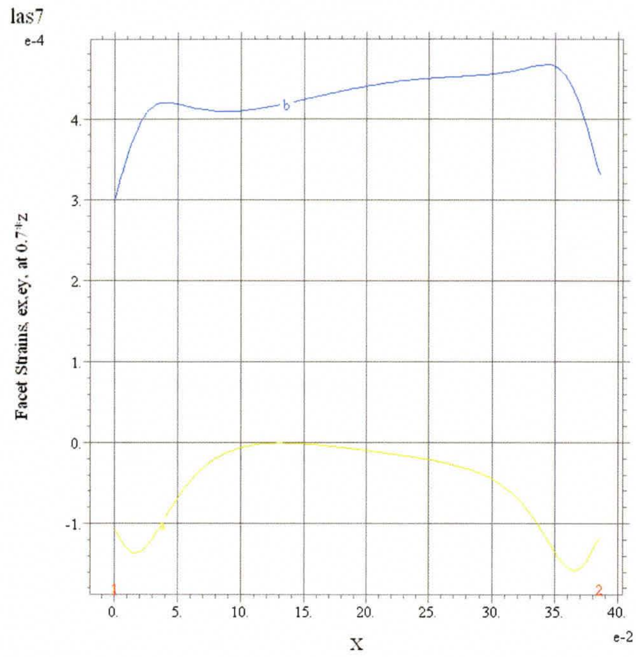

09:09:47 12/22/06
FlexPDE 5.0.11

Facet Strains, ex,ey, at 0.7*z
from (0,0.7*yt,Lc)
to (wc,0.7*yt,Lc)

a: ex
b: ey

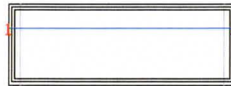

(d)

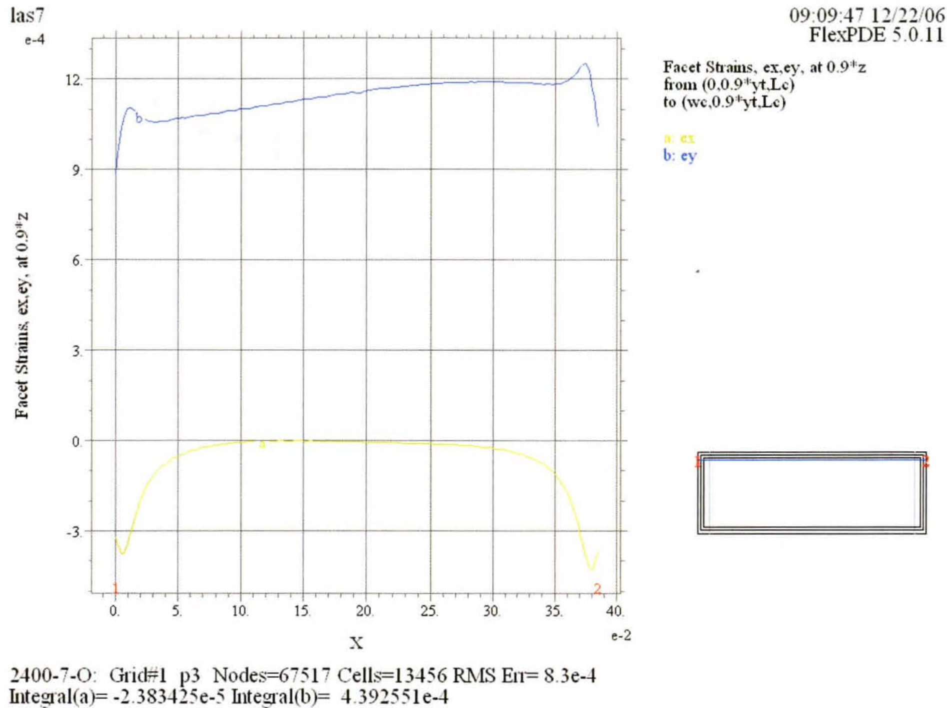

(e)

Figure 6.20. (a) – (e). This series of plots shows the strain profile along horizontal sections taken 0.1, 0.3, 0.5, 0.7, and 0.9 times the height, *yt*, of the device. As noted before, $ey \equiv \varepsilon_{zz}$.

The ε_{xx} strain remains very nearly zero as one moves up the device, although it does achieve a peak compressive value near the middle of the facet. The highest magnitude it achieves occurs near the middle of the facet. However, the magnitude of the ε_{zz} strain increases monotonically, moving from compressive to tensile as one moves up the facet. The region near the centre of the facet has zero ε_{zz} strain.

It is likely that the compressive ε_{zz} strain observed near the bottom of the facet is due to an upward curvature induced by the carrier underneath. However, it is not clear why that should not result in a tensile ε_{xx} strain. From the stiffness coefficients of InP, one might expect that the ε_{zz} strain be about twice the ε_{xx} strain. However, this does not account for the difference observed in this simulation.

The figure below illustrates the strain profile along a vertical section taken through the middle of the device.

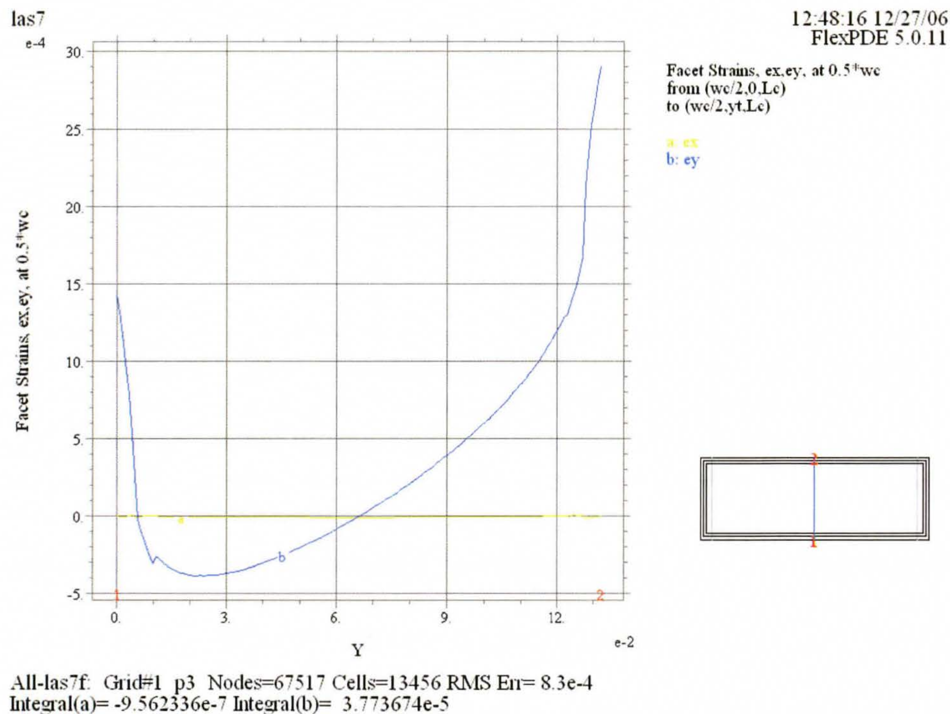

Figure 6.21. This figure shows the strain profile through a vertical section through the middle of the device. As before, $ey \equiv \varepsilon_{zz}$. The profile evalutated at 0.25 and 0.75 the width, *wc*, of the facet remained similar in shape.

The diagram below shows the distortion to the facet that causes these strains.

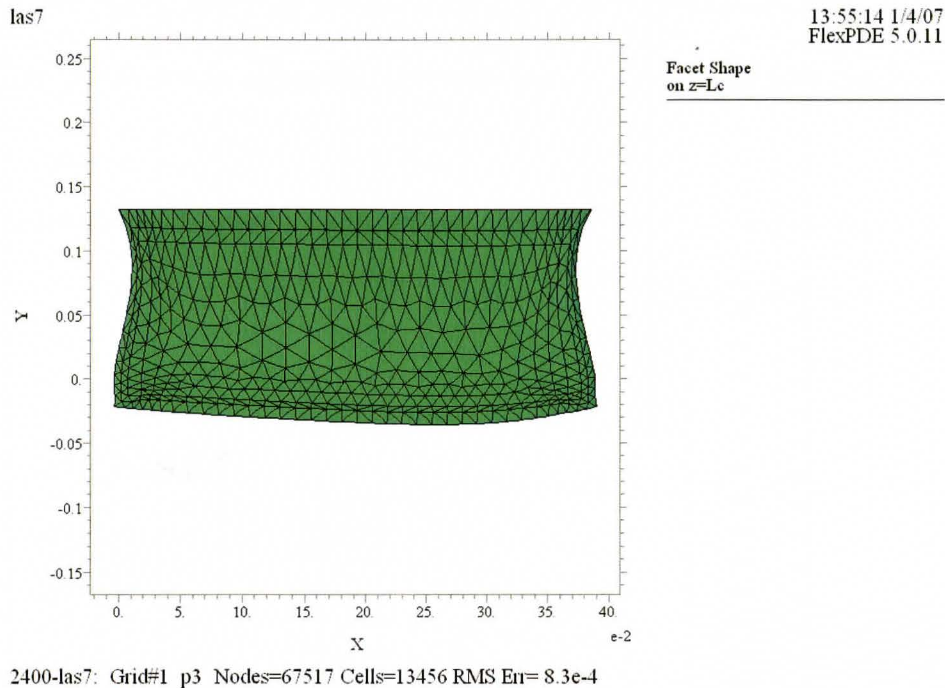

Figure 6.22. This diagram shows the distortion to the facet that causes the strains calculated in Figure 6.19. (a) – (e). As established before, the *y*-axis here is the *z*-axis in the discussion.

A bottleneck effect is quite apparent in figure 6.21. above. It dominates the regions near but not at the top of the device. At the top of the device, there is very little distortion in the *x*-direction. The tensile strain along the *z*-direction, however, is evident here.

There is also a slight bending at the bottom of the facet. From the relatively undistorted shape of the top of the facet, it seems apparent the chip

expands or contracts against the metal contact on top. A lateral expansion of the carrier would cause an upward bending motion near the bottom. This would induce a compressive strain in the z-direction, as observed. However, given the intractable contact at the top, the semiconductor material there would be pinched narrow. This would have two effects: it would cause a tensile strain in the z-direction near the top of the device; and it would induce vertical planes near the central regions of the facet to come together, causing a compressive strain in the x-direction.

Perhaps the reason why one does not observe much of a tensile ε_{xx} strain at the bottom due to the compressive ε_{zz} strain is because of this pinching effect: the curvature at the bottom causes too small a tensile z-direction strain; as such, the pinching of the vertical planes above would be sufficient to overcome the natural tendency to distend in the x-direction near the bottom.

6.4.2. Summary

The tensile strains of six devices, as determined by FEM fits to their DOP data have been analysed in an attempt to explain the nature of the strain patterns on them.

The qualitative behaviour of the strain near the bottom and top of the respective devices can generally be explained by reference to the physics of the situation.

5000 hours (a) las2 exhibits an overall bending motion consistent with a lateral expansion of the underlying carrier.

5000 hours (b) las6 shows a slight curvature at the bottom and general compressive strain in the x-direction. The top of the device indicates features consistent with a non-uniform metallisation.

3100 hours (a) las2 shows little to no strain at the bottom. The primary cause of distortion in the facet is posited to be the top, where the strain at the top right-hand corner propagates down the facet.

3100 hours (b) las9 indicates features implying a non-uniform solder. Asymmetry is mirrored at the top and bottom, with more curvature at the bottom left-hand side implying less at the top right-hand side and vice versa.

2400 hours (a) las9 indicates pure shear, causing the device to be compressed along the z-direction and distended along the x-direction for much of the height of the facet.

2400 hours (b) las7 exhibits a pinching effect due to an unyielding metal contact on top. The semiconductor underneath expands and contract against this rigid metal, inducing a higher-than-expected ε_{xx} strain near the middle of the device.

6.4.3. Discussion: Shear Strain Plots Extracted from ROP Fits

The asymmetry mentioned in Chapter 4 is apparent in all the ROP strain plots.

5000 hours (a) las2

The figure below shows the shear strain, ε_{xz}, plots extracted from the FEM fit to the ROP data near the bottom and top of the device.

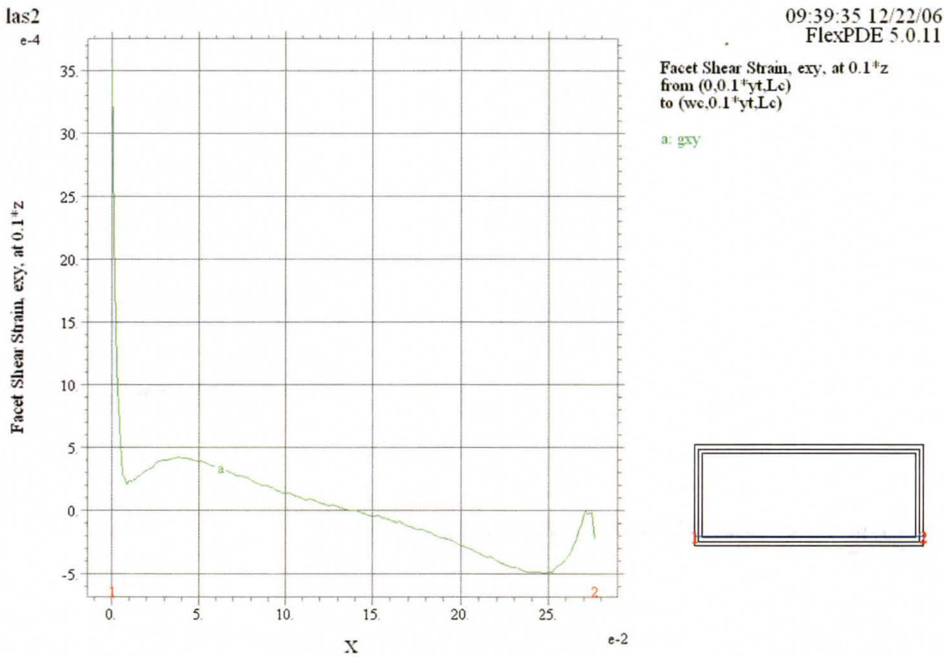

(a)

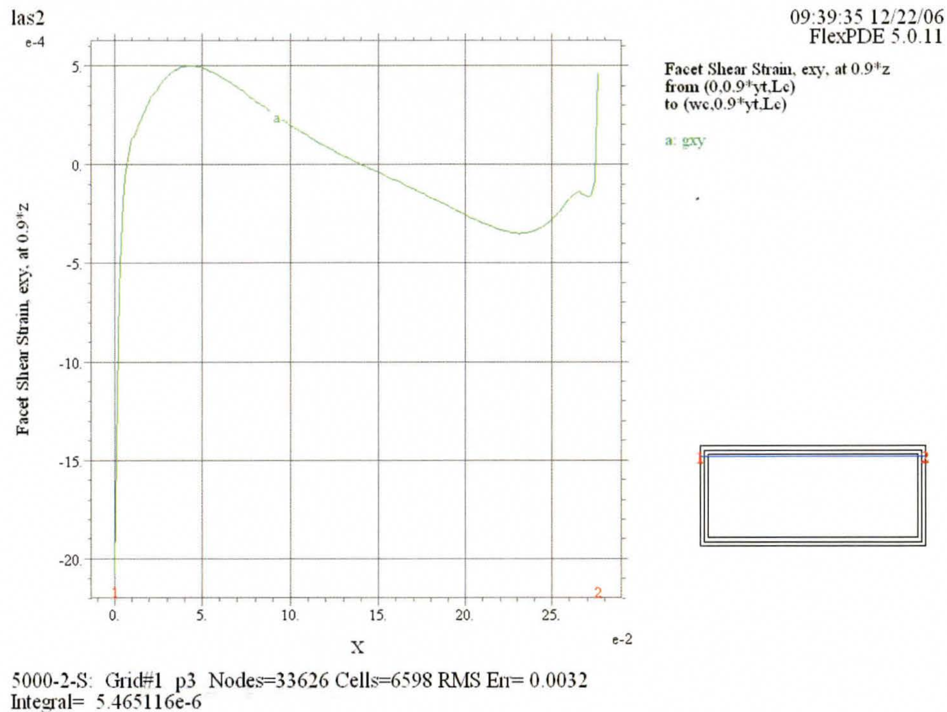

Figure 6.23. (a)-(b) This figure shows the shear strain profile evaluated at 0.1 and 0.9 times the height, yt, of the facet.
As noted before, $gxy \equiv \varepsilon_{xz}$.

The asymmetry is about the central line bisecting the facet vertically. Though the shape of the strain profile changes slightly as one moves up the device, this asymmetry is preserved. Additionally, the basis functions used to generate the fit lack torsion terms in both the bottom and top tensile strains. These observations suggest that the primary source of shear strain is the bending of the InP due to the carrier or metal contact, or both. This is consistent with what has already been deduced above.

5000 hours (b) las6

The figures below show the shear strains extracted from the FEM fit near the bottom and top of the facet.

Though indicating an asymmetry like 5000 hour (a)'s, the simulation shows it to be opposite in sense and also not quite centred about the vertical bisecting line. Additionally, the form of the strain plot is not preserved as one moves up the device from bottom to the top. Furthermore, the basis functions indicate the presence of torsion terms both at the top and bottom tensile strains of the device.

Therefore, in addition to the bending of the material due to the carrier and metal contact, there is a twisting moment possibly due to both the metal and the carrier. Looking at the respective magnitudes of the shear strains for the top and bottom, it is clear that the bending is more severe near the top than near the bottom.

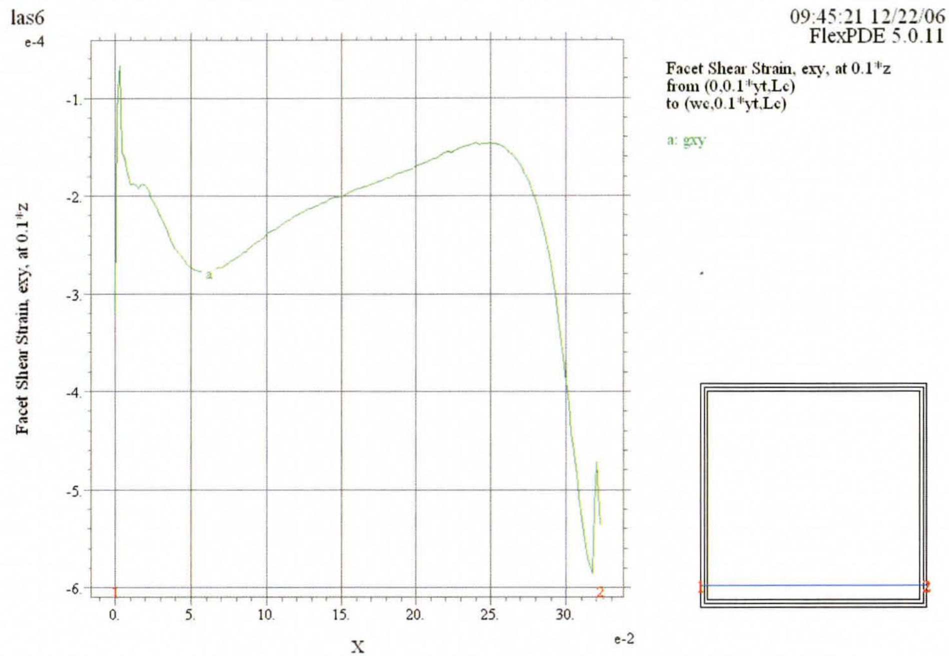

(a)

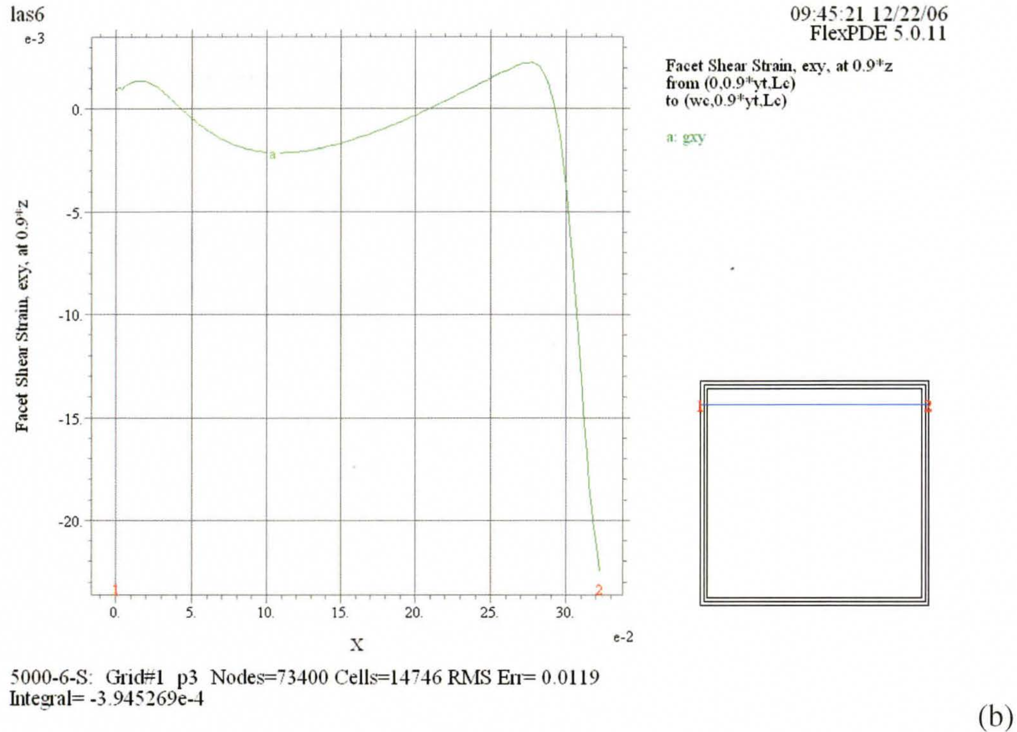

(b)

Figure 6.24. (a)-(b) This figure shows the shear strain profile evaluated at 0.1 and 0.9 times the height, yt, of the facet. As noted before, $gxy \equiv \varepsilon_{xz}$.

These findings are consistent with what can be seen in figure 6.9. There is a large distortion due to non-uniform deposition of metal on top. Presumably, this distortion leads to the torsion terms observed here. The slight bending at the bottom of the facet would account for the asymmetry observed here. Since the distortion at the top is very much localised, it is understandable that the form of the shear strain plot is not preserved moving up the device.

<u>3100 (a) las2</u>

The figures below show the shear strains extracted from the FEM fit near the bottom and top of the facet.

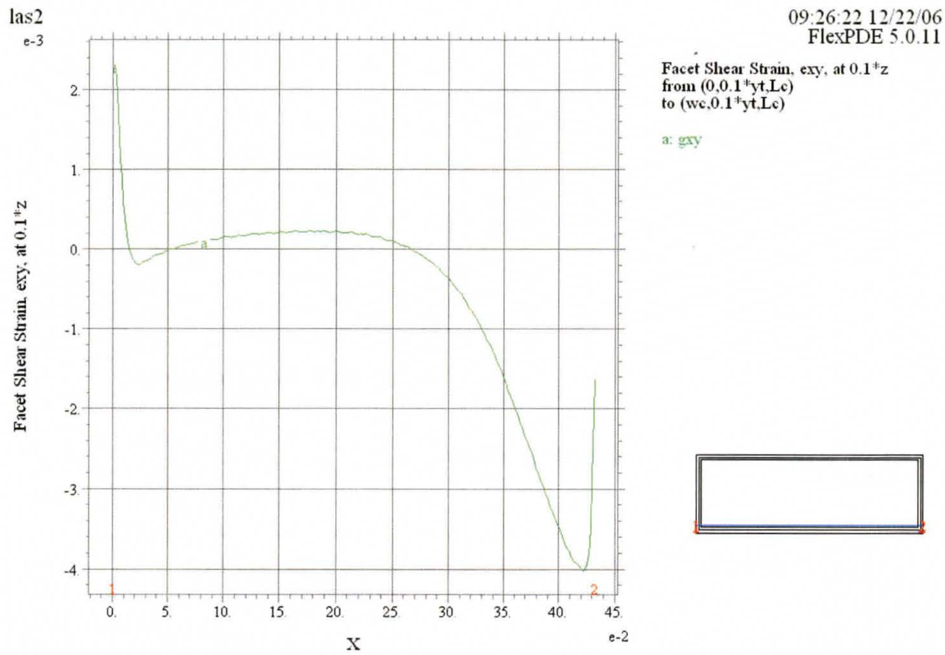

(a)

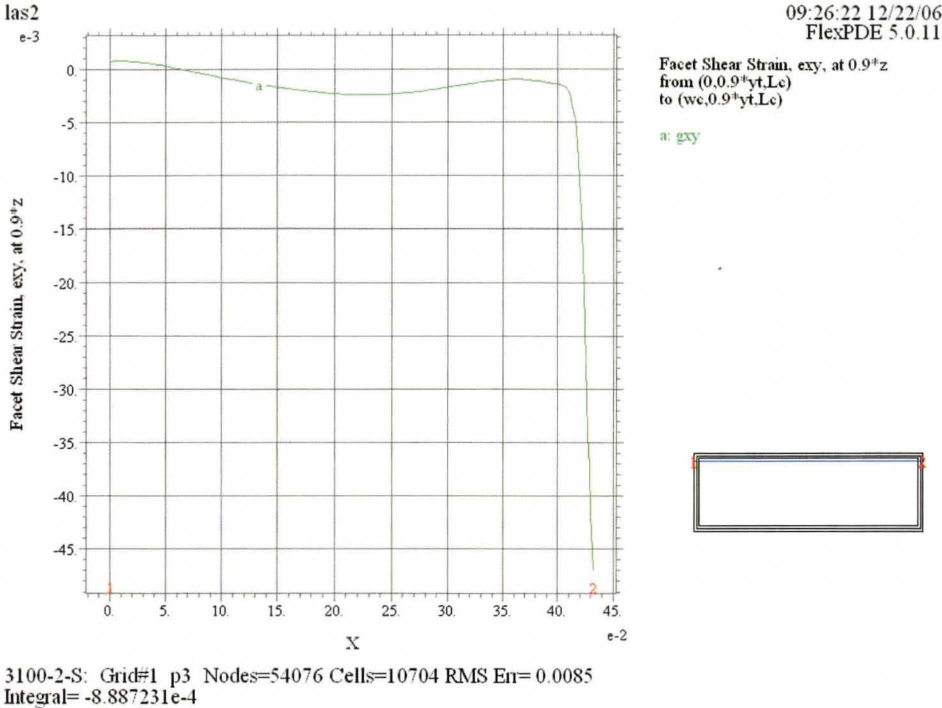

(b)

Figure 6.25. This figure shows the shear strain profile evaluated at 0.1 and 0.9 times the height, yt, of the facet.
As noted before, $gxy \equiv \varepsilon_{xz}$.

Shear strain asymmetry is not apparent in these plots. Presumably, therefore, the metal-induced compression at the top does not cause an appreciable bending of the underlying semiconductor. This is consistent with Figure 6.12., where one can see little to no bending at the bottom and a very localised distortion at the top, with no bending. Furthermore, there is a torsion component to the basis functions used to fit to the data. Both the metal contact and the carrier contribute to this aspect of the tensile strain.

A further analysis of the basis functions used to fit to the data reveals a strong *y*-dependence on one of the tensile strains imposed on the perimeter of the facet, up to and including the fourth order (where the *y*-direction is perpendicular to the plane of the facet). This is observed in the vertical strain imposed at the bottom of the device. Additionally, one observes curvature along the length of the device at both the top and bottom to a high order in *y*. Presumably, the solder is not uniformly deposited across the bottom plane of the die; this particular inhomogeneity would lead to a strain contribution from the solder in the more interior regions, or at least close to the emitting surface, of the device along the *y*-direction. The metal contact should also contribute to this.

<u>3100 (b) las9</u>

The figures below show the shear strains extracted from the FEM fit near the bottom and top of the facet.

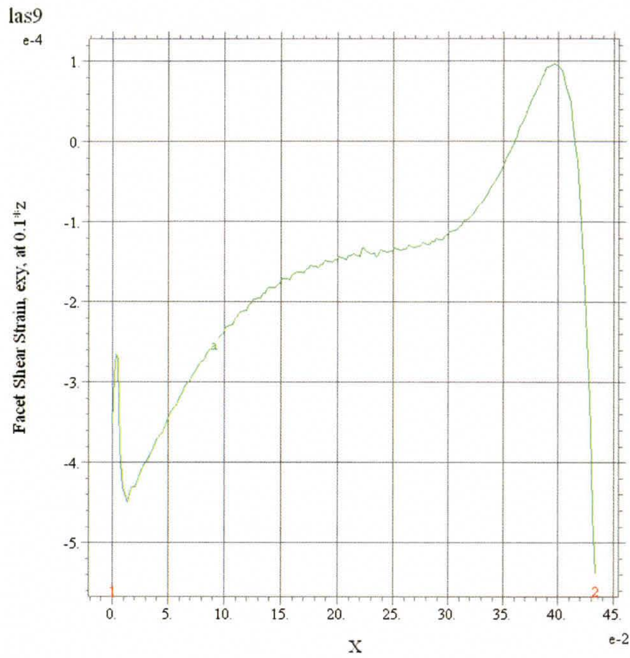

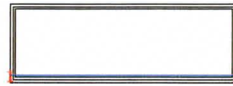

(a)

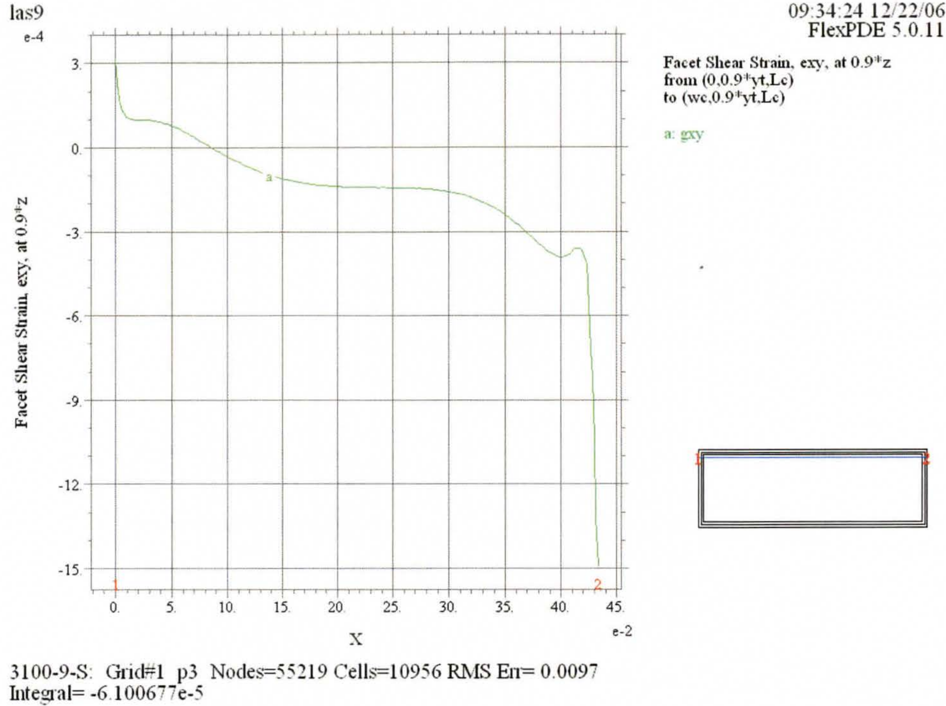

(b)

Figure 6.26.(a)-(b) This figure shows the shear strain profile evaluated at 0.1 and 0.9 times the height, yt, of the facet.
As noted before, $gxy \equiv \varepsilon_{xz}$.

What little asymmetry there is is confined to the bottom right-hand corner and the top left-hand corner. The former fact may be explained by the observation that the solder does not extend the whole way across the bottom of the die, leaving a strip of semiconductor overhang to one side. These findings are consistent with the argument of a non-uniform solder that was posited in 6.4.1. above. Both the top and the bottom of the device, however, include torsion terms in the basis functions used to fit to the ROP and DOP data here; it is therefore

likely that the areas of the die attached to the solder contribute torsion terms to the local asymmetry observed.

An interesting point emerges when one examines the basis functions for the strains imposed at the bottom of the device. Both strains show high order (up to third) dependence on the *y*-coordinate. This is true not only of strains expected to have explicit *y*-dependence. For instance, a vertical strain imposed in the bottom left hand corner shows strong *y*-dependence. This implies a non-uniform solder bond in the *y*-direction, and may explain the highly tensile ε_{zz} strain in the middle of the facet, since not all stresses are due to forces in the *x*-*z* plane.

2400 (a) las9

The figures below show the shear strains extracted from the FEM fit near the bottom and top of the facet.

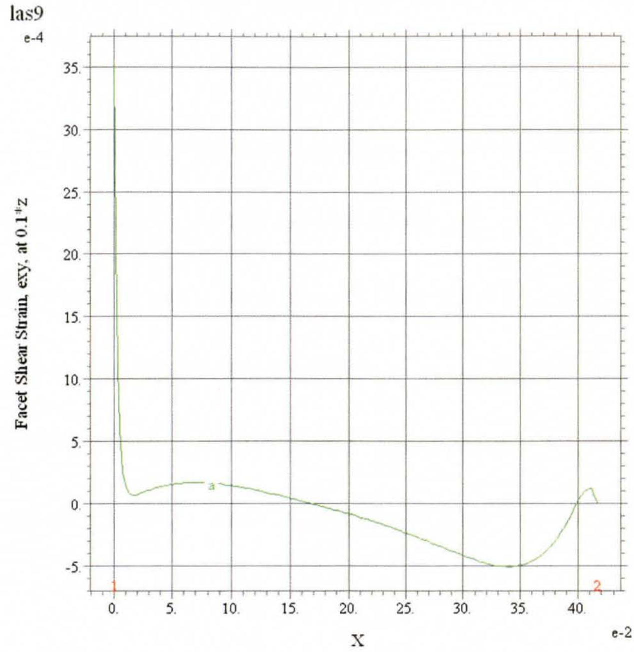

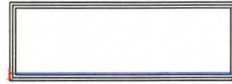

(a)

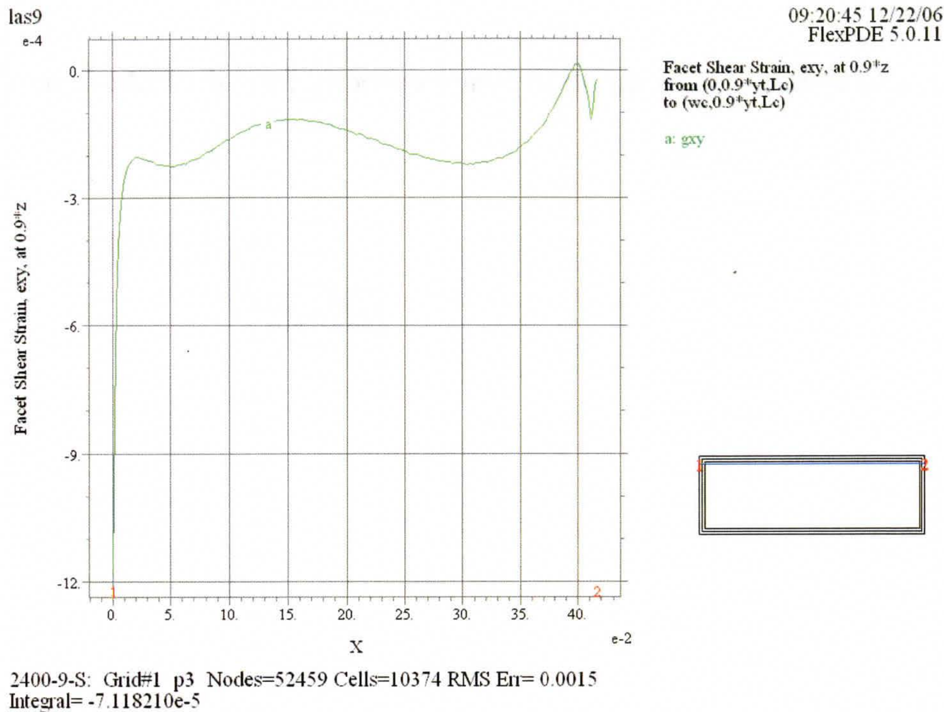

(b)

Figure 6.27.(a)-(b) This figure shows the shear strain profile evaluated at 0.1 and 0.9 times the height, yt, of the facet.
As noted before, $gxy \equiv \varepsilon_{xz}$.

While the asymmetry in shear strain is present near the bottom of the device, it is absent near the top. Presumably, there is some small bending at the bottom of the device not evident in figure 6.18.

Additionally, the basis functions do not reveal a significant *y*-dependence for the strains imposed on the facet. Interestingly, there is not a *y*-dependent force at the top. This implies that the metal is uniformly deposited at least a short distance away from the facet. There are, however, torsion terms both at the top and bottom of the device.

2400 (b) las7

The figures below show the shear strains extracted from the FEM fit near the bottom and top of the facet.

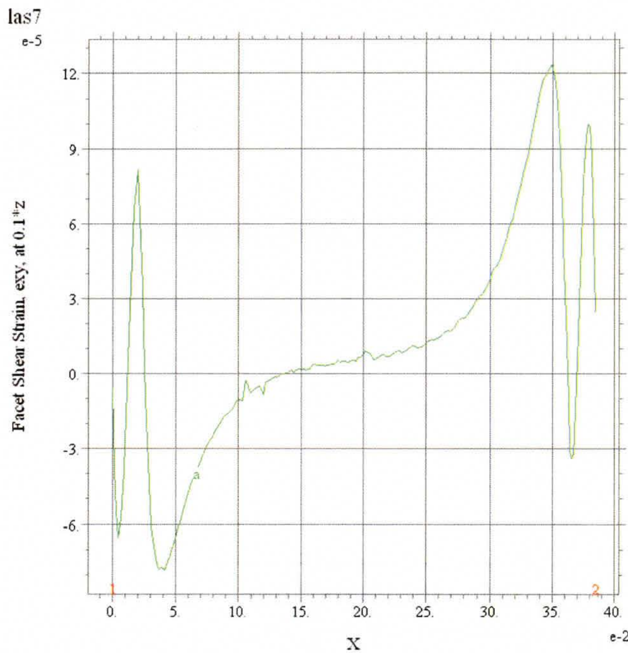

09:12:55 12/22/06
FlexPDE 5.0.11

Facet Shear Strain, exy, at 0.1*z
from (0,0.1*yt,Lc)
to (wc,0.1*yt,Lc)

a: gxy

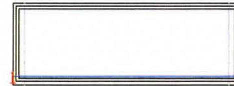

2400-7-S: Grid#1 p3 Nodes=67517 Cells=13456 RMS Err= 8.3e-4
Integral= 4.307700e-6

(a)

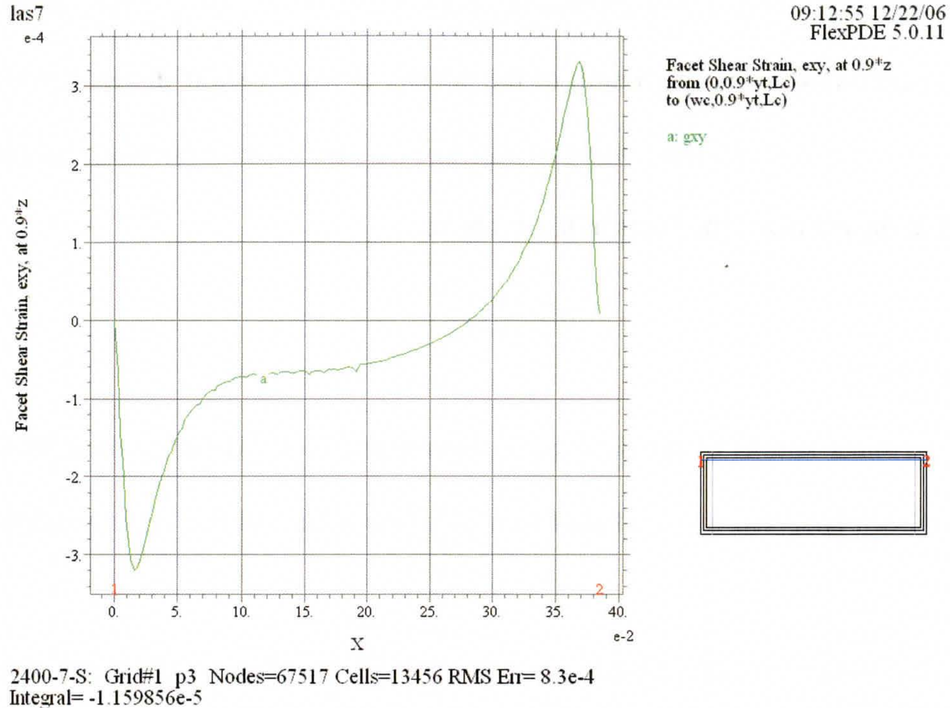

(b)

Figure 6.28. This figure shows the shear strain profile evaluated at 0.1 and 0.9 times the height, yt, of the facet.
As noted before, $gxy \equiv \varepsilon_{xz}$.

The asymmetry is present, though it is not centred about the bisecting line.

The FEM fit for this sample is rather distinctive for it was obtained without imposing strains on the top of the facet. The DOP and ROP patterns were generated from strain patterns imposed at the bottom of the device. Presumably the primary origin for the strain patterns observed on the facet of the device resides in the solder and carrier. This is consistent with what was argued in 6.4.1.

From an examination of the basis functions used to fit to the data, it is found that the single imposed bottom vertical strain has a torsion component.

Additionally, the explicitly y-dependent strain contains a third order term, indicating curvature along the length of the device, at least a short distance from the facet. These two factors might contribute to the compressive ε_{xx} strain observed at the centre of the facet in 6.4.1. above.

6.4.4. Summary

The shear strains of six devices, as determined by FEM fits to their ROP data have been analysed in an attempt to explain the nature of the strain patterns on them.

5000 hours (a) las2 reveals a nearly perfect asymmetry about the line bisecting the facet vertically. It shows no torsion terms in the strains imposed on it to generate the fit. Both facts suggest that bending due to either, or both of, the carrier and the metal contact is the primary cause of the strain observed.

5000 hours (b) las6 also reveals an asymmetrical distribution of the shear strain, though it is not as perfect as the case above. This is possibly due to the twisting terms present in the basis functions used to generate the strains imposed on the device for the FEM fit. Thus, although there is a bending of the device, more severe at the top than at the bottom, there is also a twisting of the facet.

3100 hours (a) las2 indicates no asymmetry. The material is therefore not under significant bending. However torsion terms in the basis functions suggest shear due to the metal and carrier exerting a twisting moment on the die. Additionally, strong y-dependence on some of the basis functions up to and

including the fourth order suggest non-uniform deposition of metal and solder, so that more interior regions of the device, or at least those regions near the surface, should experience curvature due to this.

3100 hours (b) las9 shows localised asymmetry near the bottom right-hand and the top left-hand corners of the facet. This is posited to be due to a combination of die overhang as well as the torsion due to the incomplete coverage of the solder at the bottom of the device. There are also high-order y-dependent terms in the basis functions for the strains imposed on the device for FEM fitting. This also suggests non-uniform deposition of the metal and solder.

2400 hours (a) las9 reveals asymmetry near the bottom but not near the top of the device. Thus, one may assume that the carrier contributes to the bending of the device here. There are also no y-dependent terms in the expansion for the strains imposed at the top of the facet, suggesting that the metal contact is uniformly deposited there. There are, however, torsion terms both at the top and bottom of the device.

2400 hours (b) las7 reveals asymmetry, though this is not centred around the bisecting line. The FEM fit needed no strains imposed at the top of the device, only the bottom, suggesting that the primary origin for the strain patterns in the facet was the carrier. A combination of torsion due to the carrier as well as a strong curvature in the body of the die may explain the ε_{xx} compressive tensile strain observed before.

It may therefore be noted from these figures that FEM fit plots of the shear strain reveals details of the bonding and metallisation. This is not surprising, as previous work has shown [11]. For instance, comparing figure 6.23. (a) to figure 6.24 (a) for the bottom of the respective devices, one sees that the ε_{xz} is positive on the former and is negative in the latter. This is consistent with a pronounced upward bending in 5000 hours (a) las2 (see figure 6.7) versus the slight compressive downward bending (as inferred from the compressive ε_{xx} strain) noted in 5000 (b) las6 (see page 97). Similarly, local variations in ε_{xz} $(x,z = const)$ may also reveal further bonding and metallisation details. For instance, all the curves in these figures and even those for the tensile strain plots are fairly 'smooth', and largely lacking local discontinuities in $\frac{\partial \varepsilon_{xz}}{\partial x}$. Such discontinuities have been related to bonding defects such as voids [11]. Presumably, these are absent in the devices fitted to.

6.5. Conclusion

This chapter has introduced the finite element method, and described how it has been used to fit to the data using the proprietary programme, FlexPDE, and the custom-built programme, X3D. Its purpose has been to quantify the strain observed and explain the origins of this strain.

Chapter 7. Conclusions

7.1. Introduction

This thesis documented research carried out by the author as part of his MASc studies. This final chapter presents a summary of the work carried out by chapter and some ideas for possible work to be carried out in this area.

7.2. Review

Strain is one among the many factors that can influence the lifetime of a device. The hypothesis that was the basis of this work was that stress (or strain) played a major role in determining the performance of the diode lasers.

Chapter 1 presented a synopsis of the thesis.

Chapter 2 provided a brief introduction to elasticity. It also introduced the use of polarisation-resolved photoluminescence (DOP and ROP) to determine the strain on III-V materials.

Chapter 3 described the details of the experimental system used to make measurements on the devices. It also explained the process used to make the devices themselves.

Chapter 4 presented a qualitative treatment of the data. It was discovered that some of the very short-lived devices showed extensive damage to the top (near the active region). The shorter-lived devices also showed high strain in these areas. An examination of scanning electron micrograph images showed that the

reason for this was likely due to the shape of the metal and dielectric deposited around the ridge region. DOP patterns near the bottom regions were in general rather complex, but did not reveal any particular influence on device reliability. Additionally, it was found that ROP patterns were similar across most devices in all hour groups, characterised by an asymmetry due to a twisting moment. The tops of the facets were not under a lot of shear strain, and so it was concluded that ROP would not significantly affect the performances of these devices.

Chapter 5 presented a quantitative treatment of the data by introducing two metrics, v and w. v measured the difference between the middle and the top of an area-averaged DOP and ROP value for a device. w measured the average strain profile across the top of the facet, specifically how the strain immediately beneath the ridge region differed from regions immediately to the right and left of it. Correlations were sought between these metrics and device parameters such as aging time, metal thickness and type, and threshold current degradation rate. Statistically significant differences were found between individual devices of one test-hour group when compared with another test-hour group via the v(%DOP) metric. The only exceptions occurred when devices from the 3100-hour group were compared to the 3200-hour group; and when devices from the 4300-hour group were compared to devices from the 5000-hour group. While the average v-values of aged and non-aged devices consistently indicated a difference, this was found to be within experimental error. However, both the consistent trend between aged and non-aged devices as well as the tendency of rms-error values to

be exaggerated in highly strained structures meant that the difference between aged and non-aged devices could not be so quickly dismissed. It was therefore concluded that v(%DOP) could allow one to observe the length of time for which a device is annealed. None of the metrics displayed a clear correlation to the nature of contact thickness. Additionally, none of the metrics showed any correlation to device reliability, possibly due to the protracted aging time of the devices investigated for this thesis.

Chapter 6 introduced the ideas of the finite element method, and outlined its use in the solution to the differential equations presented by the elasticity problem in this work. The origin and values of the strains observed were elucidated through FEM fits to the data. For instance, non-uniform deposition of both metal and solder could be inferred from the nature of the basis functions used to generate fits to the data.

7.3. Suggestions for Future Work

There are some areas which for various reasons were not explored in this work, but which might make interesting study in future. It would have been interesting to examine the active region in plan view. Not only would this give one the strain distribution in the body of the laser diode, but it would also allow one to detect any possible defects such as dislocations. The idea that the difference in v-value between aged and non-aged samples is due to strain-

relieving mechanisms such as this would also be tested in this way. As it is, the information is not quite complete.

ν(%DOP) has been shown to be sensitive to the aging time to which the device has been exposed. It would also be fascinating to see how far one can take the notion of the ν-value. It would be interesting to find out how finely the concept is able to resolve the difference in life-test hours between different devices, and therefore its evolution as the device ages. This might also shed some light on whether the aging-induced increase in value seen in this thesis was due to strain-relieving mechanisms, or simply experimental error. The consistently more positive average ν-value for the aged as compared to the non-aged devices within a particular hour group as well as the fact that more highly strained environments generate a larger rms error suggests that the errors observed for the non-aged devices may be exaggerated. It is therefore likely that the change in average ν-value between aged and non-aged devices represents something of physical significance.

The author had no control over the processing and subsequent aging of the devices investigated for this thesis. In order to conclusively determine whether or not a correlation exists between the metrics and device reliability, it might be instructive to manufacture devices with identical metal contacts. Degradation rates might then be calculated based on non-linear fits to the I_{th} vs time data following limited aging time.

REFERENCES

1. Mitsuo Fukuda, "Laser and LED Reliability Update," Journal of Lightwave Technology, **6**, pg. 1488-1495,1988.
2. Mitsuo Fukuda, *Optical Semiconductor Devices.* Wiley-Interscience (1999).
3. S. Zhang, M.G. Bourdreau, R. Kuchibhatla, Y. Tao, S.R. Das & E.M. Griswold, "Influence of the Electrical Contact on the Reliability of InP-Based Ridge Waveguide Distributed Feedback Semiconductor Diode Lasers for Telecommunications Applications," J. Vac. Sci. Technol. A **22**(3), pg. 803 – 806, 2004.
4. A.S. Wakita, N. Moll, S.J. Rosner & A.Fischer-Colbrie, "Thermal Stability of MoAu and TiPtAu Nonalloyed InGaAs Contacts," J. Vac. Sci. Technol. B **13**, 2092 (1995).
5. M. A. Fritz., *Die Bonding of Diode Lasers.* PhD thesis, McMaster University, Department of Engineering Physics (2004).
6. D. Lisak & D.T. Cassidy, "Bonding Stress and Reliability of High Power GaAs-Based Lasers," IEEE Trans. Comps., Pack., Manuf. Technol. **24**, 92-98 (2001).
7. V. Swaminathan, L.A. Koszi & M.W. Focht, "Effect of Macroscopic Stress on Accelerated Aging of GaInAsP Channeled Substrate Buried Hetereostructure Lasers," J. Appl. Phys. **66**, 1849-1854 (1989).

8. P.D. Colbourne, *Measurement of Stress in III-V Semiconductors Using the Degree of Polarization of Luminescence.* PhD thesis, McMaster University, Department of Engineering Physics (1992).
9. P.D. Colbourne & D.T. Cassidy, "Imaging of Stress in GaAs Diode Lasers Using Polarization-Resolved Photoluminescence," IEEE Journal of Quantum Electronics **29**, No. 1, 62-68 (1993).
10. D.T. Cassidy, S.K.K. Lam, B.Lakshmi & D.M. Bruce, " Strain Mapping by Measurement of the Degree of Polarisation of Photoluminescence," Applied Optics **43**, No. 9, 1811-1817 (2004).
11. M. A. Fritz & D.T. Cassidy, "Extraction of Bonding Strain Data in Diode Lasers From Polarization-Resolved Photoluminescence Measurements," Microelectronics Reliability **44**, 787-796 (2004).
12. S. Adachi, *Physical Properties of III-V Semiconductor Compounds.* Wiley-Interscience (1992).
13. J.F. Nye, Physical Properties of Crystals. Oxford, Clarendon Press (1957).
14. P.C. Chou, N.J. Pagano, *Elasticity: Tensor, Dyadic and Engineering Approaches.* D. Van Nostrand Company (Canada), Ltd, 1967.
15. S.L. Chuang, *Physics of Optoelectronic Devices.* Wiley-Interscience (1995).
16. C.P. Kuo, S.K. Vong, R.M. Cohen, & G.B. Stringfellow, "Effect of Mismatch Strain on Band Gap in III-V Semiconductors," J. Appl. Phys. **57**(12), 5428-5432, (1985).

17. G. P. Li, T. Makino, R. Moore & N. Puetz, "1.55 μm Index/Gain Coupled DFB Lasers With Strained Layer Multiquantum-Well Active Grating," Electron. Lett. **28**, 1726-1727 (1992).

18. Discussions held with Dr. Marcel Boudreau, InP MZ Design, Bookham Co. Ltd.

19. As quoted in the online version of *CRC Handbook of Chemistry and Physics, 87th Edition.* CRC Press. Boca Raton, Florida, 2006; Section 12, Properties of Solids; Thermal and Physical Properties of Pure Metals. (http://www.hbcpnetbase.com/).

20. R.P. Runyon, K.A. Coleman, D.J. Pittenger, *Fundamentals of Behavioural Statistics*. 9th Edition. Mc-Graw Hill (2000).

21. H. Friedman, *Introduction to Statistics.* 1st Edition. Random House (1972).

22. J.E. Freund, *Modern Elementary Statistics.* 4th Edition. Prentice-Hall (1973).

23. A. Katz, B.E. Weir & W.C. Dautremont-Smith, J. Appl. Phys. **67**, 6237-6246 (1990).

24. P.R. Bevington and D.K. Robinson, *Data reduction and error analysis for the physical sciences*. 3rd edition. Mc-Graw-Hill (2002).

25. S. C. Chapra, R. P. Canale, *Numerical Methods for Engineers*. New York, McGraw-Hill, 2006.

26. K.H. Huebner, E.A. Thornton & T.G. Byron, *The Finite Element Method for Engineers*, 3rd Ed., John Wiley & Sons Inc. (1995).

27. J.J. Coleman, "Strained-Layer InGaAs Quantum-Well Heterostructure Lasers," IEEE Journal on Selected Topics in Quantum Electronics, **6**, no. 6, 1008-1013 (2000).

9948 36